University of
Stavanger

Faculty of Science and Technology

MASTER'S THESIS

Study program/ Specialization: Petroleum Geosciences Engineering	Spring semester, 2021 Open access
Writer: Zohyab Afzal	…………………………………………… (Writer's signature)

Faculty supervisor:

Udo Zimmermann

Thesis title:

The use of a magnetic separator ('FRANTZ') and Energy dispersive spectroscopy (EDS) for separation of heavy minerals: A case study from South Africa.

Credits (ECTS): 30

Key words: Frantz Isodynamic separator Heavy minerals Scanning Electron Microscope (SEM) X-Ray Diffractometer (XRD) Energy dispersive spectroscopy (EDS)	Pages: 64 + enclosure: 41 Stavanger, 19.08.2021

The use of a magnetic separator (‘FRANTZ’) and Energy dispersive spectroscopy (EDS) for separation of heavy minerals: A case study from South Africa.

by

Zohyab Afzal

MSc Thesis
Petroleum Geosciences Engineering
Presented to the Faculty of Science and Technology
University of
Stavanger Norway

University of Stavanger
August 2021

Acknowledgement

Firstly, I wish to express my deepest gratitude to my supervisor Dr. Udo Zimmermann, for his guidance and providing me an opportunity to conduct and complete this thesis project. Your professional attitude, continuous engagement and persistent support is a true inspiration for me. Without this, the goal of completing this project wouldn't be achieved.

I would like to thank Staff Engineer Caroline Ruud who helped in preparing samples as well as formulating the best everyday solutions for my laboratory related matters at UiS.

The acknowledgment extends to Research fellow Mona Minde (UiS) who trained me with the use of SEM and EDS and also to Senior Engineer Wakshum Mekonnen Tucho (UiS) who was always there to help and answer SEM related questions.

Waqar Ahmed (friend), Qazi Abdul Rauf (friend) and Shujah Nasir (friend) deserves huge thanks for their guidance and continuous support.

Lastly, I want to thank my parents for always supporting me. Your patience, endless encouragement and never giving up on me will always be appreciated.

Abstract

A detail study on three selected samples is applied to dispatch the of effectiveness of Frantz isodynamic separator for separation of heavy minerals. Samples selected for study are amphibolite, phyllite and lava from Rosh Pinah Formation, Grootderm Formation and Vredefontein Formation respectively. The selected samples contains only magnetic fraction of heavy minerals, whereas the non-magnetic fractions was removed by Geotrack international, Australia at 25º forward slope and 2º side slope on full Frantz scale. Separation of minerals in Frantz isodynamic separator for three different grain sizes (for each sample) is carried out at magnetic field strength ranging from 0.1 A to 0.4 A keeping 25º forward slope and 15º side slope. The minerals in Frantz separated fractions are identified using FE-SEM-EDS analysis. Generally, amphibolite has low amount of quartz compare to phyllite and lava. The dominant amount of quartz, albite and feldspar in lava indicates felsic to intermediate composition.

The analysis of Frantz separated fractions shows that, light minerals such as quartz, albite, anorthite and other occurs as relict of magnetic separation. The dominance of these minerals in magnetic fractions is attributed chiefly to presence of lithoclasts in the samples. The comparison of heavy mineral concentration in different lithologies suggest that some of heavy minerals such as hematite, tin bearing hematite, almandine, occurs in all lithologies in different grain sizes. Furthermore, there occurrence is not restricted to specific magnetic fraction instead they have range of extraction. Mostly these mineral lies in expected range of extraction except few cases where they are found in other magnetic fractions. Rutile, a high temperature mineral and is abundant in amphibolite suggesting high pressure temperature condition. Goethite is dominantly found in phyllites indicating chemical weathering. Rutile also shows abundance in all magnetic fractions, making it difficult to define exact range of extraction.

The presence of some non-magnetic mineral such as apatite-F, zircon, monzonite, barite and titanite in samples and their occurrence in magnetic fractions retained at low magnetic field strength indicates separation of non-magnetic fraction done by Geotrack international, Australia was not fully effective. The reason could be occurrence of these minerals in the form of locked grains with other paramagnetic minerals. The tourmaline among all the heavy minerals shows most effective separation for grain size >150 µm and for un-sieved fraction, however the high amount of lithoclasts in grain size >250 µm could be the reason of effecting the separation in this grain size. Certain heavy minerals such as tourmaline, monzonite, titanite and barite are limited to phyllite and lava only indicating possibility of extraction of determining heavy minerals for correlation.

Contents

List of figures

List of tables

Commonly used abbreviations

SE	Back-Scattered Electron
EDS	Energy Dispersive Spectroscopy
FE	Field Emission
HM	Heavy minerals
keV	Kilo electron-volts
A	Ampere
SE	Secondary Electron
SEM	Scanning Electron Microscope
UiS	University of Stavanger
µm	Micrometer
WD	Working distance
wt%	Weight percent
XRD	X-Ray Diffractometer
Af	Apatite fraction
Mf	Magnetic fraction
Zf	Zircon fraction
Zc	Zircon concentrate

1 INTRODUCTION

A detailed study on three selected samples from Gariep belt (South Africa) is carried out to know how each lithology reacts in Frantz isodynamic separator. The thesis defines strategy to separate heavy minerals from whole rock and also it evaluates the effectiveness of Frantz isodynamic separator when it comes the separation of heavy minerals from rock sample of different grain sizes. Single grain analysis using analytical methods such as Field Emission Scanning Electron (FE-SEM) and Energy Dispersive Spectroscopy (EDS) aided in identification of minerals concentrations. The worth of this combined approach is presented in this thesis by a case study of phyllite (Grootderm Formation), amphibolite (Rosh Pinah Formation) and felsic lava (Vredefontein Formation) from the Porth Nolloth group and Marmora terrane.

1.1 Objectives of the study

The objective of this thesis is to study and get better understanding how Frantz isodynamic separator can be fruitful for separation of heavy minerals from Neoproterozoic lavas, phyllite and amphibolite from Gariep belt. The selected samples have been already gone through Frantz magnetic separation in (by Geotrack international) Australia at 25º forward slope and 2º side slope on full Frantz scale. The resulting apatite fraction (Af), zircon fraction (Zf) and zircon concentrate (Zc) was taken out and the magnetic fraction (Mf) was kept in the samples.

The separation carried out for this project at UiS is at 25º forward slope and 15º side slope. Full Frantz scale was not used, instead the magnetics field strength from 0.1 A to 0.4 A was utilized to carry out the separation. The aim is to identify minerals and map their percentages in each separated fraction to get deep insight which fraction is most promising for specific group of heavy minerals. The sample will be analyzed using different analytical methods: Scanning Electron Microscopy (FE-SEM) with Back-Scattered Electron (BSE) detector, and Energy Dispersive Spectroscopy (EDS) detector and X-Ray Diffractometer (XRD).

Finally result will be analyzed and integrated to understand the behavior of mineralogy from each lithology in the magnetic separator.

1.2 Sampling area

The samples have been collected by Dr. Udo Zimmermann (supervisor for the thesis project) from three outcrops exposed in southern part of Nambia and southwestern part of South Africa. The first rock Formation has GPS coordinates 28° 48' 57,30"S 17° 14' 4.00"E (marked with green triangle in Figure 1.1), the second outcrop has GPS location is 27° 49' 44,5"S 16° 42' 17,52"E (marked with red triangle in Figure 1.1) and third rock Formation has GPS location 28° 30' 26,8"S 16° 42' 39,9"E (marked with yellow triangle in Figure 1.1).

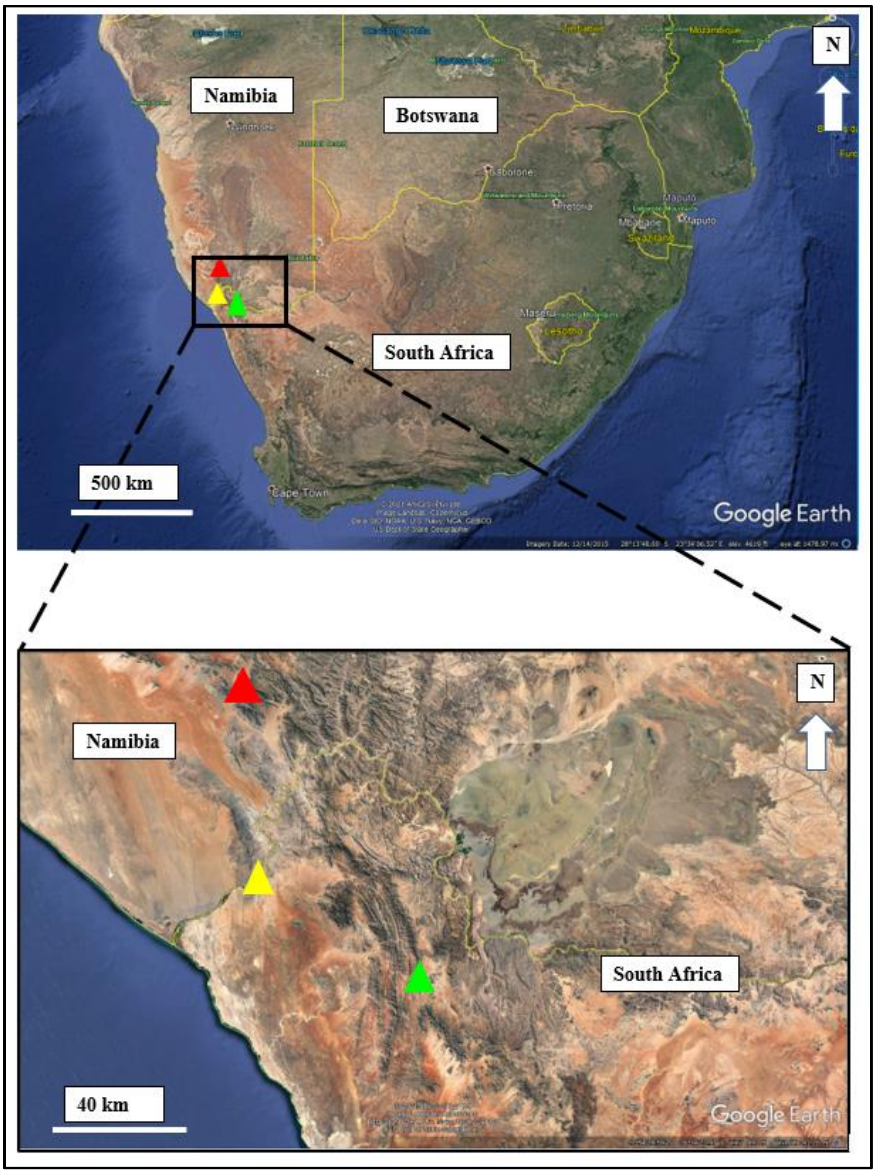

Figure 1.1: Location of sampling areas in southern part of Namibia and southwestern part of South Africa. The red, green, and yellow triangles show location of three sampling areas. (Modified after google earth (August 12, 2021))

1.3 Geologic setting

This section will discuss the geological features of the Gariep orogenic belt, with particular emphasis on the Port Nolloth group and Marmora- chameis. Specifically, the student bases emphasis precisely on Vredefontein, Rosh Pinah, and lastly, Grootderm Formation.

1.3.1 Gariep Belt

Gariep belt is known to be the superior of the geological features of the southwestern part of Namibia. This feature forms a significant percentage of the rock basement of Namib's desert, be it covered or manifested with sand. The desert is between Orange River and Lideritz. This belt goes beyond coastal inland, as seen in the Figure 1.2.

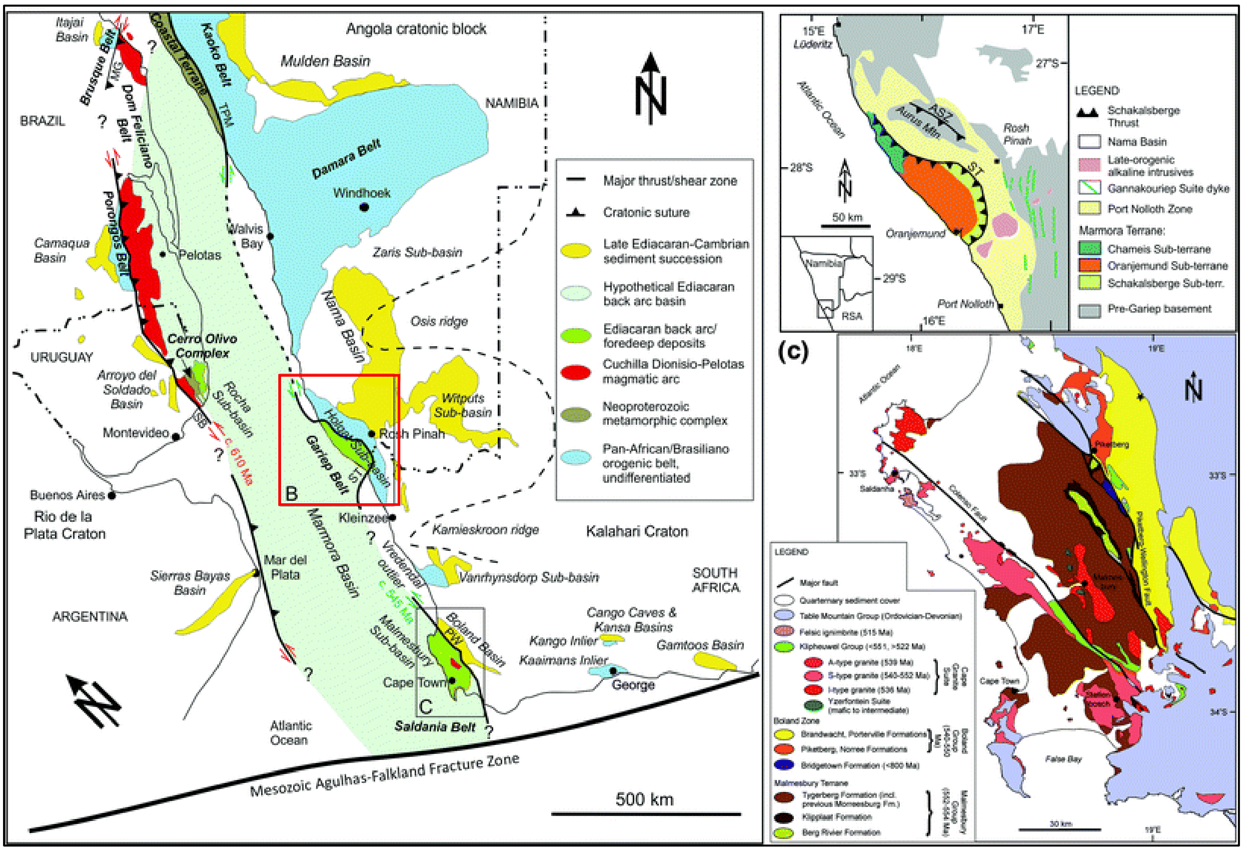

Figure 1.2: Gariep belt position pan-Africa orogenic plate framework in southwestern Africa and inferred Ediacaran Marmora. The red square marks the study area (modified after (H. Frimmel, Basei, & Gaucher, 2011)).

It was named Gariep, which means Great River. The belt is well manifested in South Africa in the western Richtersveld region after crossing the Orange River. Again, the belt stretches along the coast southwards to Kleinzee according to arcuate North-northwest trends. We notice from the research that the Gariep belt is an extensive pan-African Brasiliano and Neoproterozoic section up to Cambrian Orogens as observed in west-Gondwana. Hence, you can easily compare their tectonic and stratigraphy evolution with Damara and Kaoko belt in central and northwestern respectively (Germs, 1995).

Numerous models (Geodynamic) suggest the formation of many pan-African belts along with South Africa. Historically, the Gariep Belt and the coast-parallel sections of the Pan-African orogenic belt system, through the Congo Cratonic Bridge (Sào Francisco), have also been perceived to be the African segment of the Neoproterozoic South American-African suture. This geodynamic model is therefore integrated into studies. However, the Gariep Belt should involve the disfigured part of a Neoproterozoic passive margin and record a complete Wilson Cycle. A large percentage of the past research prioritized westward subduction below Rio de la Plata (Germs, 1995). This conclusion was later seconded by (Schorn & Diener, 2017).

A second model was also suggested and put forth. The model was majorly based on the provenance of zircon together with geochemical data-sediment isotopes. This model claims the suture location to be inland Brazil and Uruguay rather than coastlines (Basei, Frimmel, Nutman, Preciozzi, & Jacob, 2005). Additionally, it states that the fragment was split from Kalahari craton during the Rodinia breakup (Basei et al., 2005). Since the Gariep belt had got little attention in the 20th century, it becomes difficult to access the number one diamond region (Martin, 1965). The mapping research outcomes are contradicting. Recently, both tectonothermal as well as age progression, such as pre-Gariep basin in the belt, have been studied (Thomas et al., 2016). Additionally, the belt has main metallic base ores- Rosh Pinah Province that currently consists of two mines: Zinc at scorpion and Zn-Pb at Rosh Pinah. Because it is highly restricted, the best is yet to be explored for deposits.

1.4 Basin architecture and stratigraphy

During the Gariepian orogeny, many activities took place. These are strenuous folding, southeast thrust, and torsion faults that destroyed all concrete proof of the sedimentary basin, including their original magnitude, depth, and composition. The eastern edge, characterized by reversed arrangements along which they pressured Neoproterozoic sedimentary rocks against their base, is well marked. Therefore, the two major zones of tectonostratigraphic are classified. These are Marmora Terrane and Port Nolloth. We can distinguish these two zones via Schakalsberge Thrust. Even though port Nolloth's destruction was internal, it still retains its basement's para-autochthonous feature. The prior relationship was evident using silvers with their geochemical proofs.

While Marmora Terrane does not have a basement since it is altogether thrust bound. Their lower part lacks critical continental deposit hence termed as allochthonous. Port Nolloth shape depicts the margin of the eastern outline on Pinah rift Graben. In the Gariep belt, the rocks have substantive proof of the tectonic stages since crustal to amalgamation occurred during the continental-continental collision of Neoproterozoic time. Every series stage left reasonably distinct succession. From history, the record of the belt rocks can be subdivided into post-orogenic and pre-synorogenic. These form the Gariep supergroup as shown in Figure 1.3.

Researchers observed both the pre-rift and post-orogenic phases of magmatic in the Gariep belt. Synogenous magmatic does not appear to exist. Before focusing the study of a simultaneous stratigraphic comprehension to specific issues, they had already classified the lithostratigraphic segment volcano-sedimentary units in the Gariep belt, particularly in the Port Nolloth area.

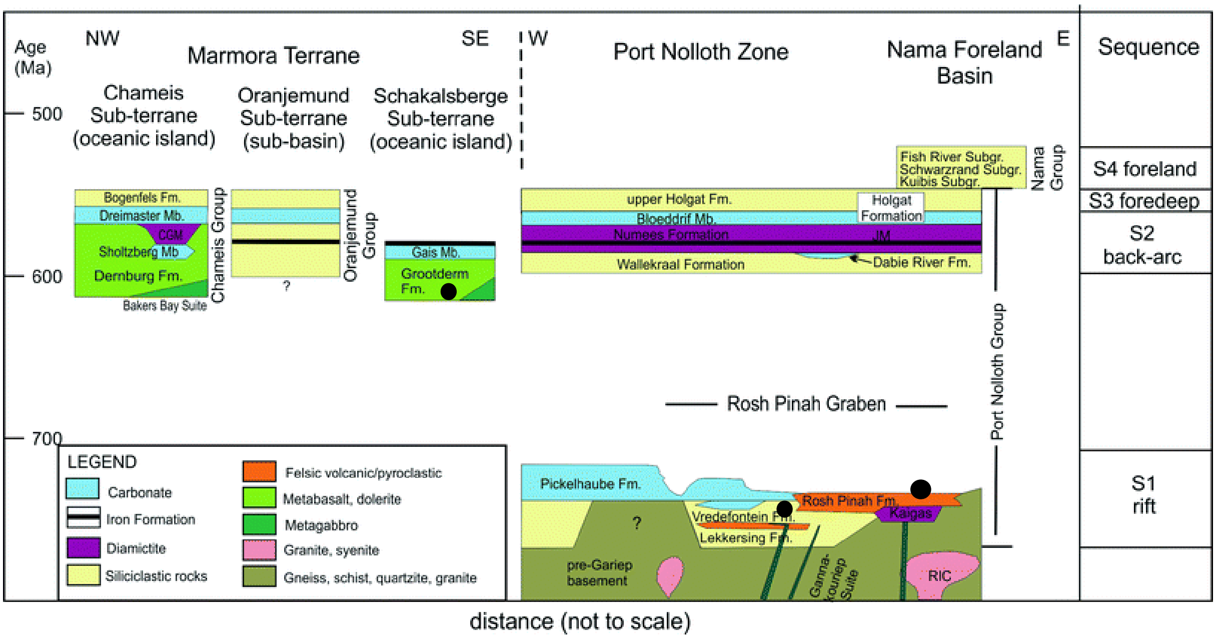

Figure 1.3: The Gariep Supergroup with subgroups, members, and formations. (Fm= Formation and Mb=Member). Black dots mark the rock formations under study (Siegesmund, Basei, Oyhantçabal, & Oriolo, 2018).

This was when the entire succession was perceived in expressions of a classic full Wilson Cycle (Van der Voo & French, 1974). Later, they combined the two different sediments succession deposited at various basins to form a single lithostratigraphic. The conclusion from above figure (Figure 1.3) can be made that port Nolloth has three other deposits of multiple sequences. In this section, we will now move on to the subgroups of Port Nolloth group, and Marmora terrane. The lithostratigraphic map of Gareip Belt is shown in Figure 1.4.

1.4.1 Port Nolloth Group

This group links all Neoproterozoic and volcanic, which are older than pan-African orogenic displacement, which consists of the port Nolloth area. Deposition of sediments followed through a sequence of stages from continental rift Graben to stinkfontein (Siegesmund et al., 2018).

The fans (both Alluvial and delta) alongside alluvial plains were the prevailing depositional areas along the western side of a vigorously growing fault scarp. This growth fault was the epicenter of volcanic activity. With deeper water reserves further west, pragmatic subsidence resulted in noticeable facies alterations (Siegesmund et al., 2018).

The development of kaigas and proximal glaciogenic has accumulated carbonate sediments that facilitate Rosh Pinah and pickelhaube Formation. Debie River was formed in the process due to reef facie carbonate development. The second period resulted in the formation of Numees and other rocks (Siegesmund et al., 2018).

1.4.2 Stinkfontein subgroup

This subgroup is evidenced in South Africa and the Gariep belt and further subdivided into Vredefontein and lekkersing. Lekkersing extends Orange River southwards with common erosional channels that are both continuous and discontinuous. Their cross-bedding inclination reversals are traced from antidune features (Van der Voo & French, 1974). At the upper part of this subgroup, there is Feldspathic. This sandstone, with time, becomes continuous and undergoes a transition to form Vredefontein Formation. The rocks of Vredefontein Formation grows as far as 300m in diameter. Internal sedimentary forms are well maintained in the prevalently medium-bedded feldspathic sedimentary rock, enhanced by heavy mineral levels along the laminations. Low-angle wedge or Trough Bridge is alternated with parallel embossed bedding. Uneven spiral points with linguoid and cuspate peaks occur on a limited basis (Van der Voo & French, 1974).

The upper part of Vredefontein Formation is characterized by thick packages of volcanic rocks, of basic to acidic in composition however, intermediate variety dominates (E. Middlemost, 1966). The rocks are only widespread in South Africa.

Due to siliciclastic succession in Namibia, stinkfontein distribution is still enigmatic due to their similarity. The lateral facies are changed to correlate with those in South Africa due to both upper and lower tectonic nature. During the lithological of the Rosh Pinah Formation, the upper contact remains closed (Siegesmund et al., 2018). This is because; Rosh Pinah stays above Stinkfontein Formation in this area. The stratigraphic diameter is only estimated to be 800m. The Stinkfontein Subtype in Namibia is geologically alike the Richtersveld's Vredefontein. The Stinkfontein Formation is not present in the tending branch of northwest to southeast and Aurus Mountain. This fact suggests another thing. However, the region consists of Kaigas Formation(Siegesmund et al., 2018).

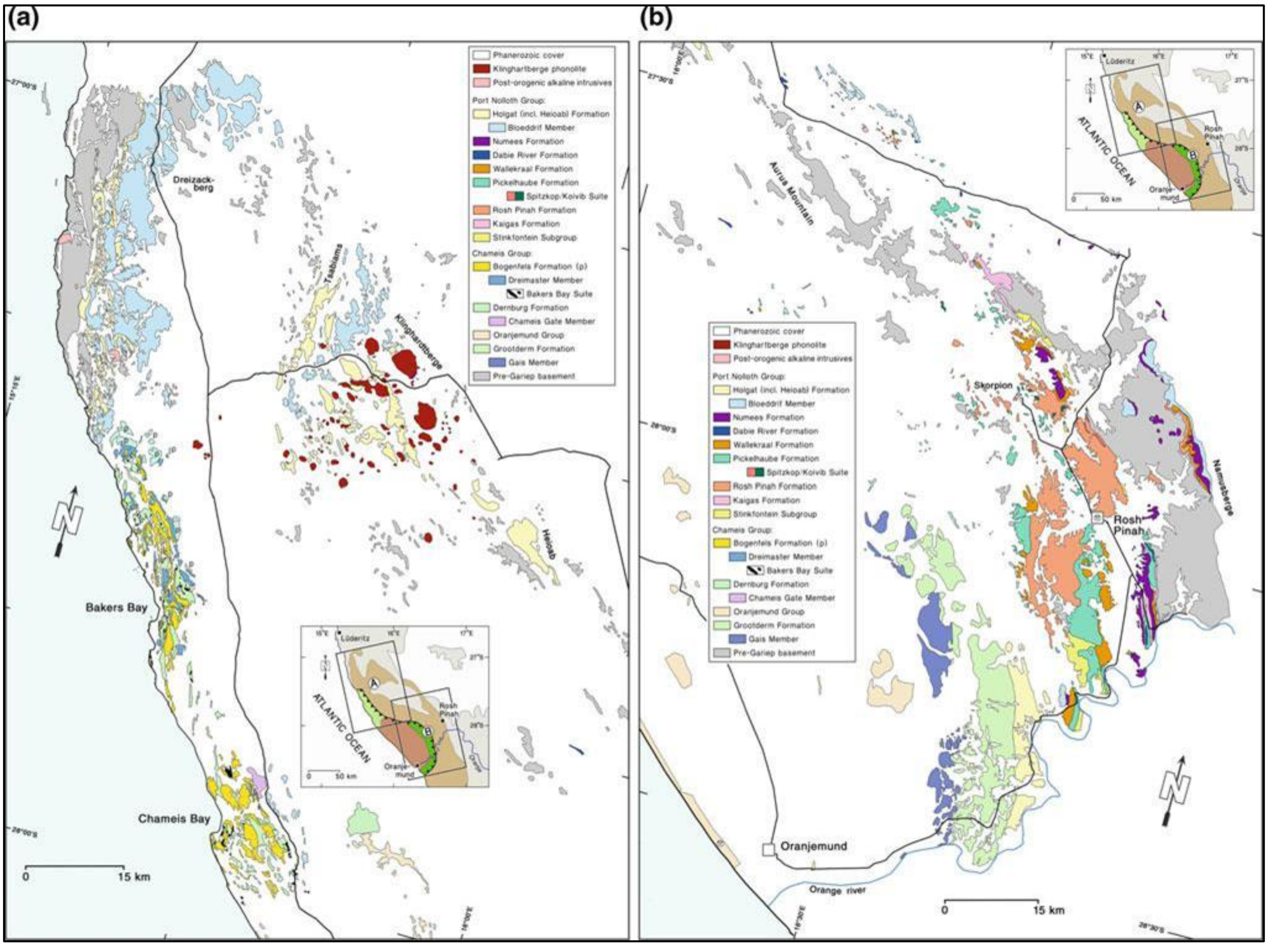

Figure 1.4: Namibia Gariep Belt lithostratigraphic map: a northwestern part, b southeastern part. (H. E. Frimmel, 2018).

1.4.3 Kaigas Formation

This Formation is only found locally in a rift basin. In South Africa, they go to extend of 115m thickness. These rocks lie in the Vredefontein Formation. Specific instances of more than 100 m diameter pinch out over only a few hundred meters, highlighting the defined Formation thickness deviations along the strike. Some of the sedimentary features indicate a vigorous debris flow due to deposition (H. E. Frimmel, 2018). The Formation of kaigas in Port Nolloth is emphasized due to derived rocks in the basin-like amphibolite and granite. From Namibia, we also note that at the southeast, as shown in Figure 1.5 on 16.527°E, 27.679°S that

Formations reach their max thickness. The Rosh Pinah Formation is at 6.706°E, 27.827°S pyroclastic deposit (H. E. Frimmel, 2018).

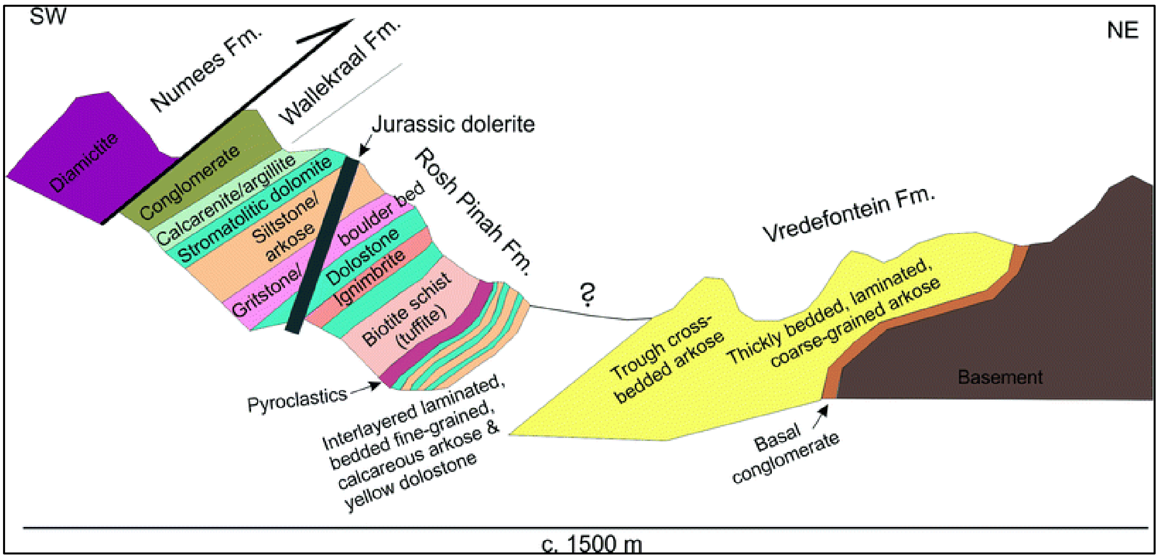

Figure 1.5: Schematic southwest-northeast features in the lower Port Nolloth Group part over the pre-Gariep basin on the farm Trekpoort 96 (Siegesmund et al., 2018).

Establishment of Pickelhaube Southeast of Rosh Pinah and on the Dreigratberg eastern borders, next to the Orange River, comparatively overlying successions via the Pickelhaube Formation with principal lower upper contacts be explored. The apparent lack of conglomerate, shortages of crossbedding, the existence of little bedding, and rising carbonate composition of the Pickelhaube Formation arenites, as contrasted to the fundamental Stinkfontein Subgroup and Kaigas Formation, denote underwater conditions, as can be anticipated in the distal portion of a fan intricate (Siegesmund et al., 2018).

1.4.4 Rosh Pinah Formation

The existence of volcaniclastic, volcanic, and felsic rocks has economic importance (Martin, 1965). According to (Alchin, Frimmel, & Jacobs, 2005) the Rosh Pinah exhibits repeated geologic cycles that mirror faster accumulation with interceding quiescent times related to retrieval on basin striding faults, followed by physical and chemical sedimentation. Tilting of the rift shoulders caused incomplete erosion of the Rosh Pinah Formation and intraformational breccia and olistostromes in proximal positions. The felsic volcanic rock outcroppings on Spitskop 111 and Trekpoort 96, near the implied volcanic center, vary in concentration from rhyodacite to rhyolite (H. E. Frimmel, C. J. H. Hartnady, & F. Koller, 1996). Metamorphic recrystallization impacted the finer-grained kinds, resulting in biotite-chlorite-sericite schist with varying quantities of clinozoisite and calcite. In many situations, traces of volcanic glass shards can peacefully be seen, although they have recrystallized. The local existence of metabasalt and metagabbro and the absence of igneous rocks with intermediary constituents demonstrate that the Rosh Pinah volcanism is bimodal. The metabasalt and metagabbro are completely recrystallized to amphibolite in some places Amorphous ripple-marked quartzite with dolomite, which is exceptionally ferruginous in areas due to fumarolic behavior, strongly correlates with volcanic facies (Siegesmund et al., 2018). A vigorously siderite carbonaceous mudstone with bed linen laminations of galena, pyrite, as well as sphalerite is confined to the Rosh Pinah Zn–Pb–Cu sulfides ore region. It consists of dark grey Arkose with mudstone interbeds on top, as well as partly sedimentary, dolomitized limestone optics. The percentages of detrital alkali feldspar, pyroclastic sanidine, and quartz in the crystal tuff are incredibly unpredictable, indicating varying degrees of sedimentary revisiting (H. E. Frimmel, C. J. Hartnady, & F. Koller, 1996). Geologists can't determine the accurate geologic size of the Rosh Pinah Formation due to tectonic interruptions, but it is considerably higher than 850 m in the Rosh Pinah region.

1.4.5 Wallekraal Formation

The Wallekraal Formation, dubbed following its locality category in the western Richtersveld part of South Africa, is overlain by a regional outcrop in the Port Nolloth Group, which signifies a first-order sequence border (Von Veh, 1988). The belt is hard to trace its uniformity due to its tectonized form. It's evidenced in the clastic rocks that are hard to categorize into various ancient stratigraphy. Coarse-grained siliciclastic sediments, including mature yet well-sorted, dominate Wallekraal Formation. The area is characterized by presence of clasts, specifically olistostromes and dolomite, which are isolated (Siegesmund et al., 2018).

1.4.6 Dabie River Formation

The Formation was dubbed after the South Africa local area (Von Veh, 1988). This Debie River Formation has a thickness extending to 160m. Stromatolites with Conophyton-like geometries (ranging in size from a few centimeters to decimeters in height) distinguish the appearance lithologically from the other carbonate-containing segments of the subgroup. This region also consists of rocks like oolite and pisolites. Because ancient limestone is dolomitized, this Formation is purely calcareous. Dolomite can be categorized as part of this Debie river Formation (Macdonald, Strauss, Rose, Dudás, & Schrag, 2010). Reef rocks formed or were conserved in regions that were spared from pre-Wallekraal destruction. As a result, the Dabie River Formation metal oxides lie in numerous areas paraconformably far above Pickelhaube

Formation dolostone, rather than generally on the edge of the clastic Wallekraal Formation stones.

1.4.7 Numees Formation

The Numees Formation has long been established to be glaciogenic (Martin, 1965). Even though the Formation portion is in the western Richtersveld, this Formation was named; it does not relate to this Formation and is instead a section of the Kaigas Formation (Von Veh, 1988). This reveals a great deal of uncertainty about the diamictite's stratigraphic location and the occurrence of two diamictite units at distinct stratigraphic stages. (Von Veh, 1988) explained thorough evaluation in the western Richtersveld and southwestern Namibia using chemo- and chronostratigraphic statistics (Fölling & Frimmel, 2002).

1.4.8 Marmora Terrane allochthonous

The Marmora allochthonous Terrane is sub-categorized into three thrust sheets; chameis, schakalsberge, and lastly, oranjemund. Every sub-category has varying stratigraphy features. The Schakalsberge complex has a local capping metabasaltic seen as a thick pile-gais member. This sub-group is lithotratigraphically linked as Grootderm Formation. Considering the geochemical features in mafic, Grootderm Formation is currently concluded to be representing the ancient guyot where reef growths are described as gais members. Some of the features that led to this conclusion are the absence of continental detrital, predominant volcanic, and many more (Hartwig E. Frimmel et al., 1996). There is a ferruginous chert band except that are less than 1 meter on gais member. The Oranjemund complex is comprised of meta-greywackes, phyllites and quartzites (Hartwig E. Frimmel et al., 1996). These rocks are categorized to belong to the oranjemund group (Basei et al., 2005).

The Chameis Complex consists of two units i.e. Bongenfels and Dernburg. The geological features of dernburg are similar to those exhibited in Grootderm. The local oolitic and stromatolitic dolomite spreads over this subterrane. The overlying rocks on the members of scholtzberg are spotted as ancient marine deposits of evaporites. They are believed to have originated from an atoll in the eustatic sea-level period (H. Frimmel & Jiang, 2001).

1.5 Samples

The three rock samples analyzed in the thesis project are collected by Dr. Udo Zimmermann (supervisor for the thesis project) from southwestern part of the South Africa and southern part of Namibia. The rock types are phyllite, amphibolite and lava of felsic to intermediate composition.

The three samples are labeled as CR-27, CR-18, and CR-03 extracted from Rosh Pinah Formation, Vredefontein Formation and Grootderm Formation respectively (more details in Table 1.1). All these samples have been separated into different fractions by Geotrack International, Australia. These fractions are:

- magnetic fraction $(> 2.95\ \mathrm{g/\,cm^3})$;
- non-magnetic apatite fraction $(2.95 - 3.3\ \mathrm{g/\,cm^3})$;
- non-magnetic zircon fraction $(> 3.3\ \mathrm{g/\,cm^3})$; and
- zircon concentrate (a fraction nearly contains detrital zircons).

The non-magnetic apatite fraction $(2.95 - 3.3\ \mathrm{g/\,cm^3})$, non-magnetic zircon fraction $(> 3.3\ \mathrm{g/\,cm^3})$ and zircon concentrate (a fraction nearly contains detrital zircons) were detached from the sample and only magnetic fraction $(> 2.95\ \mathrm{g/\,cm^3})$ of these three samples will be used in the thesis project.

Table 1.1: List of samples with sample name, lithology, age, GPS locality, terrane, sub-group, and formation name.

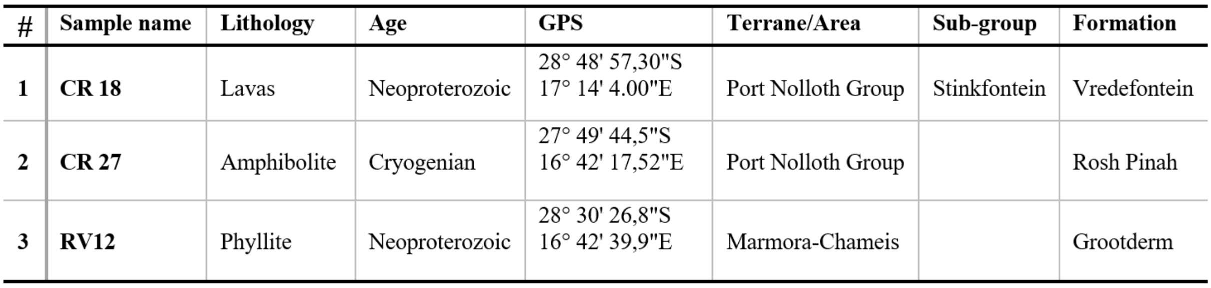

#	Sample name	Lithology	Age	GPS	Terrane/Area	Sub-group	Formation
1	**CR 18**	Lavas	Neoproterozoic	28° 48' 57,30"S 17° 14' 4.00"E	Port Nolloth Group	Stinkfontein	Vredefontein
2	**CR 27**	Amphibolite	Cryogenian	27° 49' 44,5"S 16° 42' 17,52"E	Port Nolloth Group		Rosh Pinah
3	**RV12**	Phyllite	Neoproterozoic	28° 30' 26,8"S 16° 42' 39,9"E	Marmora-Chameis		Grootderm

2 METHODOLOGY

The project's methodology begins with sample preparation for separation in Frantz isodynamic separator before applying different analytical methods. The various analytical techniques employed for the identification of minerals are X-ray diffraction (XRD) and Energy Dispersive X-Ray Spectroscopy (EDS) in combination with Field Emission Scanning Electron Microscope (FE-SEM).

The separation of minerals in Frantz and all other analytical processes such as X-ray diffraction (XRD), Energy Dispersive X-Ray Spectroscopy (EDS), Field Emission Scanning Electron Microscopy (FE-SEM) is carried out at the University of Stavanger (UiS).

At the end of laboratory work, the results from all analyses are analyzed individually and in combination to make a logical interpretation. Table 2.1 shows the different analytical methods applied on different fractions of each sample.

Table 2.1: List of analytical methods applied to each sample.

#	**Sample name**	**Sample type**	**Magnetic Separation by**		**FE-SEM**		**XRD**
			Hand magnet	**Frantz**	**BSE**	**EDS**	
1	CR-27	Reference			X	X	X
		Fraction un-sieved (original)	X	X	X	X	
		Fraction $< 250\ \mu m$	X	X	X	X	
		Fraction $< 150\ \mu m$	X	X	X	X	
2	CR-18	Reference			X	X	X
		Fraction un-sieved (original)	X	X	X	X	
		Fraction $< 250\ \mu m$	X	X	X	X	
		Fraction $< 150\ \mu m$	X	X	X	X	
3	CR-03	Reference			X	X	
		Fraction un-sieved (original)	X	X	X	X	
		Fraction $< 250\ \mu m$	X	X	X	X	
		Fraction $< 150\ \mu m$	X	X	X	X	

2.1 Frantz isodynamic separator

2.1.1 Sample preparation

2.1.1.1 Sieving

Before using the Frantz magnetic separator, each sample was divided into three different fractions based on grain size. The original un-sieved sample is placed as one fraction that includes grains of all sizes (Figure 2.1 and 2.1 b), whereas the sample passed through the sieve of 250 µm and 150 µm represents the other two fractions, respectively. One-half of the un-sieved original sample fraction was used to make reference mount, and the other half was passed through Frantz magnetic separator. The reason behind selecting sample fraction of varied grain sizes was to test the effectiveness of Frantz for sample fraction of larger grain size that contains inclusions or locked fragments of other minerals and for smaller grain size, i.e., <150 µm which have low inclusions or locked fragments.

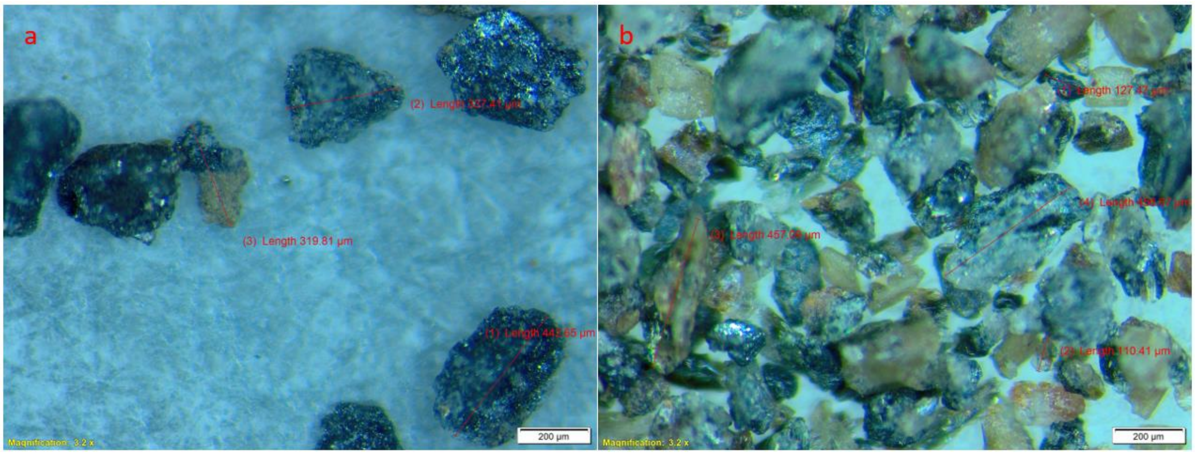

Figure 2.1: Un-sieved sample of sample CR-18 (a) and CR-27 (b) containing grains of varied sizes.

2.1.2 Theoretical background

Physical separation of materials by magmatism is in practice since the time of Thomas A. Edison. The separation process is controlled by the difference in the magnetic properties of a material. Iron enriched magnetic minerals was amongst earliest material processed with these devices. Newly designed magnetic separators are employed in many industries and research institutions for minerals separation (Oder, 1976).

Magnetic susceptibility of minerals is controlled by their chemistry, which plays a vital role in extracting end members of mineral series in cases where iron substitutes magnesium (Rosenblum & Brownfield, 2000). The olivine series is the best example to demonstrate this phenomenon in which iron-rich member (fayalite) is separated in the range of 0.10 to 0.60 A.

In contrast, magnesium-rich member (forsterite) demands a higher current range of 0.40 to 1.20 A for extraction (Rosenblum & Brownfield, 2000).

Frantz magnetic separator is a device that is capable of separating even weakly magnetic materials. It utilizes specially designed magnetic poles to generate a force independent of the distance in an area between these poles. In a free fall deflecting mode, the magnetic separator is known for its unique ability to separate materials with susceptibilities as small as -0.3×10^6 (Oberteuffer, 1974).

2.1.3 Instrumentation

The Frantz magnetic separator comprises a magnet coil positioned above and parallels to a two-channel aluminum track (Figure 2.2), which is slightly tilted and can accept a continuous feed (crushed rock material). The magnetic field created by the magnet can be adjusted as low as 0.01 A for extracting highly susceptible material from the sample to its peak value of 1.70 A for isolating minerals with weak susceptibility. A glass or steel hoper attached above the two-channel track is responsible for feeding the sample grains. These grains of minerals are forced down under the magnet by vibrations.

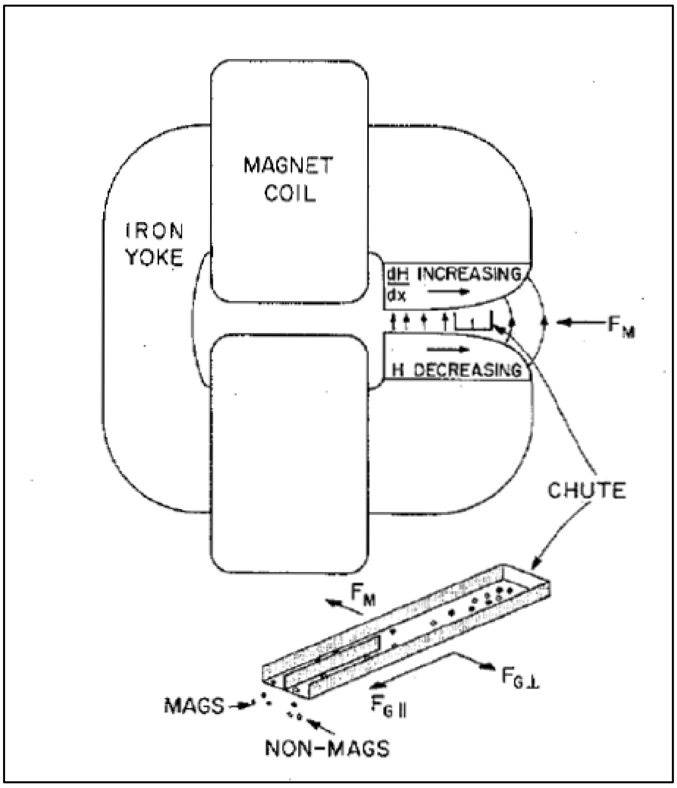

Figure 2.2: Conceptual sketch of Frantz isodynamic separator (Oberteuffer, 1974).

A controlling system for adjusting the vibration of the hopper and track is also installed in Frantz. This system helps to slow down or speed up the feed rate and movement of minerals grains toward the end of the track. When the grains pass through the area lying under the magnet, they split according to their paramagnetic susceptibility. The magnetic material falls into a left (black) container. In contrast, the non-magnetic fraction is retained in a white container situated on the right side at the end of the two-channel track (Strong & Driscoll, 2016).

2.1.4 Purpose of the method

For provenance studies, some heavy minerals are of key importance, so it is an important method to separate them from the whole rock (Morton, 1985). The primary purpose of using Frantz is to separate the different mineral fractions from three samples, namely CR-27, CR-18, and CR-03, based on their paramagnetic susceptibility.

2.1.5 Technical Specifications

The Frantz isodynamic separator (Model: LB-1 and Serial no:751) installed at UiS was used for this thesis project (Figure 2.3). The equipment was used after getting proper Lab training from Caroline Rudd (Staff Engineer at UiS). The ferromagnetic material from each sample fraction was first separated by hand magnet, and later on, the field strength of the magnet starting from 0.1 A was increased to 0.2 A , 0.3 A, and finally to 0.4 A until the total amount of the sample vanished and few grains were left. In the end, the non-magnetic fraction remained at 0.4 A was stored.

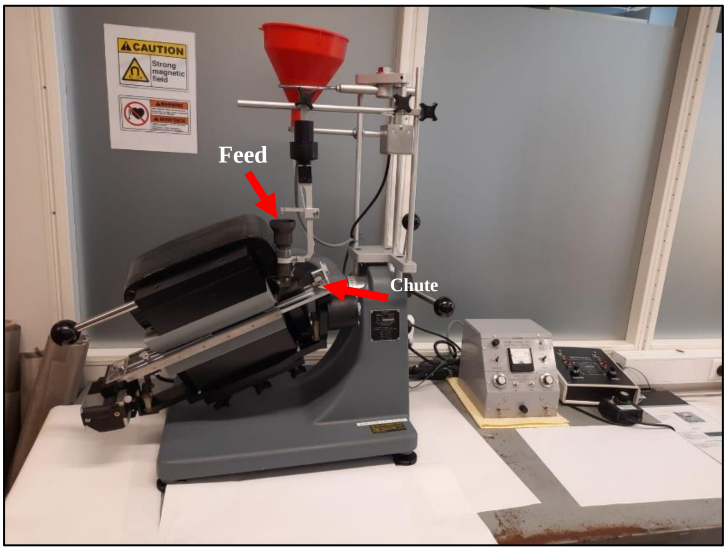

Figure 2.3: Frantz isodynamic separator (Model: LB-1) at UiS Laboratory.

Every sample fraction was passed through Frantz three time on each magnetic field strength to get satisfactory results. For each sample, three fractions of varying size were separated via Frantz (see Table 2.2, 2.3 and 2.4 for details), which makes nine Frantz separated sample mounts. After every sample run, the Frantz magnetic separator was cleaned with ethanol and by a jet of compressed air to prevent sample contamination.

2.2 Scanning electron microscope (SEM)

2.2.1 Sample preparation

2.2.1.1 Mounting

To prepare mounds, a sticky tape was used, on which a random selection of grains was placed (Figure). For each sample, one reference mound and three Frantz separated mounds were created, which became 12 in total for all three samples (see Table 2.2, Table 2.3, and Table 2.4 for more details). Approximately $200 - 500$ grains from each sample and fraction were handpicked by needle and placed on sticky tape side by side in a line.

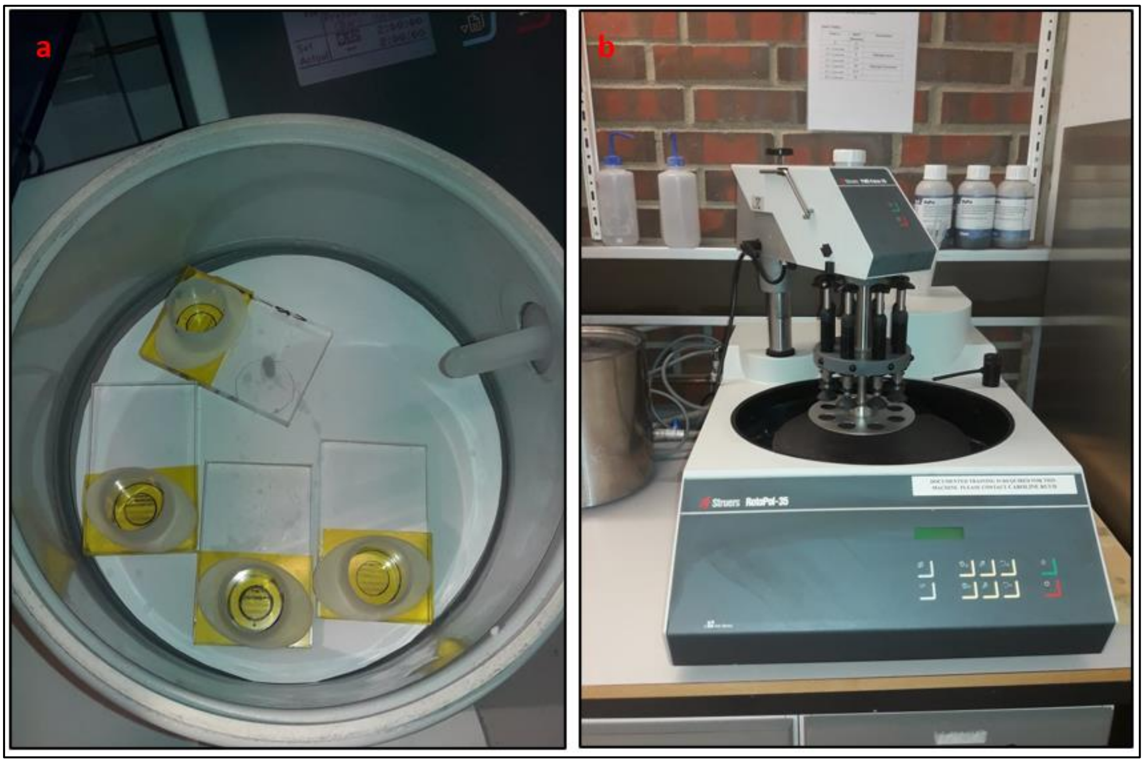

Figure 2.4: Pouring of epoxy on top of grains in a vacuumed chamber (a) the Struers Tegra machine used for polishing sample mounds (b).

After finishing the handpicking of grains, epoxy resin (polymer) was poured on top of the grains and placed on the side to dry for 36-48 hours (Figure 2.4a). The hard mounds having a diameter of 1 inch were taken out of the plastic mold and then were first polished by hand at the grinding plate, and later on, a machine called Struers Tegra (installed at UiS) was used to smooth the surface (Figure 2.4b). The two polishing cloths, “Nap” and “Dac” along with diamond suspension, were used for polishing the mounds in the machine. The samples were polished for 8 minutes with “Nap” cloth and 3 µm diamond suspension and then with “Dac” cloth and suspension of 1 µm. The whole work was done with great care, so the grains do not fall off the mound during the polishing process. The map for each mound can be seen in Figure 2.6, Figure 2.7, and Figure 2.8.

2.2.1.2 Coating

Mostly the geological samples resist the flow of electric current; therefore, they require a coating of conductive material to avoid overcharging under a bombardment of electrons. The carbon coating is most suitable for x-ray analysis. It has a negligible effect on the x-ray spectrum but is not ideal for secondary electron imaging as it can decrease the production of secondary electrons (Reed, 2005).

To carry out the FE-SEM analysis in this project, sample mounts were first coated with a thin layer of carbon in a machine called Emitech K550 Sputter Coater (Figure 2.5). Before applying the carbon coating, the mount's surface was cleaned with pressured air and ethanol.

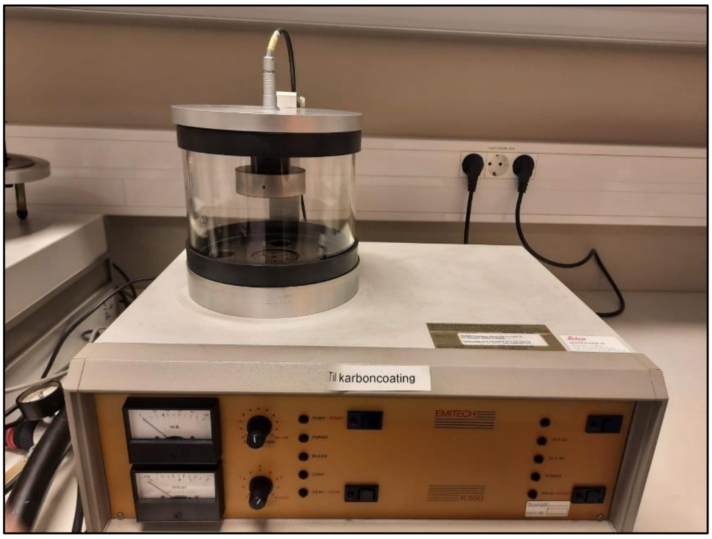

Figure 2.5: Emitech K550 Sputter Coater machine used for coating the mounts before BSE and EDS analysis.

The cleaned specimen was then placed in a vacuum chamber containing a carbon evaporation source made up of two electrodes. The carbon thread was placed tightly in between electrodes. The pressure inside the vacuum was maintained with a turbopump to make carbon more adhesive to the mound surface. Finally, the carbon thread was burnt and then evaporated to throw carbon atoms on the mounting surface. The second layer of coating was done to get better BSE imaging results.

2.2.2 Theoretical background

A scanning electron microscope (SEM) is a device capable of producing magnified images that helps to get microscopic scale information about different parameters such as size, shape, composition, and crystallography of a sample (Goldstein et al., 2018). The admiration of SEM arises from its power to produce images by using an electron beam instead of light, as in a typical optical microscope. Furthermore, the smaller wavelength (λ) of electrons make them able to resolve minutes details of material to a much larger extent compared to an optical microscope. The present-day SEM has even become more powerful and can magnify objects millions of times their actual size. These unique characteristics make it the perfect choice for material characterization, including observing surfaces at submicron and nano-level to describe material properties (Ul-Hamid, 2018). The undeniable advantages of SEM as an imaging tool brand it as an influential instrument in mineralogical studies (Reed, 2005)

2.2.3 Instrumentation

The scanning electron microscope (SEM) consists of three central units: the electron column, the specimen chamber, and the computer control system. The topmost section of the electron column comprises an electron gun responsible for producing an electron beam (Figure 2.9). The beam is focused into a finer diameter probe employing electromagnetic lenses attached within the column. The specimen chamber lies at the end of the column and contains a sample. The scan coils in the column, scan the probe on the specimen surface in systematic order. The column, the gun, and the sample chamber are placed in a vacuum to facilitate electron beam generation and development. When the electrons (traveling in the form of the beam) penetrate few microns in the sample surface, the interaction of electrons with atoms of the specimen results in secondary electrons, backscattered electrons, and characteristic x-rays. These signals are collected at their respective detector and amplified to recreate an image to gain information about the chemistry of the specimen (Ul-Hamid, 2018).

Table 2.2: List of mound names with the line name and corresponding fraction type for sample CR-27.

Mound name	Line name	Fraction type
CR-27- Reference Mound	Line A	Fine to medium grain
	Line B	Fine to medium grain
	Line C	Fine to medium grain
	Line D	Medium to coarse grain
	Line E	Coarse grain
CR-27- Reference Mound (Frantz separated)	Line A	Ferromagnetic fraction
	Line B	Magnetic fraction at 0.1
	Line C	Magnetic fraction at 0.2
	Line D	Magnetic fraction at 0.3
	Line E	Magnetic fraction at 0.4
	Line F	Nonmagnetic fraction at 0.4
CR-27- < 250 µm (Frantz separated)	Line A	Ferromagnetic fraction
	Line B	Magnetic fraction at 0.1
	Line C	Magnetic fraction at 0.2
	Line D	Magnetic fraction at 0.3
	Line E	Magnetic fraction at 0.4
	Line F	Nonmagnetic fraction at 0.4
CR-27- < 150 µm (Frantz separated)	Line A	Ferromagnetic fraction
	Line B	Magnetic fraction at 0.1
	Line C	Magnetic fraction at 0.2
	Line D	Magnetic fraction at 0.3
	Line E	Magnetic fraction at 0.4
	Line F	Nonmagnetic fraction at 0.4

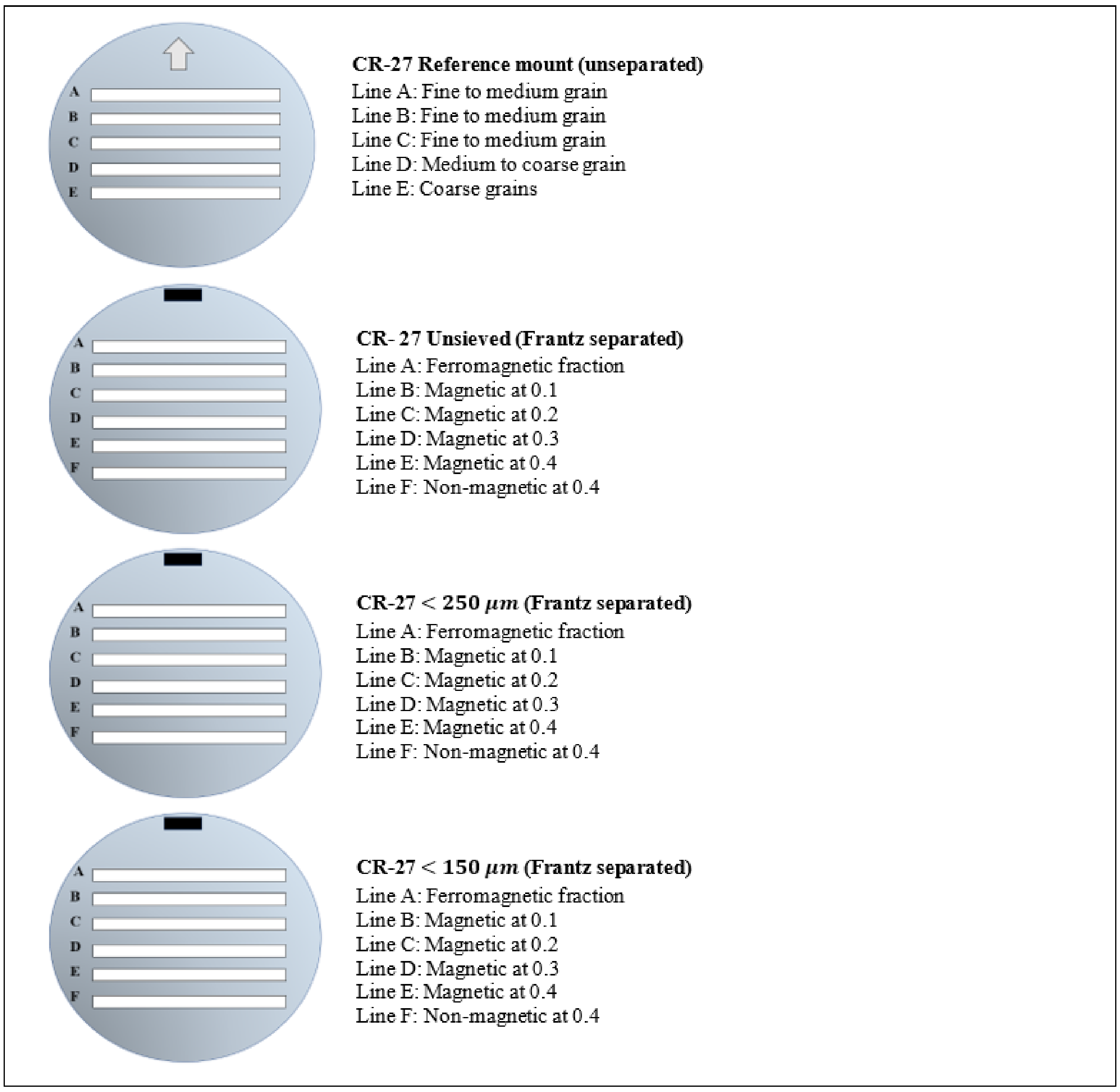

CR-27 Reference mount (unseparated)
Line A: Fine to medium grain
Line B: Fine to medium grain
Line C: Fine to medium grain
Line D: Medium to coarse grain
Line E: Coarse grains

CR- 27 Unsieved (Frantz separated)
Line A: Ferromagnetic fraction
Line B: Magnetic at 0.1
Line C: Magnetic at 0.2
Line D: Magnetic at 0.3
Line E: Magnetic at 0.4
Line F: Non-magnetic at 0.4

CR-27 < 250 μm (Frantz separated)
Line A: Ferromagnetic fraction
Line B: Magnetic at 0.1
Line C: Magnetic at 0.2
Line D: Magnetic at 0.3
Line E: Magnetic at 0.4
Line F: Non-magnetic at 0.4

CR-27 < 150 μm (Frantz separated)
Line A: Ferromagnetic fraction
Line B: Magnetic at 0.1
Line C: Magnetic at 0.2
Line D: Magnetic at 0.3
Line E: Magnetic at 0.4
Line F: Non-magnetic at 0.4

Figure 2.6: Map of the mounds for sample CR-27 with fraction type based on grain size

Table 2.3: List of mound names with the line name and corresponding fraction type for sample CR-18.

Mound name	Line name	Fraction type
CR-18- Reference Mound	Line A	Fine to medium grain
	Line B	Fine to medium grain
	Line C	Fine to medium grain
	Line D	Medium to coarse grain
	Line E	Coarse grain
CR-18- Reference Mound (Frantz separated)	Line A	Ferromagnetic fraction
	Line B	Magnetic fraction at 0.1
	Line C	Magnetic fraction at 0.2
	Line D	Magnetic fraction at 0.3
	Line E	Magnetic fraction at 0.4
	Line F	Nonmagnetic fraction at 0.4
CR-18- < 250 µm (Frantz separated)	Line A	Ferromagnetic fraction
	Line B	Magnetic fraction at 0.1
	Line C	Magnetic fraction at 0.2
	Line D	Magnetic fraction at 0.3
	Line E	Magnetic fraction at 0.4
	Line F	Nonmagnetic fraction at 0.4
CR-18- < 150 µm (Frantz separated)	Line A	Ferromagnetic fraction
	Line B	Magnetic fraction at 0.1
	Line C	Magnetic fraction at 0.2
	Line D	Magnetic fraction at 0.3
	Line E	Magnetic fraction at 0.4
	Line F	Nonmagnetic fraction at 0.4

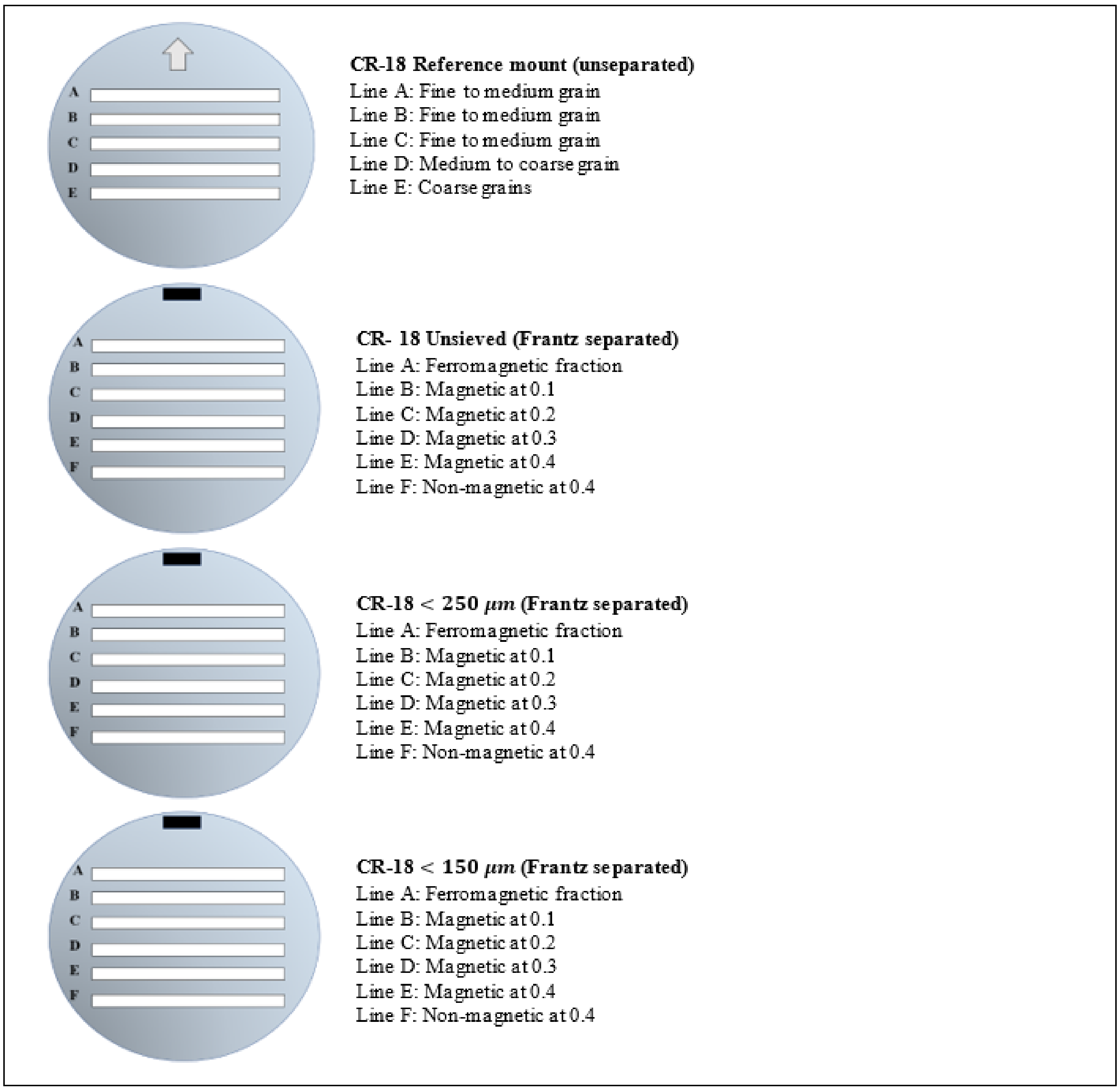

CR-18 Reference mount (unseparated)
Line A: Fine to medium grain
Line B: Fine to medium grain
Line C: Fine to medium grain
Line D: Medium to coarse grain
Line E: Coarse grains

CR- 18 Unsieved (Frantz separated)
Line A: Ferromagnetic fraction
Line B: Magnetic at 0.1
Line C: Magnetic at 0.2
Line D: Magnetic at 0.3
Line E: Magnetic at 0.4
Line F: Non-magnetic at 0.4

CR-18 < 250 μm (Frantz separated)
Line A: Ferromagnetic fraction
Line B: Magnetic at 0.1
Line C: Magnetic at 0.2
Line D: Magnetic at 0.3
Line E: Magnetic at 0.4
Line F: Non-magnetic at 0.4

CR-18 < 150 μm (Frantz separated)
Line A: Ferromagnetic fraction
Line B: Magnetic at 0.1
Line C: Magnetic at 0.2
Line D: Magnetic at 0.3
Line E: Magnetic at 0.4
Line F: Non-magnetic at 0.4

Figure 2.7: Map of the mounds for sample CR-18 with fraction type based on grain size.

Table 2.4: List of mound names with the line name and corresponding fraction type for sample CR-03.

Mound name	Line name	Fraction type
CR-03- Reference Mound	Line A	Fine to medium grain
	Line B	Fine to medium grain
	Line C	Fine to medium grain
	Line D	Medium to coarse grain
	Line E	Coarse grain
CR-03- Reference Mound (Frantz separated)	Line A	Ferromagnetic fraction
	Line B	Magnetic fraction at 0.1
	Line C	Magnetic fraction at 0.2
	Line D	Magnetic fraction at 0.3
	Line E	Magnetic fraction at 0.4
	Line F	Nonmagnetic fraction at 0.4
CR-03- < 250 µm (Frantz separated)	Line A	Ferromagnetic fraction
	Line B	Magnetic fraction at 0.1
	Line C	Magnetic fraction at 0.2
	Line D	Magnetic fraction at 0.3
	Line E	Magnetic fraction at 0.4
	Line F	Nonmagnetic fraction at 0.4
CR-03- < 150 µm (Frantz separated)	Line A	Ferromagnetic fraction
	Line B	Magnetic fraction at 0.1
	Line C	Magnetic fraction at 0.2
	Line D	Magnetic fraction at 0.3
	Line E	Magnetic fraction at 0.4
	Line F	Nonmagnetic fraction at 0.4

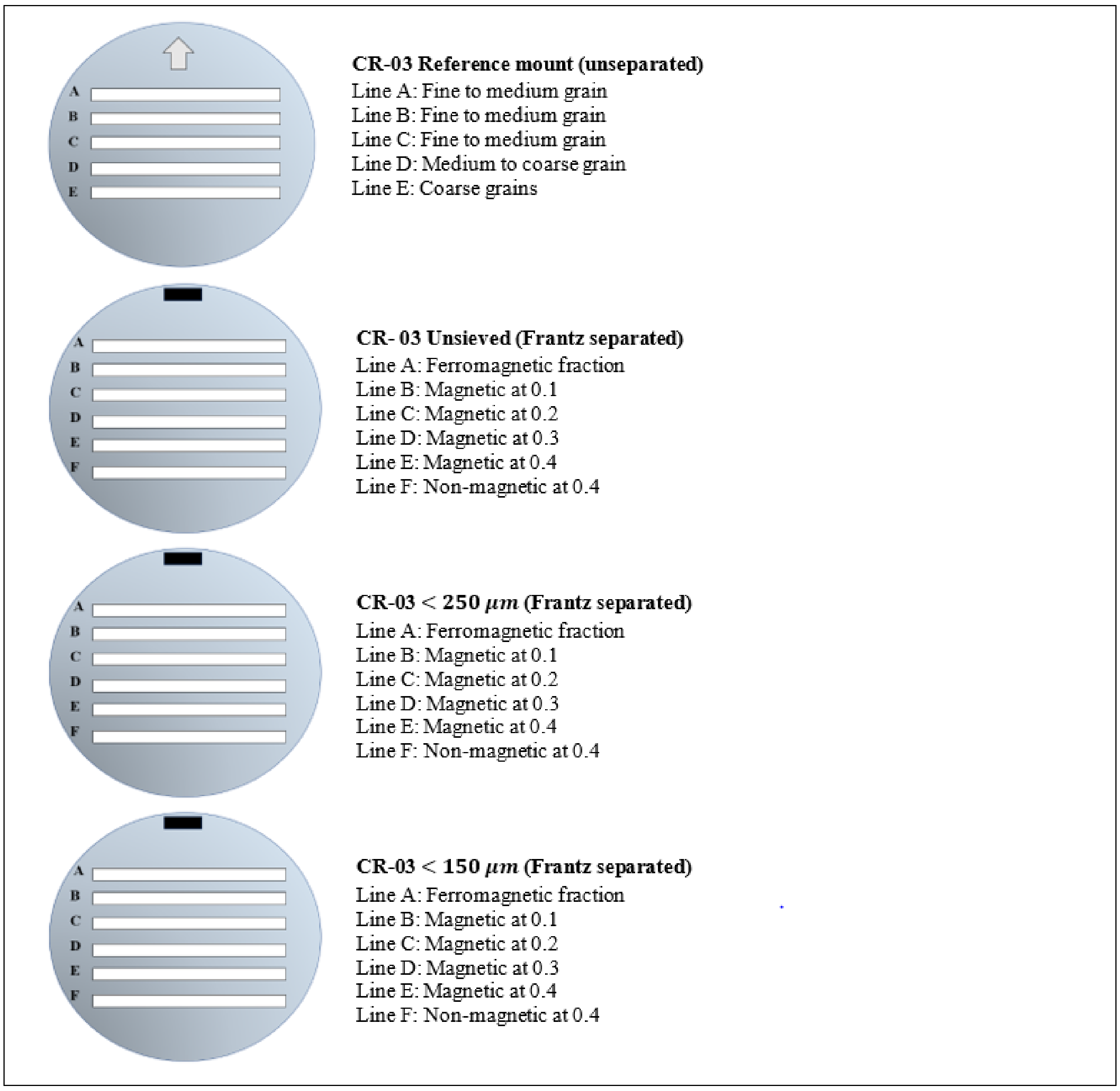
A
B
C
D
E
CR-03 Reference mount (unseparated)
Line A: Fine to medium grain
Line B: Fine to medium grain
Line C: Fine to medium grain
Line D: Medium to coarse grain
Line E: Coarse grains
A
B
C
D
E
F
CR- 03 Unsieved (Frantz separated)
Line A: Ferromagnetic fraction
Line B: Magnetic at 0.1
Line C: Magnetic at 0.2
Line D: Magnetic at 0.3
Line E: Magnetic at 0.4
Line F: Non-magnetic at 0.4
A
B
C
D
E
F
CR-03 < 250 μm (Frantz separated)
Line A: Ferromagnetic fraction
Line B: Magnetic at 0.1
Line C: Magnetic at 0.2
Line D: Magnetic at 0.3
Line E: Magnetic at 0.4
Line F: Non-magnetic at 0.4
A
B
C
D
E
F
CR-03 < 150 μm (Frantz separated)
Line A: Ferromagnetic fraction
Line B: Magnetic at 0.1
Line C: Magnetic at 0.2
Line D: Magnetic at 0.3
Line E: Magnetic at 0.4
Line F: Non-magnetic at 0.4

Figure 2.8: Map of the mounds for sample CR-03 with fraction type based on grain size.

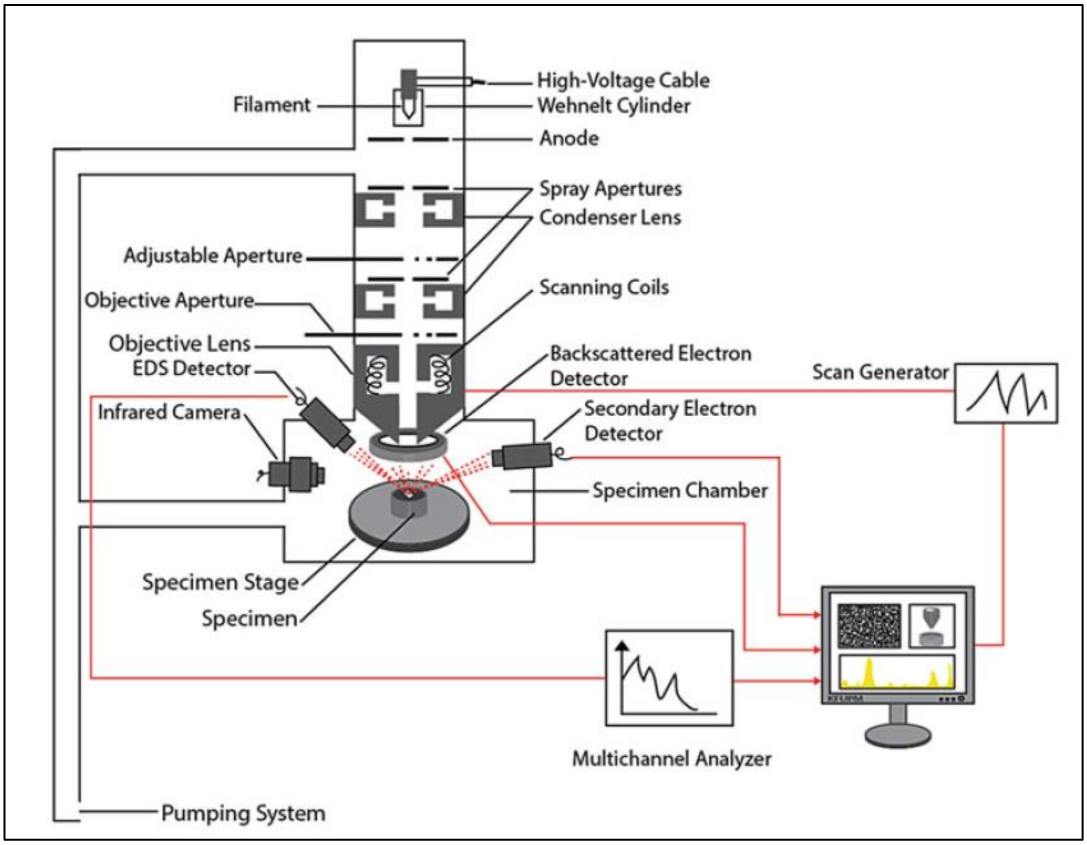

Figure 2.9: Graphical illustration of the scanning electron microscope (Ul-Hamid, 2018).

2.2.4 Magnification

The electron beam focused into the finer probe hits the surface of the specimen in a single location; therefore, to obtain an image, this probe is scanned over the sample surface in the area of interest. The produced image of the scanned area is then displayed on the screen (Figure 2.10). Magnification is the ratio between the length of the scan on the monitor screen to that of the sample.

$$\text{Magnification} = \frac{\text{Length of scan on monitor screen}}{\text{Length of scan on the sample surface}} = \frac{\text{L}_{\text{monitor screen}}}{\text{L}_{\text{sample}}}$$

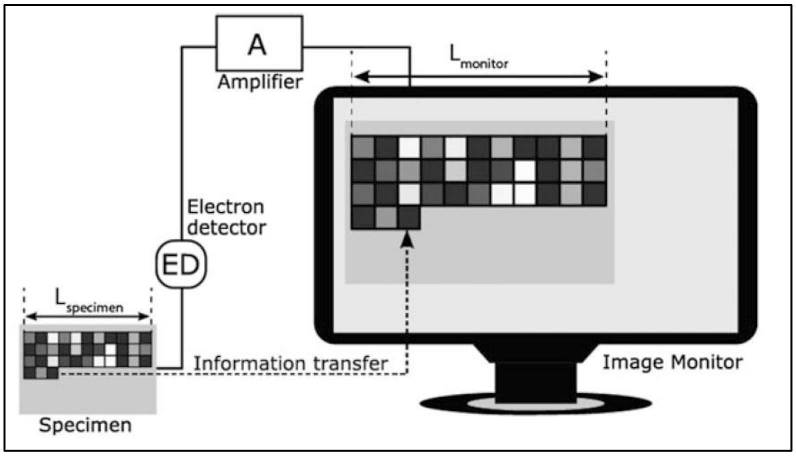

Figure 2.10: Illustration of magnification, in typical SEM (Ul-Hamid, 2018).

Obviously, the display screen's length is fixed; therefore, magnification is controlled by changing the scan length on the specimen surface utilizing scanning coils. Thus, the smaller the scan area over the sample larger the magnification is attained and vice versa (Ul-Hamid, 2018).

2.2.5 Resolution

It is the amount of tiny detail which is clearly identifiable in the image. An image's resolution is dependent on the diameter of the electron beam and the interaction of electrons with a specimen. The various instrumental factors aid in determining the beam diameter; consequently, it is possible to condense the beam's diameter to a few nanometers to get better resolution. Nevertheless, in many cases, a higher resolution is not required so, a larger beam diameter can be used. Under favorable conditions, the resolution limit, defined by the interaction of electron beam and specimen, ranges from 1 μm in x-ray imaging and <10 nm for SE imaging. In contrast, the maximum gainable resolution in digital imaging depends on pixel size instead. A short working distance is optimal for good resolution in SE images, but it is not promising in x-ray images, especially when it is less than specific values (Reed, 2005).

2.2.6 Signal Detectors

The detector is the instrument that receives the signal coming from the specimen surface (Figure 2.11) and converts it into an electrical pulse. This electrical pulse is further processed and then finally displayed on a monitor in the form of an SEM image or Energy Dispersive Spectrum (EDS) (Ul-Hamid, 2018). The scanning electron microscope is commonly armed with at least one or more detectors responsible for sensing signals coming from beam-specimen interaction. The most noticeable signals are backscattered electrons (BSE), secondary electrons (SE), and x-rays. The measurement of these signals concerning the beam location reveals valuable inFormation about various properties of the specimen (Goldstein et al., 2018). The Secondary Electron (SE) detector and Backscattered Electron (BSE) detector are responsible for registering secondary electrons and backscattered electrons. In contrast, the Energy Dispersive Spectroscopy (EDS) detector detects x-ray signals (Ul-Hamid, 2018).

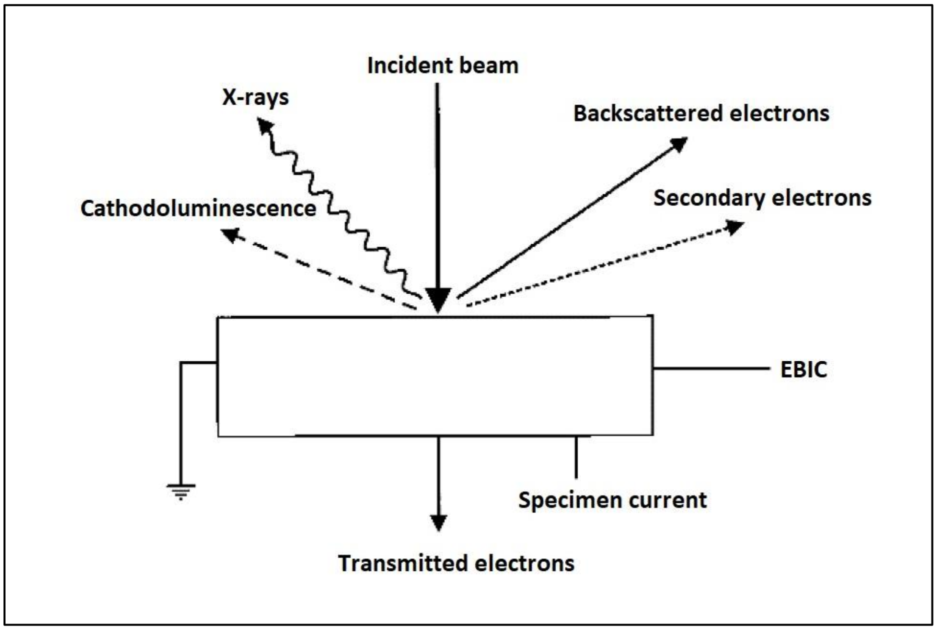

Figure 2.11: Different signals generated as a result of interaction between an electron beam and specimen surface. (after Goodhew & Humphreys, 2000).

2.2.7 Secondary Electron Detectors

In SEM, the most common detector in service for recording the secondary electrons is the Everhart-Thornley detector (ET). This detector mainly consists of a 'scintillator' with a thin metal coating and high positive potential, making it a valued tool for detecting low-energy secondary electrons. The mesh, also known as a "Faraday cage," surrounds the scintillator, which can be biassed to regulate electron collection (Goldstein et al., 2018). The application of positive bias (e.g., 200 V) results in the attraction of secondary electrons, which then pass through mesh holes and are finally directed toward the scintillator (Figure 2.12). The bombardment of electrons on the scintillator generates light. This light signal is transformed into an electrical signal utilizing a photomultiplier, amplified to produce an image on the viewing screen (Reed, 2005). The direct secondary electron signals are low; however, the large number of indirect SE and BSE distorts the resolution. Therefore, for high-resolution imaging, Through The Lens (TTL) detector is used (Ul-Hamid, 2018).

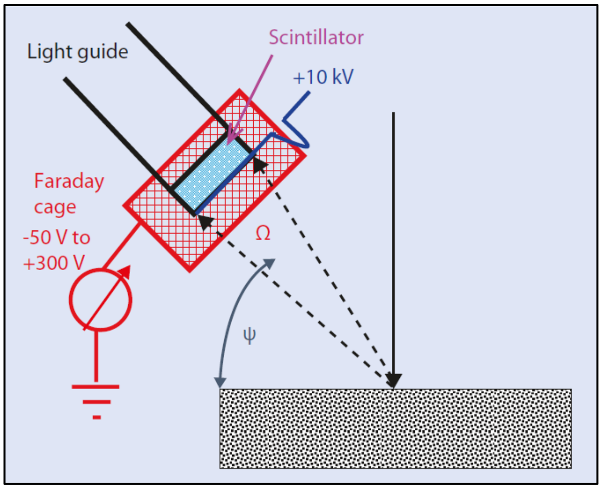

Figure 2.12: Graphical illustration of different elements constituting the Everhart-Thornley detector (Goldstein et al., 2018).

2.2.8 Backscattered Electron Detector

When the electron beam strikes the sample surface, a massive portion of the incident electron beam entirely reverses its original direction due to experiencing sufficient scattering events. This causes the coming back of these electrons to the entrance surface and withdrawal from the specimen and is acknowledged as backscattered electrons (BSE) (Goldstein et al., 2018). The energy emitted by backscattered electrons (BSE) is much higher than the secondary electrons (SE). This significant difference in energy makes it easier to detect them by modifying the Everhart-Thornley detector (ET). The application of slight negative bias (-50 eV) discards the secondary electrons and faciltates in collection of backscattered electrons (Ul-Hamid, 2018). The backscattered electrons can be detected more efficiently by the 'Robinson' detector, which employs a scintillator placed immediately above the sample. The sample is commonly mounted on a folding arm with a hole allowing the passage of electron beam (Figure 2.13 a). The noise-free backscattered electrons (BSE) can be collected due to the large solid angle (Reed, 2005). Another most common way to detect BSE is by using solid-state detectors (SSD), which comprise a silicon diode mounted just underneath the objective lens. The diode makes $\mathrm{p-n}$ type junction or sectors by which conduction of electrons and holes take palce (Egerton, 2016). This arrangmenrt produces the signal by combining the output of the sectors in several ways. Compare to the scintillators, the solid-state detectors (Figure 2.13 b) have a lower response which makes them unfavorable for fast scanning mode (Reed, 2005).

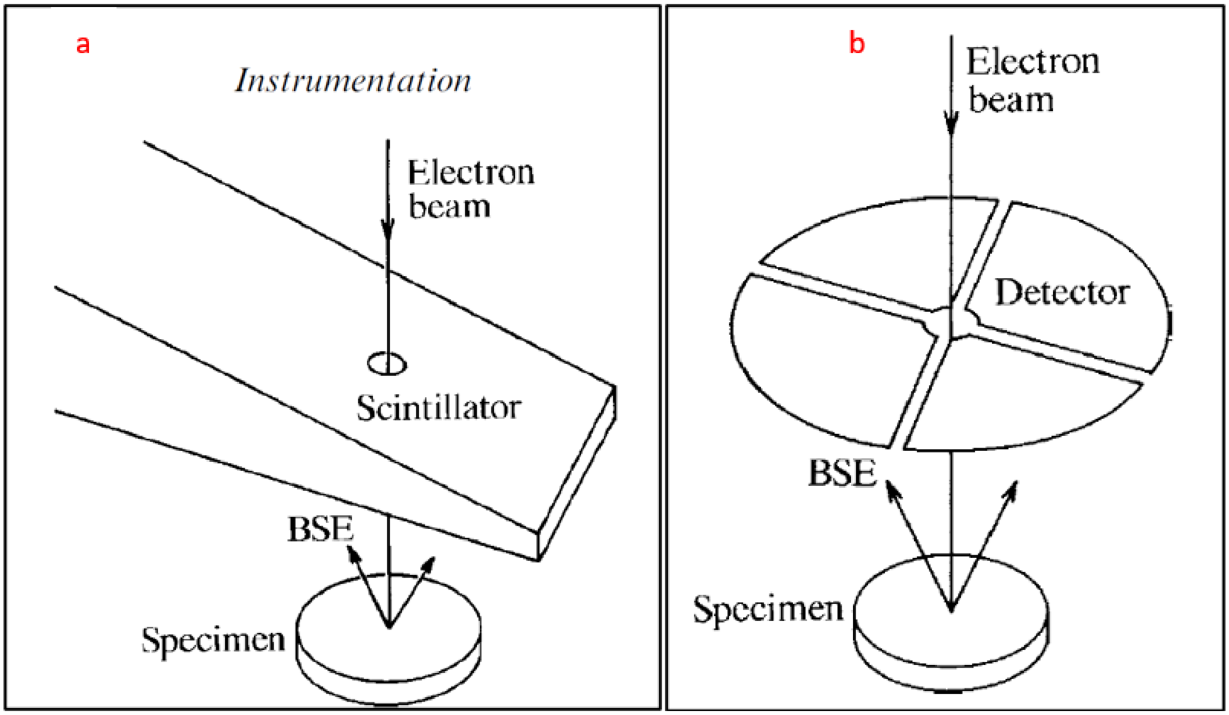

Figure 2.13: An illustration of Robinson detector (a) and solid-state detector (b) (Reed, 2005).

2.2.9 Energy dispersive spectroscopy (EDS) detector

The electron beam interaction with specimen material produces characteristic X-rays and background x-rays (white radiations), which in combination makes an x-ray signal. The energy dispersive x-ray spectrometer (EDS) is the most commonly used detector to collect the x-ray signal, measure energy and intensity distribution. The x-ray signal is analyzed to identify elements and their respective concentration in the targeted region (Ul-Hamid, 2018). In the EDS system, a small cylinder of p-type silicon and lithium in silicon diode makes up the Si (Li) detector, as shown in Figure 2.14. This Si (Li) detector collects the X-ray photons and creates a specific number of electron-hole pairs. Higher photon energies correspond to more electron-hole pairs and vice versa. The number of electron-hole pairs generated can be used to separate x-ray photons according to their energy levels (Leng, 2013). Signal pulses coming from the detector are amplified and converted to a spectrum by a multichannel pulse height analyzer. The spectrums obtained from a target area can be compared to the reference spectrums for identifying minerals; however, one needs to be very careful as the detector's efficiency varies considerably due to different factors (Reed, 2005).

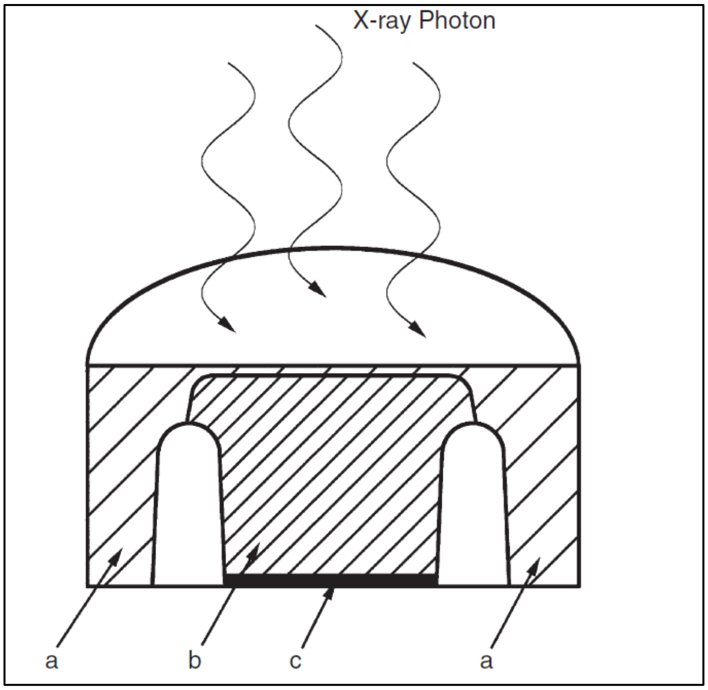

Figure 2.14: An illustration of the Si(Li) detector and electron-hole pairs (Leng, 2013).

2.2.10 Purpose of the FE-SEM and EDS method

The main aim of using FE-SEM is to take backscattered images of the mineral's grain mounted on the tape to get information about its size, shape, inclusions, and phases. The backscattered detector is capable of producing contrast images of the mineral grain based on elemental composition. The EDS detector facilitates the identification of the mineral by giving its elemental composition in the form of spectrums. These all specifications make it a handy machine for characterizing and identifying the minerals.

2.2.11 Technical specifications

The Zeiss Supra 35VP Scanning electron microscope installed at UiS was utilized for this project (Figure 2.15 a). The SEM is equipped with the backscattered detector, secondary electron detector, cathodoluminescence detector, and EDS detector of type EDAX Octane Elite 25. The carbon-coated sample mounts were placed on the sample holder one at a time, and the carbon tape was stuck on all sides of the sample to prevent overcharging. The sample chamber was opened to place the sample under vacuum in FE-SEM (Figure 2.15 b). The acceleration voltage of 20 kV was applied, and then a secondary electron image was first used to adjust focus and stigmatism. Later on, the backscattered electron detector was turned on, and again brightness, contrast, and magnification were adjusted to get decent quality images.

For BSE images, the working distance was set to 10 µm and aperture size to 30 µm. The BSE images of each fraction were captured, and then the same image area was imported to TEAM software for hitting the points to collect the EDS spectrum. Finally, the spectrum was compared to reference spectrums to interpret the mineral type.

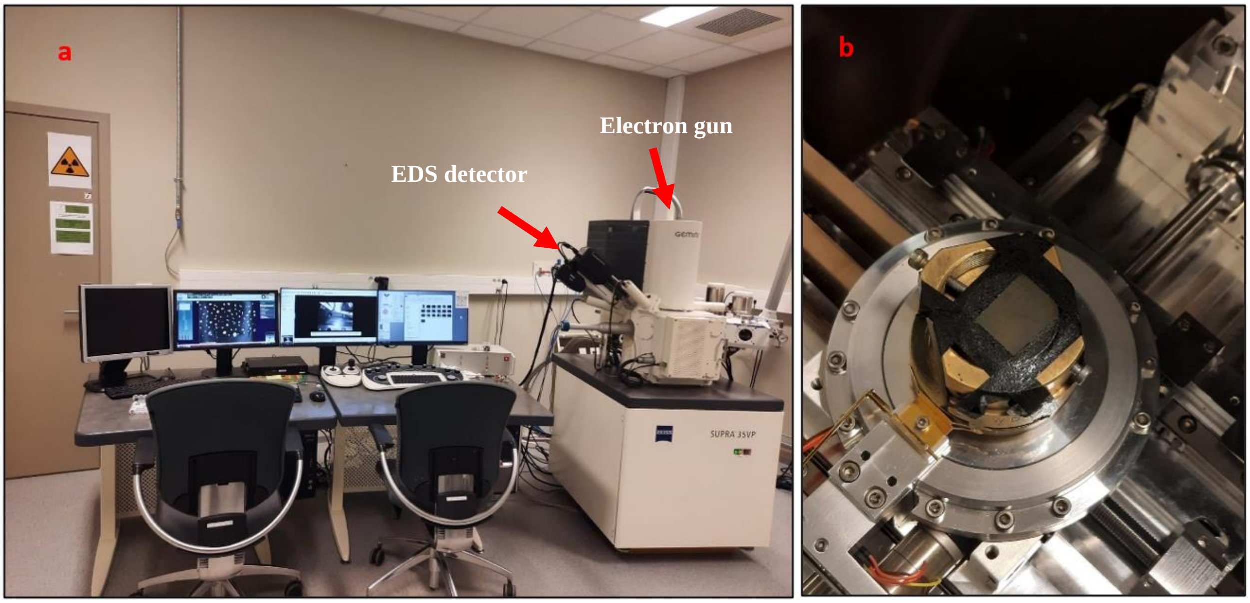

Figure 2.15: Zeiss Supra 35VP Scanning electron microscope installed at UiS (a) placing of carbon-coated sample mound at stage inside sample chamber of SEM (b).

2.3 X-ray diffraction analysis (XRD)

2.3.1 Sample preparation

2.3.1.1 Milling

For XRD analysis, three reference samples, namely CR-03, CR-27, and CR-18, were prepared. These samples have not been separated into Frantz, and also, they have not been passed through sieves. To obtain reliable results, the samples were milled before going for XRD. To get excellent results, the samples were placed in an agate-mortar and milled to make grains in a more acceptable size range (Figure 2.16 a). All three samples were then laid into plastic containers (Figure 2.16 b). The agate-mortar was cleaned with water and ethanol and then dried with compressed air for milling the following sample. To ensure the random orientation of material, samples were distributed evenly and compacted lightly into the sample holders using the spatula to spread the milled powder. Excess sample material was also removed. Finally, the samples were placed into an X-ray diffraction machine.

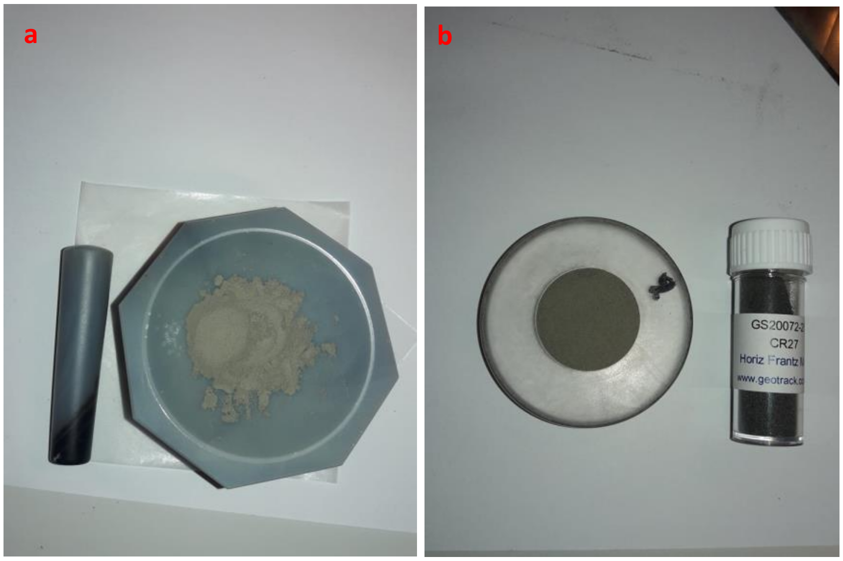

Figure 2.16: An agate-mortar used for milling the sample (a) plastic container used for placing the powder material inside the X-ray diffractometer (b).

2.3.2 Theoretical background

X-ray diffraction by crystals is the most widely used technique in different areas, particularly for material characterization since its discovery in 1912 (Leng, 2013). This method was initially employed by William Henry Bragg as a tool to study the basic crystallographic structures using X-rays. Neil Bohr also proposed his atomic model by analyzing the X-ray intensities reflected by different crystal planes and thus leading to the concept of chemical bonding (Hessenbruch, 2002).

The X-ray diffraction can be classified into two types, i.e., photographic diffraction method, which is a less common method, and spectroscopic, which is extensively used and also known as X-ray powder diffractometry or X-ray diffractometry (Leng, 2013). For this thesis project, the spectroscopic diffraction method will be used.

2.3.3 X-rays generation

The X-rays are produced in a cathode ray tube in a conventional X-ray diffractometer (XRD) (Figure 2.17). When the filament, also known as the cathode, is heated at a remarkably elevated temperature, free electrons production occurs. The application of a high voltage between cathode and target (anode) accelerates the negatively charged electrons to high energy (Nesse, 2000). The collision of these high-energy electrons with the target (anode) decelerates them rapidly and thus converting their kinetic energy to the energy of X-ray radiation (Leng, 2013).

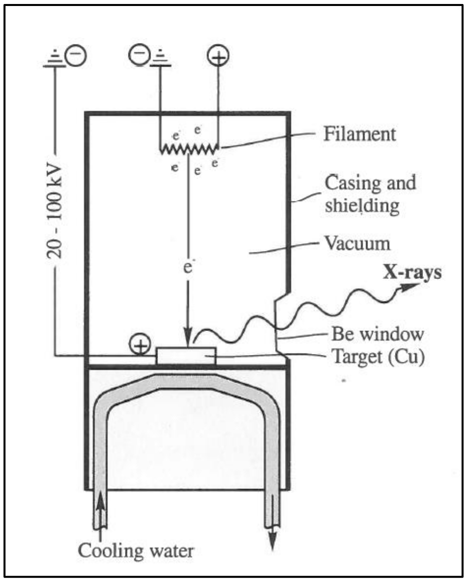

Figure 2.17: Conceptual illustration of cathode ray tube (Nesse, 2011).

If the electron strikes with the target and gets decelerate without changing the configuration of atoms, a continuous spectrum of X-rays is produced. Since electrons go through series of collisions, therefore, the energy contained by each electron is released in the form of radiations with a wide range of wavelengths (Figure 2.18 a).

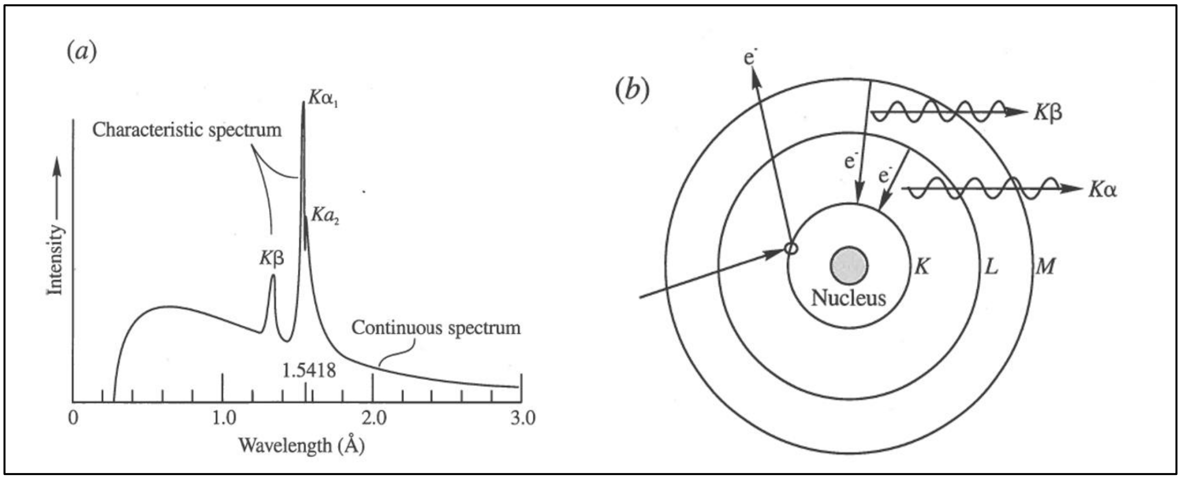

Figure 2.18: An illustration of intensity and wavelength of the characteristic and continuous X-rays spectrum (a) General model illustrating the production of characteristic X-rays (b) (Nesse, 2011).

On the other hand, when the incident high energy electrons eject an electron from the innermost K shell of target atoms, the vacant space is filled by another electron jumping from high energy orbit and releasing energy in the form of the characteristic spectrum of X-rays (Figure 2.18 b). The energy of X-ray radiation is the difference between the energy of a K-shell and an outer shell (Nesse, 2000).

There are two methods for the detection of X Rays.

1) Photographically
2) Electronically

The first method is suitable for medical purposes; however, the second method is appropriate to detect x-rays, especially when studying the minerals (Nesse, 2000).

2.3.4 Braggs law

Like visible light, x-rays are also electromagnetic waves, but their wavelength is much shorter when compared to the visible light spectrum. The phenomena of X-ray diffraction are controlled by wave interference. When the waves are in phase, it results in constructive interference, whereas destructive interference occurs when the waves are out of phase. The two different waves X and Y, are in phase when they satisfy the following relation (Leng, 2013).

$$n\lambda = 2d\sin\theta \qquad (2.1)$$

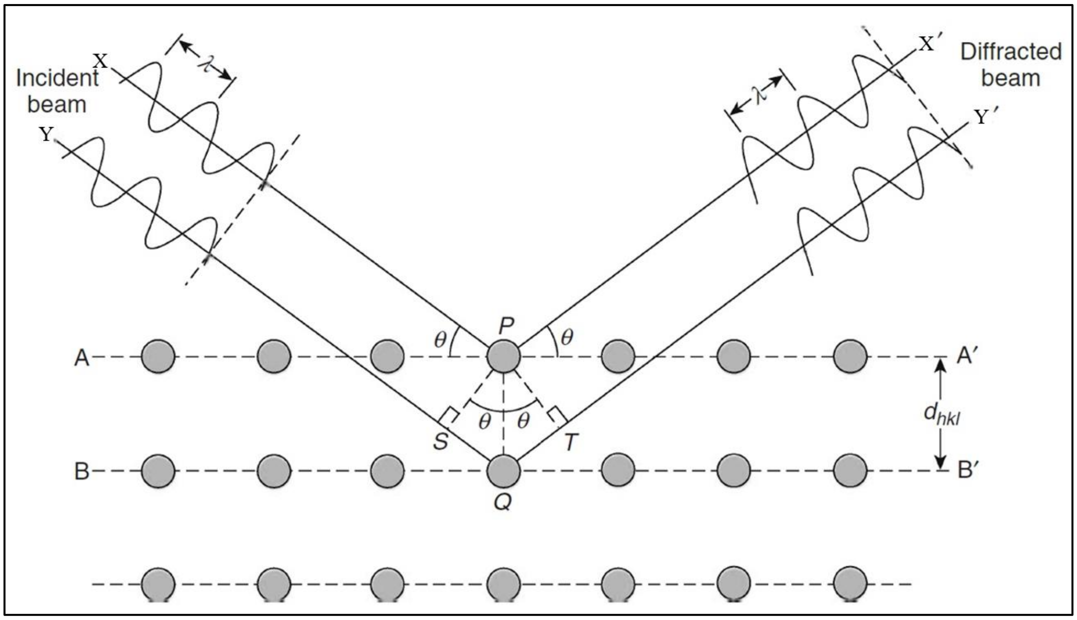

Figure 2.19: The diffraction of ray X and Y according to Braggs law (nλ=2dsinθ), modified after (Leng, 2013).

This relation is derived by estimating the path difference between two waves in Figure 2.19. The path difference between the two X-ray beams depends on the incident angle (θ) and the separation (d) between parallel crystal planes.

Based on the Braggs law, the information about spacing between atomic planes of a crystal can be obtained by sensing constructive interference at a known incident angle and wavelength λ of the incident beam. The knowledge of spacing between atomic planes reveals the material's crystal structure (Leng, 2013).

2.3.5 Instrumentation

The X-ray diffractometer is designed to detect X-ray diffraction from atomic planes of crystallographic materials. It registers the diffraction intensity in the range of diffraction angle (2θ). The internal geometrical arrangement of the X-ray source, specimen, and detector is shown in Figure 2.20. the X-ray tube produces the X-ray radiations that pass through the solar slits made up of metals to avoid beam divergence in the perpendicular direction of the figure plane (Figure 2.20). The diverging beam passing through solar slits hits the specimen surface and diffracts from crystal planes of material. These diffracted X-rays form a convergent beam at receiving slit before reaching a detector. The monochromatic filter is also installed at a passage of diverging beam to reduce the background noise in the radiations (Leng, 2013)

Comparing the diffraction pattern generated by a specimen with already known spectra aids in identifying crystalline material. The modern XRD equipment uses computer software to perform spectra matching of crystalline material (Leng, 2013).

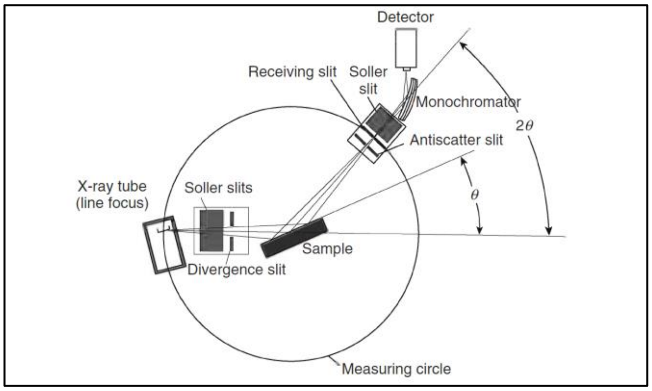

Figure 2.20: The arrangement of different elements such as Divergence silt, Soller slits, and X-ray tube in an X-ray diffractometer (Leng, 2013).

2.3.6 Purpose of the method

X-ray diffraction is the most effective technique for defining the crystal structure of crystalline substances. It identifies the chemical compounds from their crystallographic planes instead of chemical composition. This capability makes it an excellent tool for distinguishing the polymorph materials which have the same chemical composition but different crystallographic structures (Leng, 2013). The XRD technique is also used to differentiate calcite and aragonite, which exist in two dissimilar crystal structures having identical chemical compositions (Gopi & Subramanian, 2012).

2.3.7 Technical specifications

The XRD analysis was carried for only two samples at UiS by Staff Engineer Caroline Rudd. The X-ray diffractometer used for this analysis is Bruker D8 ADVANCE Eco (Figure 2.21). The software DIFFRAC.SUITE EVA recorded the X-ray diffraction patterns for powdered material and compared them with reference spectra to identify minerals. A voltage 40kV and current of 25 mA was set along with increment to 0.010 and time to $0.2\ \mathrm{second/step}$. The slit was adjusted to 0.6 mm and diffraction angle range $2\theta = 4 - 70°$, whereas CuK (alpha) radiation was applied for generating diffraction beams.

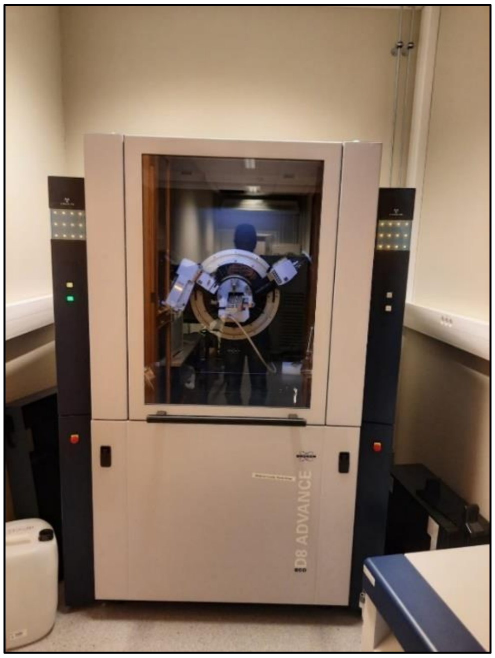

Figure 2.21: The Bruker D8 ADVANCE Eco X-ray diffractometer installed at UiS.

3 RESULTS

The results are divided into two analytical methods: FE-SEM, XRD. Data obtained from these methods is combined and analyzed in chapter 4, “Discussion and implications of the results”. results”.

3.1 Results from FE-SEM

3.1.1 Backscattered electron (BSE) images

To observe the mineralogical variations, BSE images for all samples and their respective fraction have been captured. The analysis aided to hit the right EDS spot on the basis of variation in brightness. Furthermore, this analysis helped in determining the composition of locked fragment. The results from BSE analysis can be seen in Appendix B. BSE images as an example are shown in Figure 3.1 and Figure 3.2 where the difference in brightness of grains is obvious. The BSE images also helped to visualize and understand nature of lithoclasts found in different magnetic fractions.

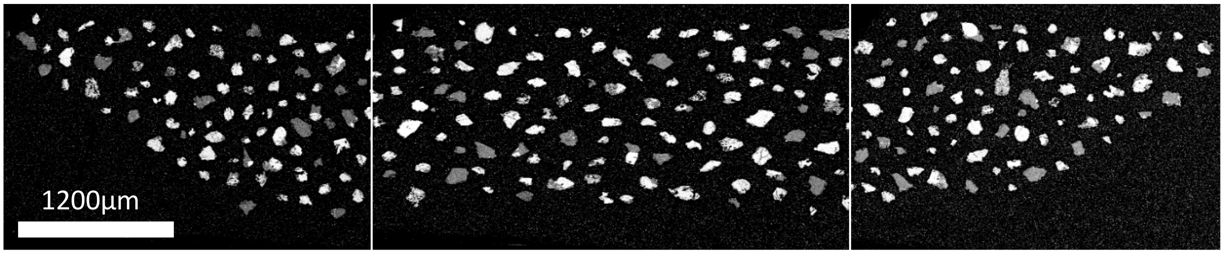

Figure 3.1: The NM (non-magnetic) fraction retrieved at 0.4 A, for sample CR-18 (<150µm)

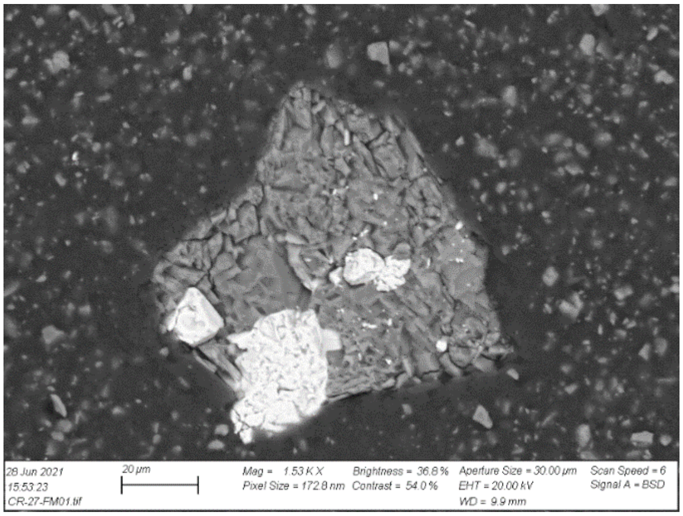

Figure 3.2: The locked fragment (lithoclast) comprising of albite (dark) and hematite (light).

3.2 Identification and semi-quantification of minerals

The minerals are identified with FE-SEM-EDS based on the spectrums (one shown as an example in Figure 3.3) in Appendix A. The non-heavy minerals (density < 2.9 g/cm^3) in samples are albite, anorthite, Fe bearing anorthite, anorthoclase, chlorite, glauconite, microcline, muscovite, orthoclase, phlogopite, and quartz. In contrast, almandine, apatite-F, barite, goethite, hematite, tin bearing hematite, ilmenite, monzonite, rutile, titanite, tourmaline, and zircon are some heavy minerals (density > 2.9 g/cm^3) identified in three samples. All the minerals identified for each sample type and their separated fractions are shown Table 3.1, Table 3.2, and Table 3.3. Percentage of each mineral in a certain fraction is estimated based on the manual spot analysis of 50-100 grains.

The Tables representing heavy minerals in each fraction can be seen in Appendix C. The values are in % and characterize only % of HM in the sample (minerals with density < 2.9 g/cm^3 are not counted in).

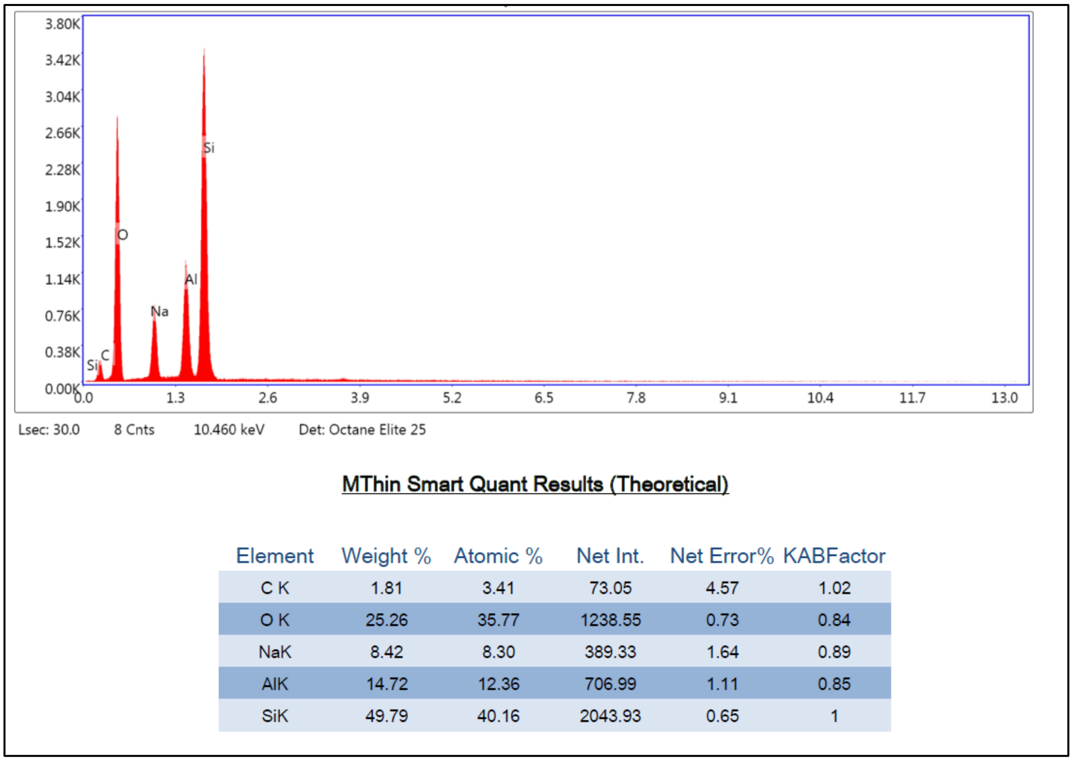

MThin Smart Quant Results (Theoretical)

Element	Weight %	Atomic %	Net Int.	Net Error%	KABFactor
C K	1.81	3.41	73.05	4.57	1.02
O K	25.26	35.77	1238.55	0.73	0.84
NaK	8.42	8.30	389.33	1.64	0.89
AlK	14.72	12.36	706.99	1.11	0.85
SiK	49.79	40.16	2043.93	0.65	1

Figure 3.3: EDS spectra for Albite.

Table 3.1: List of minerals identified using FE-SEM and EDS analysis for sample CR-27. Values are in % and represents % of total minerals identified

CR-27 (amphibolite)

			Reference	**Un-sieved (Frantz separated)**						**Less than 250 µm (Frantz separated)**						**Less than 150 µm (Frantz separated)**					
#	**Color code**	**Mineral**		**FM**	**0.1 A**	**0.2 A**	**0.3 A**	**0.4 A**	**NM at 0.4**	**FM**	**0.1 A**	**0.2 A**	**0.3 A**	**0.4 A**	**NM at 0.4**	**FM**	**0.1 A**	**0.2 A**	**0.3 A**	**0.4 A**	**NM at 0.4**
1	■	Albite	1.59	14.60	9.01	15.90	11.85	22.05	12.06	23.07	13.11	14.66	26.82	12.16	18.05	10.98	22.00	10.22	16.86	17.91	20.75
3	■	Andalusite																			
4	■	Anorthite																			
5	■	Anorthite Fe	8.30	17.97	9.01	28.03	30.37			26.92	24.59	16.00	17.07	24.32	6.94	10.98	11.00	27.00	38.55	1.49	
6	■	Anorthoclase	0.31	2.24	0.81	0.75	1.48	0.73													
7	■	Chlorite	8.94	7.86	2.45	7.57	5.18	2.20	3.44	7.69	11.47	17.33	9.75	14.86	12.50	7.69	9.00	17.04			
8	■	Glauconite																			
9	■	Microcline																			
10	■	Muscovite	2.23				0.74									3.29		1.13		1.49	
11	■	Orthoclase														1.09					
12	■	Phlogopite	36.10	14.60	2.45	24.24	4.44	2.20		13.46	24.59	20.00	4.87	1.35	9.722	2.19	2.00	20.45	6.02	4.47	
13	■	Quartz	1.59	2.24	8.19	6.81	11.11	11.76	12.06	9.61		5.33	6.09	8.10	18.05	3.29	5.00	10.22	9.63	8.95	3.77
14	■	Almandine																			
15	■	Apatite-F	3.19	1.12			1.48	5.88	22.41							2.19	2.00			11.94	26.41
16	■	Barite																			
17	■	Goethite																			
18	■	Hematite	0.31	10.11	4.91	0.75				3.84						2.19	1.00				
19	■	Hematite-Tin	8.62	19.10	46.72	6.06				5.76	9.83	12.00	10.97	2.70		24.17	36.00	1.13			
20	■	Ilmenite	18.84	2.24	8.19	1.51	1.4	1.4		3.84	4.91	5.33		1.35		13.18	7.00	3.40	1.20	1.49	
21	■	Monzonite																			
22	■	Rutile	9.58	6.74	8.19	7.57	31.85	52.94	49.98	5.76	9.836	9.33	23.17	33.78	33.33	18.68	5.00	9.09	27.71	52.23	49.05
23	■	Titanite																			
24	■	Tourmaline																			
25	■	Zircon	0.31	1.12		0.75		0.73			1.63										
26	■	Unknown											1.21	1.35	1.38						
Total:			100.00	100.00	100.00	100.00	100.00	100.00	100.00	100.00	100.00	100.00	100.00	100.00	100.00	100.00	100.00	100.00	100.00	100.00	100.00
Lithoclasts (wt. % of total analyzed grains)			~27.15	~24.25						~51.92						~13.91					

Table 3.2: List of minerals identified using FE-SEM and EDS analysis for sample CR-03. Values are in % and represents % of total minerals identified.

CR-03 (phyllite)

			Reference	Un-sieved (Frantz separated)						Less than 250 µm (Frantz separated)						Less than 150 µm (Frantz separated)					
#	Color code	Mineral		FM	0.1 A	0.2 A	0.3 A	0.4 A	NM at 0.4	FM	0.1 A	0.2 A	0.3 A	0.4 A	NM at 0.4	FM	0.1 A	0.2 A	0.3 A	0.4 A	NM at 0.4
1	■	Albite	1.64				7.14	20.27		23.07	22.72	15.71						1.33	1.56	15.78	9.30
3	■	Andalusite	2.30			1.28								8.10		2.72					
4	■	Anorthite	0.98		1.36		9.52	4.05	5.76	21.15	11.36	4.28							2.34	13.15	9.30
5	■	Anorthite Fe																			
6	■	Anorthoclase																			
7	■	Chlorite	0.65														2.98		0.78		
8	■	Glauconite	0.65							7.69	2.27	32.85							1.56	0.87	
9	■	Microcline																1.33			
10	■	Muscovite																			
11	■	Orthoclase			1.36			2.70		7.69		1.42							0.78	2.63	
12	■	Phlogopite																			
13	■	Quartz	24.34	26.08	30.13	26.92	9.52	18.91	34.61		6.81	1.42	50.00	45.94	65.21	15.90	38.80	38.66	10.15	15.78	50.00
14	■	Almandine	5.26	1.44	1.36											6.81		16.00	21.87		
15	■	Apatite-F									2.27	1.42									
16	■	Barite																1.33			
17	■	Goethite	2.30	4.34	1.36	1.28					2.27					34.09	1.49				
18	■	Hematite	33.88	23.18	36.98	14.10	5.95	1.35		13.46	15.90	15.71	5.88	10.81	13.04	29.54	14.92	17.33	3.90		
19	■	Hematite-Tin	10.85	28.98	16.43	24.35	8.33	1.35		1.92			23.52	18.91	4.34	9.09	19.40	6.66	0.78	0.87	
20	■	Ilmenite	4.60	7.24	4.10	6.41				1.92	13.36	8.57	8.82	13.51	13.04	2.72	19.40	10.66	2.34		
21	■	Monzonite																			
22	■	Rutile	4.27	4.34	1.36	3.84	3.57	5.40	17.30	13.46	9.09	4.28	8.82		4.34		1.49	4.00	3.12	10.52	12.79
23	■	Titanite									2.27										
24	■	Tourmaline	3.28	1.44	1.36	15.38	44.04	33.78		9.61	9.09	14.28	2.94	2.70					46.87	35.08	5.81
25	■	Zircon	4.60	2.89	4.10	6.41	10.71	12.16	40.38								1.49	2.66	3.90	5.26	12.79
26	■	Unknown	0.32				1.19		1.92		2.27										
Total			100.00	100.00	100.00	100.00	100.00	100.00	100.00	100.00	100.00	100.00	100.00	100.00	100.00	100.00	100.00	100.00	100.00	100.00	100.00

Table 3.3: List of minerals identified using FE-SEM and EDS analysis for sample CR-18. Values are in % and represents % of total minerals identified

CR-18 (lavas)

#	Color code	Mineral	Reference	Un-sieved (Frantz separated)						Less than 250 µm (Frantz separated)						Less than 150 µm (Frantz separated)					
				FM	0.1 A	0.2 A	0.3 A	0.4 A	NM at 0.4	FM	0.1 A	0.2 A	0.3 A	0.4 A	NM at 0.4	FM	0.1 A	0.2 A	0.3 A	0.4 A	NM at 0.4
1	🟧	Albite	15.52	8.00	9.45	20.68	25.00	12.74	5.40	4.76	12.16	35.21	20.00	11.47	10.16		12.85	28.57	15.87	11.11	6.00
3	🟨	Andalusite	2.68			2.29										3.92	1.42			1.38	
4	🟥	Anorthite					1.25	1.96	1.35									1.42	1.58		
5	🟧	Anorthite Fe																			
6	🟥	Anorthoclase	2.98		5.40	3.44	10.00	1.96	1.35	1.58	1.35	5.63	1.53	1.63	1.69		1.42	4.28	7.93	2.77	
7	⬛	Chlorite																			
8	🟩	Glauconite		2.00		1.14												2.85			
9	🟩	Microcline			5.40	10.34	8.75	9.80		3.17	4.05	4.22	18.46	6.55	10.16	1.96	8.57	7.14	15.87	13.88	
10	⬜	Muscovite	2.68		4.05	8.04	1.25	0.98		1.58		5.63		6.55	3.38	1.96				2.77	
11	🟦	Orthoclase	10.44	2.00	2.70	6.89	7.50	0.98	1.35	4.76	2.70	1.40	3.07		1.6		4.28	8.57	3.17	2.77	
12	🟫	Phlogopite																			
13	🟦	Quartz	26.26	6.00	17.56	36.78	32.50	31.37	33.78	19.04	13.51	14.08	33.84	47.54	40.67	7.84	22.85	24.28	34.92	23.61	50.00
14	🟥	Almandine	1.79			2.29		0.98				2.81	1.53				1.42	1.42	1.58		
15	🟩	Apatite-F	1.79		1.35		7.50	19.60	17.56		1.35	4.22	1.53	4.91	3.38		1.42	1.42	4.76	19.44	
16	🟪	Barite	0.59					2.94	14.86						5.08						2.00
17	🟨	Goethite		4.00	4.05	2.29	1.25					1.40	1.53					2.85			
18	🟥	Hematite	27.76	50.00	43.24	4.59		0.98		47.61	45.94	15.49	13.84	16.39	3.38	60.78	41.42	12.85	7.93	2.77	
19	🟦	Hematite-Tin	2.38	26.00	5.40		1.25			14.28	9.45	2.81	1.53			21.56	2.85		1.58		
20	🟩	Ilmenite	0.89	2.00	1.35					1.58	4.05	5.63	1.53	1.63			1.42			1.38	
21	⬛	Monzonite					1.25	2.94													
22	🟥	Rutile	2.68			1.14	2.50	7.84	10.81	1.58	4.05		1.53	1.63	11.86	1.96		2.85	3.17	9.72	30.00
23	🟪	Titanite	1.19					0.98	9.45		1.35	1.40		1.63	1.69			1.42		4.16	12.00
24	🟦	Tourmaline																			
25	🟪	Zircon	0.29					3.92	4.05						6.77					2.77	
26	🟥	Unknown																	1.58	1.38	
Total:			100.00	100.00	100.00	100.00	100.00	100.00	100.00	100.00	100.00	100.00	100.00	100.00	100.00	100.00	100.00	100.00	100.00	100.00	100.00
Lithoclasts (wt. % of total analyzed grains)			~11.34	~1.71						~15.15						~11.43					

3.3 Results from XRD

Table 3.4 shows each mineral type identified with XRD technique. This technique was applied only on reference samples (that have not been sieved and separated by Frantz). The XRD spectrums are presented in Appendix D. Minerals identified with the XRD are albite, chlorite, hematite, muscovite, orthoclase, phlogopite, quartz and rutile. The XRD results shows, the sample contains rutile, and no other polymorphic mineral exists in the sample with same composition i.e. TiO_2. This analysis also confirms that the element containing iron and oxygen is hematite.

Table ***3.4****: Minerals identified by XRD technique in each reference sample.*

			Sample name	
#	**Color code**	**Mineral**	**CR-27-Refernce**	**CR-18-Reference**
1	🟨	Albite	×	×
2	⬛	Chlorite	×	
3	🟥	Hematite		×
4	⬜	Muscovite	×	
5	⬜	Orthoclase		×
6	🟫	Phlogopite	×	
7	🟦	Quartz		×
8	🟥	Rutile	×	

4 DISCUSSION AND IMPLICATION OF RESULTS

The FE-SEM and XRD results of reference samples are analyzed to know about the mineralogical composition of all three rock types. The outcomes obtained from FE-SEM for all sample fractions based on grain sizes and paramagnetic susceptibility have been combined, interpreted, and compared. Later on, the mineralogy of three reference sample fractions (not separated in Frantz) identified using FE-SEM-EDS, and XRD is discussed.

Secondly, for each sample, the relict of light minerals at different strength of magnetic fields for all grain sizes, i.e., un-sieved fraction (contains grains of all sizes), grains size < 250 µm, and grains size < 150 µm is enlightened.

Finally, the heavy mineral composition of amphibolite (CR-27), phyllite (CR-03), and felsic lava (CR-18) is also compared for all three different grain sizes to:

- Define the most fertile fraction for heavy mineral grains based on paramagnetic susceptibility.
- Determine the effectivity per lithology when using Frantz magnetic separator.

4.1 The mineralogical composition of samples

The mineralogical composition (in %) of reference samples (not gone through Frantz separation) of rocks is shown in Figure 4.1. The dominant mineralogy found in sample CR-27 is phlogopite, ilmenite, tin bearing hematite, Fe bearing anorthite, chlorite, and other heavy and non-heavy minerals. Quartz occurs in low concentrations. Since the CR-27 is an amphibolite rock, so a low amount of quartz was expected.

In contrast, the second sample, CR-03, which is phyllite (Grootderm Formation), contains quartz and hematite as the most abundant mineral type. In comparison, tin bearing hematite and other accessory minerals are in low concertation (Figure 4.1). Phyllite is a low-grade metamorphic rock. Therefore the interpreted mineralogy based on spectrums (in Appendix A) agrees with the rock type.

The Vredefontein Formation comprises volcanic rocks of acidic to intermediate composition in its upper parts (E. A. K. Middlemost, 1963). Albite, muscovite, phlogopite, and hematite constitute the dominant portion sample CR-18 with other minerals as minor components. The higher quartz, albite, and other feldspars content indicates the rock type as intermediate to felsic in composition.

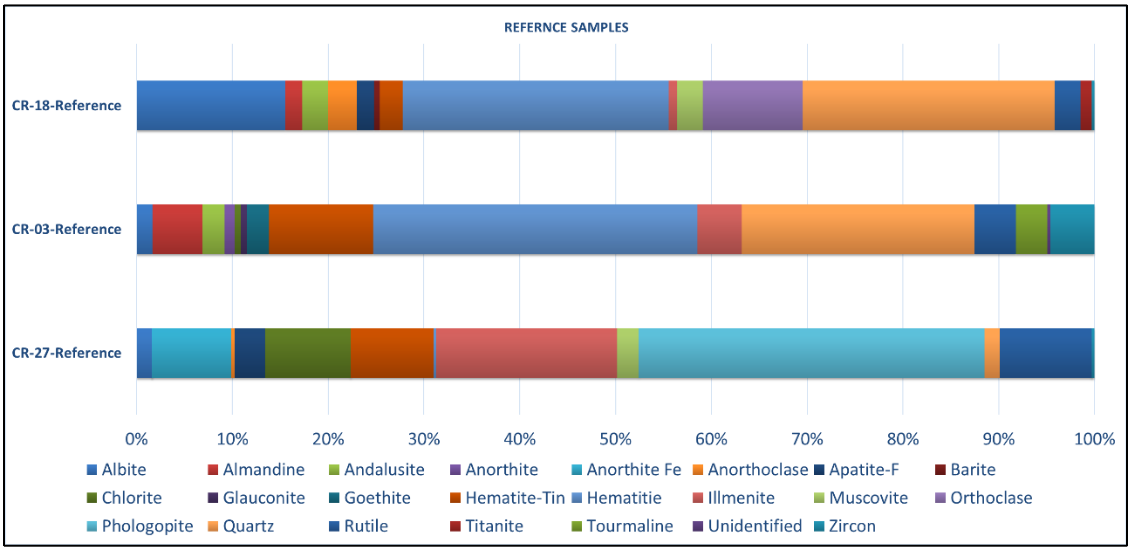

Figure 4.1: The graphs showing concertation of each mineral in reference samples.

The overall concentration of heavy minerals is low in all three samples when considering the whole mineralogy of the sample. This is because, during the magnetic separation of these samples (by Geotrack laboratory) in Australia, the apatite fraction, zircon concentrate, and zircon fraction were removed out at 25° forward slope and 2° side angle. The discussion of the magnetic separation results below is at 25° forward slope and 15° side angle.

4.2 Light minerals as a relict of magnetic separation

4.2.1 Rosh Pinah Formation (CR-27-amphibolite)

In Rosh Pinah Formation (CR-27-amphibolite) highest amount (>20%) for mineral albite is documented in the magnetic fraction at 0.4 A for un-sieved grains, and in FM, and 0.3 A for grains size < 250 µm (Figure 4.5). For grain size < 150 µm, it has abundance in magnetic retain at 0.1 A and nonmagnetic left over at 0.4 A. However, best extraction range for albite is >1.7 A (Rosenblum & Brownfield, 2000). Therefore, presence of albite as a dominant component in different fractions (at above mentioned magnetic field strengths) is due to its attachment with mineral hematite having high paramagnetic susceptibility (Figure 4.2 and 4.4).

In contrast, Fe bearing anorthite is abundant (>20%) at 0.2 and 0.3 A in un-sieved and grain size < 150 µm fraction (Figure 4.5). In grain size < 250 µm, Fe bearing anorthite is absent. Like albite, pure anorthite is also extractable at higher magnetic field strengths (>1.7 A). Despite this, the iron coating has increased anorthite's paramagnetic susceptibility, which led to its dominance at lower field strengths.

Quartz and chlorite occur in low amounts (<20%) and even <5% in some fractions. Magnetic retain at 0.2 A contains phlogopite in abundance (>20%) for all three different grain size fractions; however, in grain size < 250 µm, it also dominates in 0.1 A (Figure 4.5).

Based on the composition of quartz and mica like phlogopite, they need high magnetic field strength for extraction (Rosenblum & Brownfield, 2000). Presence of these minerals at lower magnetic field strength (Figure 4.5) is again because of their attachment to other minerals of high paramagnetic susceptibility, such as hematite (Figure 4.4). Chlorite comes with an exception among the light minerals; it has comparatively high paramagnetic susceptibility compare to quartz and other minerals. It has the best extraction range from 0.2 A to 0.5 A (Rosenblum & Brownfield, 2000). In sample CR-27, chlorite also makes lithoclast with hematite (see Figure 4.3), which could cause of its presence in certain fractions even in low quantities.

In general, all the sample fractions contain lithoclasts, but the un-sieved and < 250 µm fractions have shown more lithoclasts (>20%) than <150 µm (<20%) (Figure 4.5).

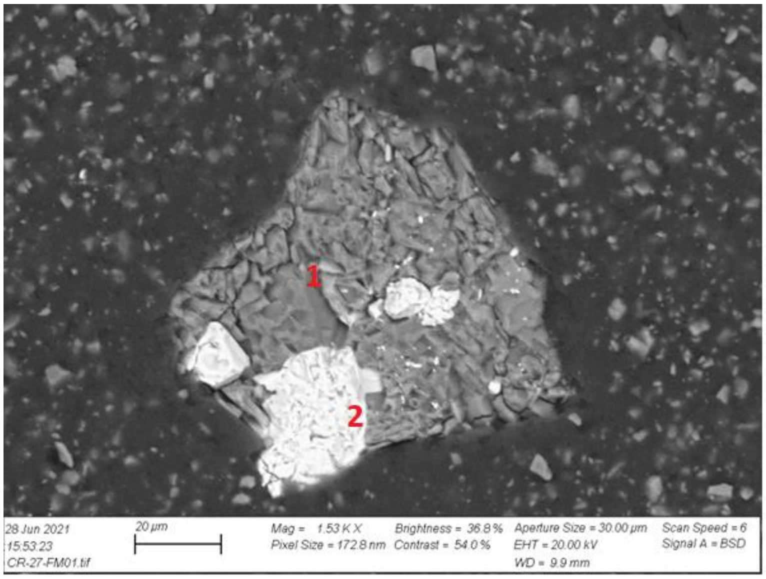

Figure 4.2: A lithoclast is made up of two minerals, albite (1) and hematite (2), in FM fraction (CR-27-Unisieved).

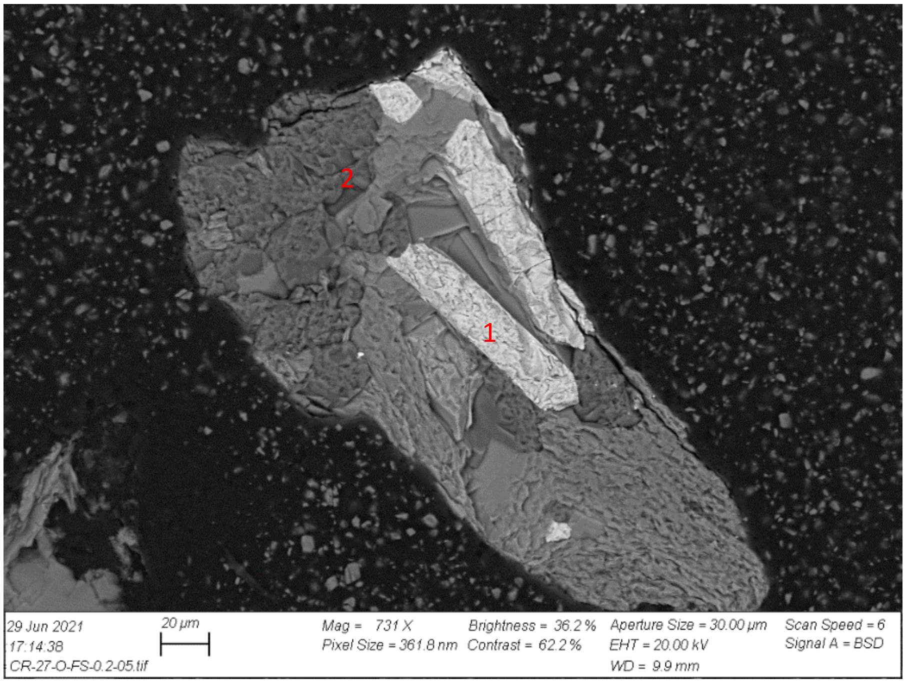

Figure 4.3: A lithoclast composed of hematite (1) and chlorite (1) in magnetic fraction at 0.2 A (CR-27-Unsieved).

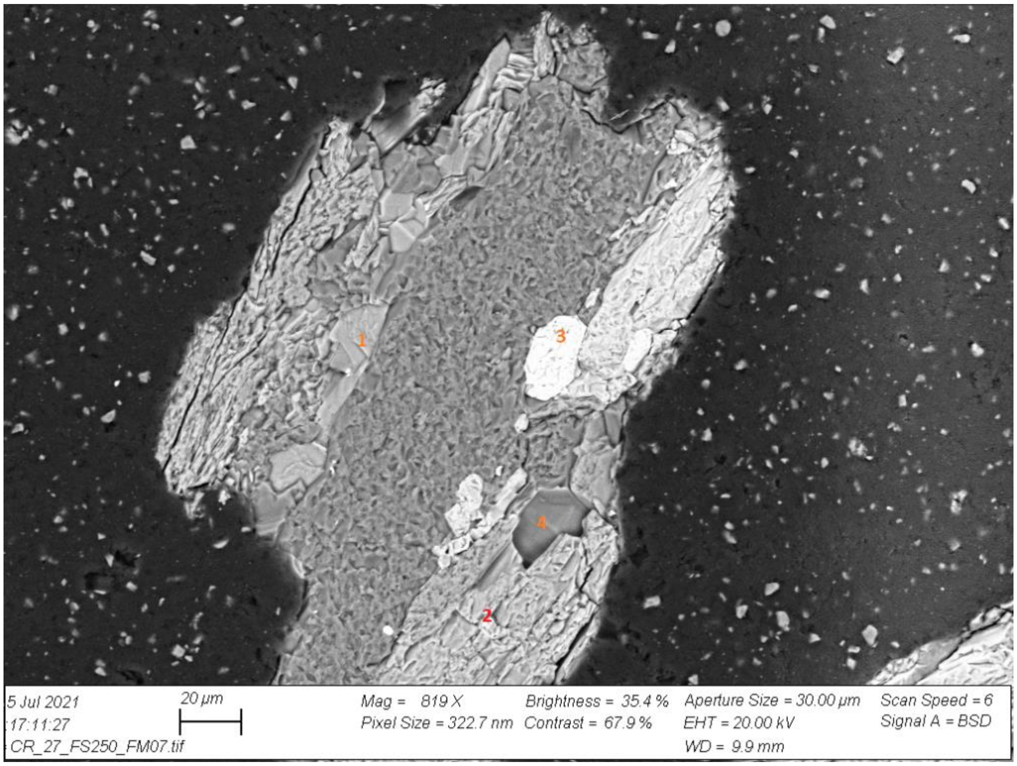

Figure 4.4:A lithoclast containing four minerals phlogopite (1), albite (2), hematite (3), and quartz (4) in FM fraction (CR-27<250 µm)

CR-27 (amphibolite)

			Un-sieved (Frantz separated)						Less than 250 µm (Frantz separated)						Less than 150 µm (Frantz separated)					
#	Color code	Mineral	FM	0.1 A	0.2 A	0.3 A	0.4 A	NM	FM	0.1 A	0.2 A	0.3 A	0.4 A	NM	FM	0.1 A	0.2 A	0.3 A	0.4 A	NM
1	🟨	Albite	▒	▒	▒	▒	█	▒	█	▒	▒	█	▒	▒	▒	█	▒	▒	▒	█
3	🟨	Andalusite						░												
5	🟧	Anorthite Fe	▒	▒	█	█			█	█	▒	▒	█	▒	░	░	█	█	░	
6	🟥	Anorthoclase	░	░	░	░	░													
7	⬛	Chlorite	▒	░	▒	▒	░	░	▒	▒	▒	▒	▒	▒	▒	▒	▒			
10	⬜	Muscovite				░									░		░		░	
11	⬜	Orthoclase													░					
12	🟫	Phlogopite	▒	░	█	░	░		▒	█	█	░	░	▒	░	░	█	▒	░	
13	🟦	Quartz	░	▒	▒	▒	▒	▒	▒		▒	▒	▒	▒	░	▒	▒	▒	▒	░
15	🟩	Apatite-F	░			░	▒	█							░	░			▒	█
18	🟥	Hematite	▒	░	░				░						░	░				
19	🟦	Hematite-Tin	▒	█	▒				▒	▒	▒	▒	░		█	█	░			
20	🟩	Ilmenite	░	▒	░	░	░		░	░	▒		░		▒	▒	░	░	░	
22	🟥	Rutile	▒	▒	▒	█	█	█	▒	▒	▒	█	█	█	▒	▒	▒	█	█	█
25	🟪	Zircon	░		░		░			░										
26	🟥	Unknown										░	░	░						
Total:		100.00	100.00	100.00	100.00	100.00	100.00	100.00	100.00	100.00	100.00	100.00	100.00	100.00	100.00	100.00	100.00	100.00	100.00	100.00
Amount of lithoclasts:			█						█						▒					

	Not found
░	Very few (<5%)
▒	Major component (5-20%)
█	Dominant component (>20%)

NM: Nonmagnetic at 0.4 A

FM: Ferromagnetic

Figure 4.5: The % of each mineral in different magnetic fractions of sample CR-27. The values are % of total minerals identified using EDS.

4.2.2 Grootderm Formation (CR-03 -Phyllite)

In Grootderm Formation (CR-03 -Phyllite), some light minerals have also remained in the least expected fractions. These minerals are anorthite, glauconite, orthoclase, and quartz. Albite shows the highest amount in an un-sieved fraction, where it dominates (>20%) at 0.4 A, whereas in grain size < 250 µm, it shows the maximum amount (>20%) in FM an 0.1 A fraction. In a grain size <150 µm, it occurs in less amount (Figure 4.8).

Anorthite and glauconite show presence as dominant components (>20%) in FM and at 0.2 A in grain size <250 µm. Quartz also shows wide distribution as an abundant component (>20%) in all the grain sizes (i.e., un-sieved fraction, grains size < 250 µm, and grain size < 150 µm) at different magnetic field strengths (Figure 4.8)

The sample CR-03 also contains lithoclasts (Figure 4.8). The amount of lithocalsts is high (>20%) for grain size < 250 µm compared to the other two grain sizes (un-sieved and <150 µm). The presence of these minerals here is either the result of the impurities or their association with other paramagnetic minerals in the form of lithoclast (Figure 4.6 and Figure4.7), leading to their abundance at low magnetic field strength.

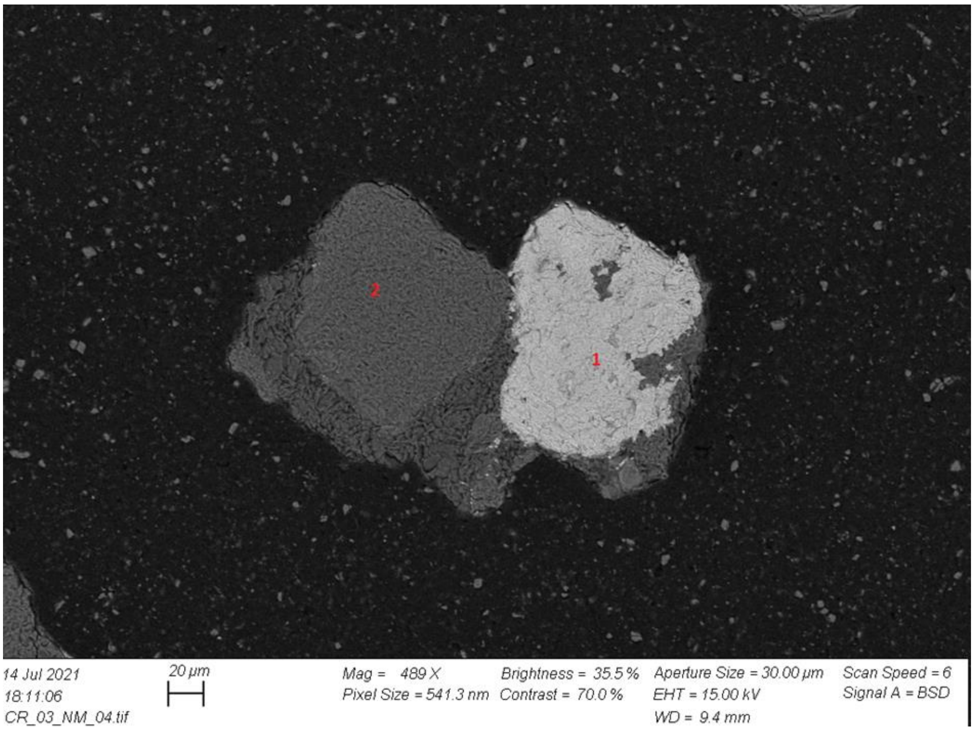

4.6: A lithoclast composed of hematite (1) and quartz (2) in nonmagnetic fraction at 0.4 A (CR-03 < 250 µm)

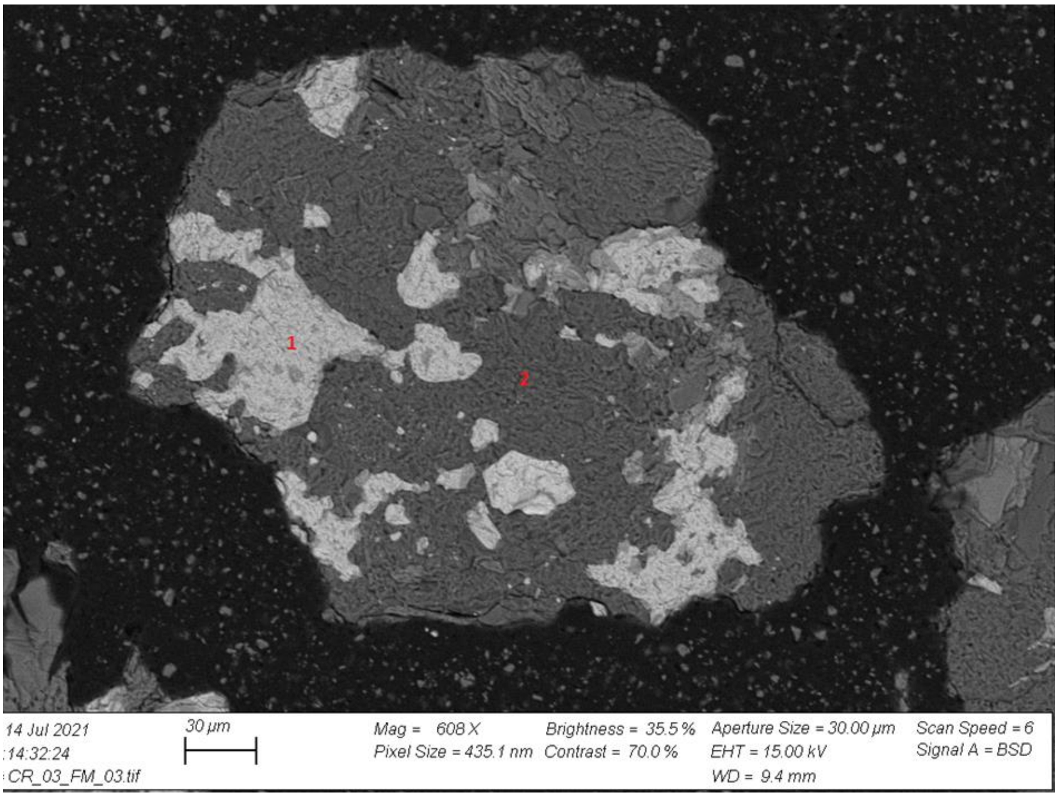

4.7: A lithoclast is composed of hematite (1) and albite (2) in ferromagnetic fraction (CR-03 < 250 µm).

CR-03 (phyllite)

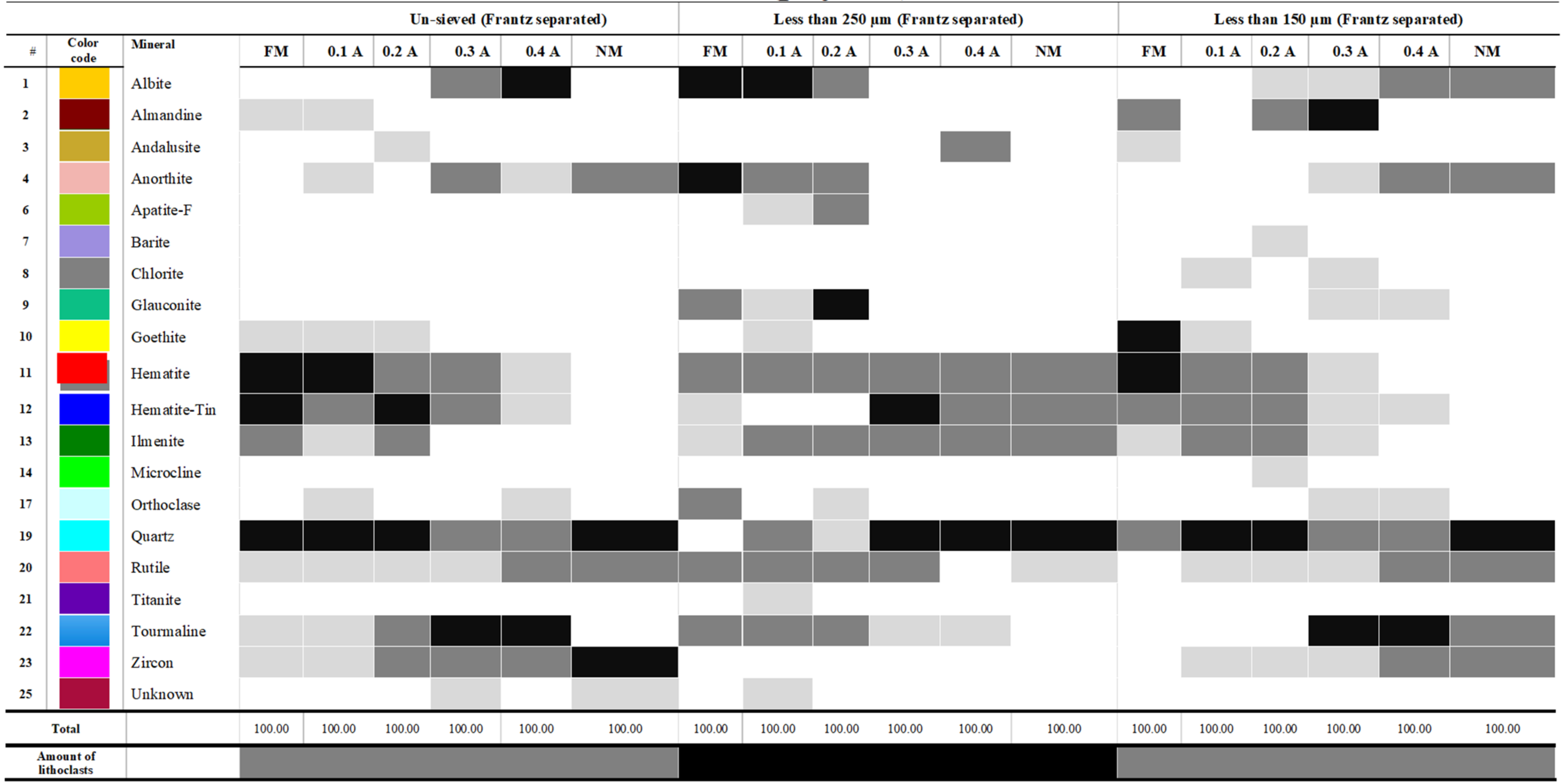

#	Color code	Mineral	Un-sieved (Frantz separated)						Less than 250 µm (Frantz separated)						Less than 150 µm (Frantz separated)					
			FM	0.1 A	0.2 A	0.3 A	0.4 A	NM	FM	0.1 A	0.2 A	0.3 A	0.4 A	NM	FM	0.1 A	0.2 A	0.3 A	0.4 A	NM
1	■	Albite				▒	█		█	█	▒						░	░	▒	▒
2	■	Almandine	░	░											▒		▒	█		
3	■	Andalusite			░								▒		░					
4	■	Anorthite		░		▒	░	▒	█	▒	▒							░	▒	▒
6	■	Apatite-F								░	▒									
7	■	Barite															░			
8	■	Chlorite														░		░		
9	■	Glauconite							▒	░	█							░	░	
10	■	Goethite	░	░	░					░					█	░				
11	■	Hematite	█	█	▒	▒	░		▒	▒	▒	▒	▒	▒	█	▒	▒	░		
12	■	Hematite-Tin	█	▒	█	▒	░		░			█	▒	▒	▒	▒	▒	░	░	
13	■	Ilmenite	▒	░	▒				░	▒	▒	▒	▒	▒	░	▒	▒	░		
14	■	Microcline															░			
17	■	Orthoclase		░			░		▒		░							░	░	
19	■	Quartz	█	█	█	▒	▒	█		▒	░	█	█	█	▒	█	█	▒	▒	█
20	■	Rutile	░	░	░	░	▒	▒	▒	▒	▒	▒		░		░	░	░	▒	▒
21	■	Titanite								░										
22	■	Tourmaline	░	░	▒	█	█		▒	▒	▒	░	░					█	█	▒
23	■	Zircon	░	░	▒	▒	▒	█								░	░	░	▒	▒
25	■	Unknown				░		░		░										
Total			100.00	100.00	100.00	100.00	100.00	100.00	100.00	100.00	100.00	100.00	100.00	100.00	100.00	100.00	100.00	100.00	100.00	100.00
Amount of lithoclasts			▒						█						▒					

□ Not found
░ Very few (<5%)
▒ Major component (5-20%)
█ Dominant component (>20%)

NM: Nonmagnetic at 0.4 A
FM: Ferromagnetic

Figure 4.8: The % of each mineral in different magnetic fractions of sample CR-03. The values are % of total minerals identified using EDS.

4.2.3 Vredefontein Formation (CR-18-Lavas)

Retain of light minerals is also found in Vredefontein Formation (CR-18-Lavas). For example, albite is dominant in magnetic retain at 0.2 A and 0.3 A for un-sieved and <250 µm grains size, whereas in <150 µm, it only shows high concertation in magnetic retain at 0.2 A (Figure 4.10). Other than this, anorthite, anorthoclase, microcline, muscovite, and orthoclase occur in low quantity, occasionally having concertation >5% in some fractions (Figure 4.10).

Quartz shows abundance in all three grain sizes (un-sieved fraction, grain size <250 µm and grain size<150 µm) at different magnetic field strengths (Figure 4.10). Same is the case for other light minerals such as anorthite, anorthoclase, microcline, muscovite, and orthoclase. Considerable amount (<20%) these minerals is retained in some magnetic fractions (Figure 4.10).

Like previous two lithologies (amphibolite and phyllite), the sample CR-18 also contains lithoclast or locked grains (Figure 4.10). The amount of lithoclasts is low (<5%) in un-sieved fraction and is considerably high (<20%) for the other two grain sizes (grain size <250 µm and grain size<150 µm).

The survival of these light minerals can be attributed to either impurities which increase their specific density or their welding with other paramagnetic minerals that increases their abundance at lower magnetic field strengths (Figure 4.9).

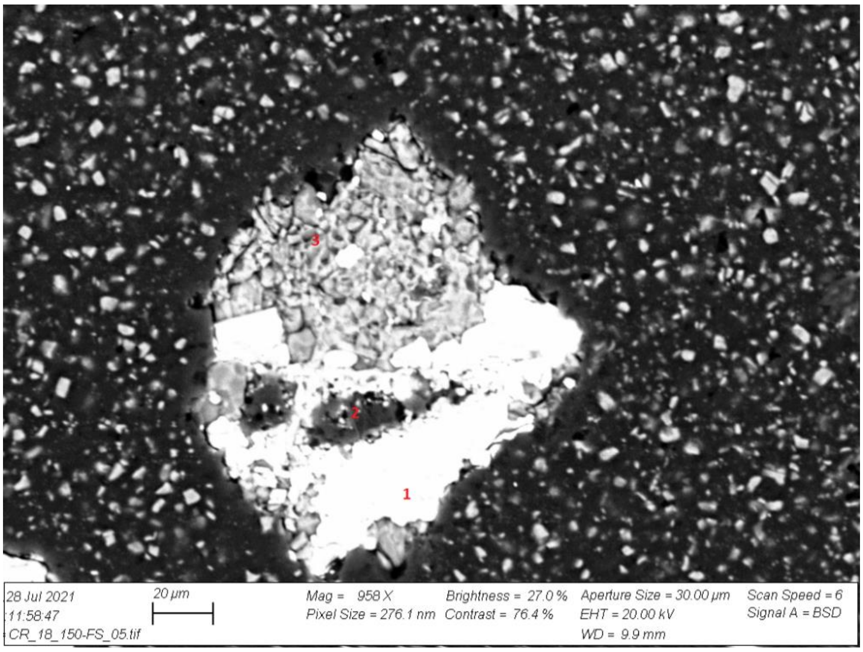

Figure 4.9: The lithoclast is composed of hematite (1), rutile (2), and quartz (3) in ferromagnetic fraction (CR-18 < 150 µm).

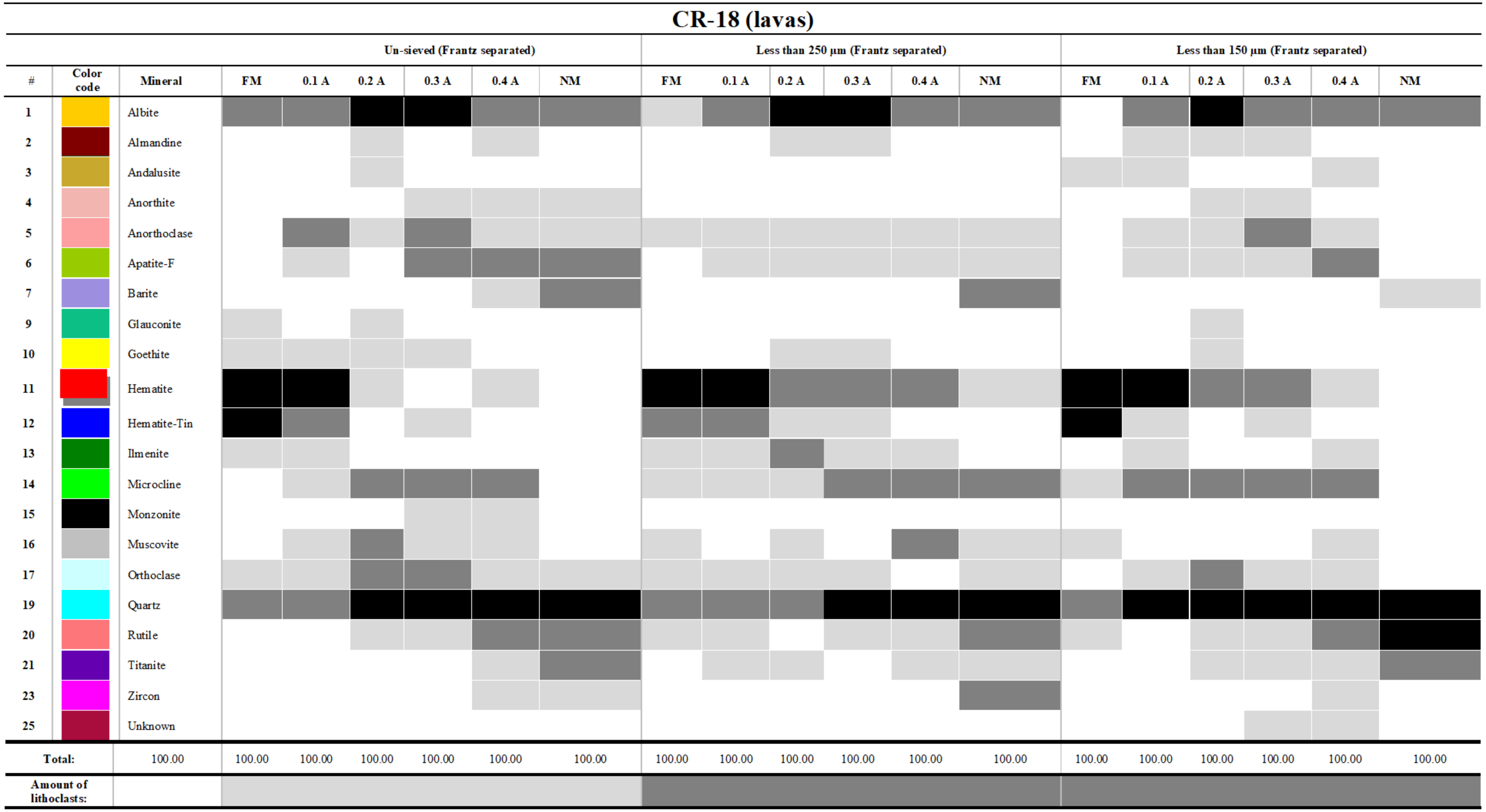

CR-18 (lavas)

			Un-sieved (Frantz separated)						Less than 250 µm (Frantz separated)						Less than 150 µm (Frantz separated)					
#	**Color code**	**Mineral**	**FM**	**0.1 A**	**0.2 A**	**0.3 A**	**0.4 A**	**NM**	**FM**	**0.1 A**	**0.2 A**	**0.3 A**	**0.4 A**	**NM**	**FM**	**0.1 A**	**0.2 A**	**0.3 A**	**0.4 A**	**NM**
1	🟧	Albite	▓	▓	█	█	▓	▓	░	▓	█	█	▓	▓		▓	█	▓	▓	▓
2	🟫	Almandine			░		░				░	░				░	░	░		
3	🟫	Andalusite			░										░	░			░	
4	🟥	Anorthite				░	░	░									░	░		
5	🟥	Anorthoclase		▓	░	▓	░	░	░	░	░	░	░	░		░	░	▓	░	
6	🟩	Apatite-F		░		▓	▓	▓		░	░	░	░	░		░	░	░	▓	
7	🟪	Barite					░	▓						▓						░
9	🟩	Glauconite	░		░												░			
10	🟨	Goethite	░	░	░	░					░	░					░			
11	🟥	Hematite	█	█	░		░		█	█	▓	▓	▓	░	█	█	▓	▓	░	
12	🟦	Hematite-Tin	█	▓		░			▓	▓	░	░			█	░		░		
13	🟩	Ilmenite	░	░					░	░	▓	░	░			░			░	
14	🟩	Microcline		░	▓	▓	▓		░	░	░	▓	▓	▓	░	▓	▓	▓	▓	
15	⬛	Monzonite				░	░													
16	⬜	Muscovite		░	▓	░	░		░		░		▓	░	░				░	
17	⬜	Orthoclase	░	░	▓	▓	░	░	░	░	░	░		░		░	▓	░	░	
19	🟦	Quartz	▓	▓	█	█	█	█	▓	▓	▓	█	█	█	▓	█	█	█	█	█
20	🟥	Rutile			░	░	▓	▓	░	░		░	░	▓	░		░	░	▓	█
21	🟪	Titanite					░	▓		░	░		░	░			░	░	░	▓
23	🟪	Zircon					░	░						▓					░	
25	🟥	Unknown																░	░	
Total:		100.00	100.00	100.00	100.00	100.00	100.00	100.00	100.00	100.00	100.00	100.00	100.00	100.00	100.00	100.00	100.00	100.00	100.00	100.00
Amount of lithoclasts:			░						▓						▓					

⬜	Not found
░	Very few (<5%)
▓	Major component (5-20%)
█	Dominant component (>20%)

NM: Nonmagnetic at 0.4 A
FM: Ferromagnetic

Figure 4.10: The % of each mineral in different magnetic fractions of sample CR-03. The values are % of total minerals identified using EDS.

4.3 Comparison of different lithologies concerning heavy mineral compositions at different grain sizes

Comparison of three different lithologies Amphibolite (CR-7), felsic lava (CR-18), and phyllite (CR-03), with only heavy mineral concentration, are presented in graphs as shown in Figure 4.11, Figure 4.12, and Figure 4.13 for un-sieved, grain size fraction <150 µm and grain size fraction <250 µm fraction respectively. The values are in % and represent the only % of HM in the sample. The tabular graphs are produced using data shown in Appendix B.

Beginning from almandine, (Figure 4.11, Figure 4.12, and Figure 4.13) it is noticeable that amphibolite (CR-27) is entirely missing almandine in its composition at all magnetic fractions in all grain size fractions (i.e. un-sieved sample fraction, grain size fraction <150 µm and grain size fraction <250 µm fraction). For other two rock units (phyllite and lava), almandine does not show abundance in any magnetic fraction at any grain size fraction; however, for lavas (CR-18), magnetic retain at 0.2 A in un-sieved grains, and for phyllite (CR-03), magnetic retain at 0.2 A and 0.3 A in grain size fraction <150 µm contains a significant amount of almandine (<30%) (Figure 4.11, Figure 4.12, and Figure 4.13).

Table 4.1: The best extraction range for heavy minerals at 25° forward slope and 15° side slope (Rosenblum & Brownfield, 2000).

Mineral	**Best extraction range**
Almandine	0.2 A to 0.4 A
Apatite	>1.7 A
Barite	>1.7 A
Goethite	0.2A to 0.4 A
Hematite	0.1 to 0.3 A
Ilmenite	02 A to 0.3 A
Monzonite	0.5 A to 0.8 A
Rutile	>1.7 A
Titanite	0.8 A to >1.7 A
Zircon	>1.7 A

As the rock sample CR-18 does not contain the almandine in abundant amount but the presence of the almandine in igneous is not rare. They are mostly found in three parageneses: In granitic aplites and pegmatite as later stage minerals, they can also found as xenocrysts due to contamination by pelitic material and in some rocks such as calc-alkali granites and rhyolites they are found as primary equilibrium phases (Deer, Howie, & Zussman, 2013).

Like igneous rock almandine is also commonly found in metamorphic rocks as in phyllite (CR-03). Almandine can be used as zonal minerals, in areas where a progressive metamorphism of rocks take place. This almandine forms at the top of biotite zone as a result of reaction with chlorite. The breakdown of the mica in high grade metamorphic rocks also produces almandine (Deer et al., 2013).

Hematite is abundant mineral (Figure 4.11, Figure 4.12, and Figure 4.13) in two rock units i.e. phyllite (CR-03) and lavas (CR-18). In lava, for hematite the most fertile fraction is FM, 0.1 A and 0.2 A for un-sieved grains, and FM,0.1 A, 0.2 A, 0.3 A and 0.4 A for grain size fraction <250 µm. In grain size <150 µm the hematite is dominant in FM,0.1 A, 0.2 A, and 0.3 A.

The phyllite contains abundant hematite in FM and 0.1 A for un-sieved grains, in FM, 0.2 A and in NM fraction for grain size fraction <250 µm. For grain size <250 µm it is abundant in FM and magnetic retained at 0.2 A (Figure 4.11, Figure 4.12, and Figure 4.13).

In contrast, amphibolite has overall low amount (<30%) of hematite in all three grain sizes (i.e. un-sieved, <250 µm and <150 µm) (Figure 4.11, Figure 4.12, and Figure 4.13).

Hematite in large amount is not so common in igneous rocks. However if the magma is deficient in ferrous (such as in granites, syenites, rhyolites etc.) and there is a late-stage volcanic activity particularly with ilmenite whose thin crystals are sublimed on already present material, then Formation of hematite can take place. It can also form as results of pseudo-morphous replacement of olivine in basalts (Deer et al., 2013). The lava of sample CR-18 is dominantly of felsic to intermediate composition (E. Middlemost, 1966) therefore high occurrence of hematite maybe due to late stage volcanic activity with already present iron rich material.

The rock Grootderm Formation (CR-03) contains both mafic and metamorphic rocks (Hartwig E. Frimmel et al., 1996). In metamorphic rocks, usually the quartz-hematite ore is found in gneiss and meta cherts which formed as result of volcanic activity. The presence of hematite in phyllite could be result of volcanic activity.

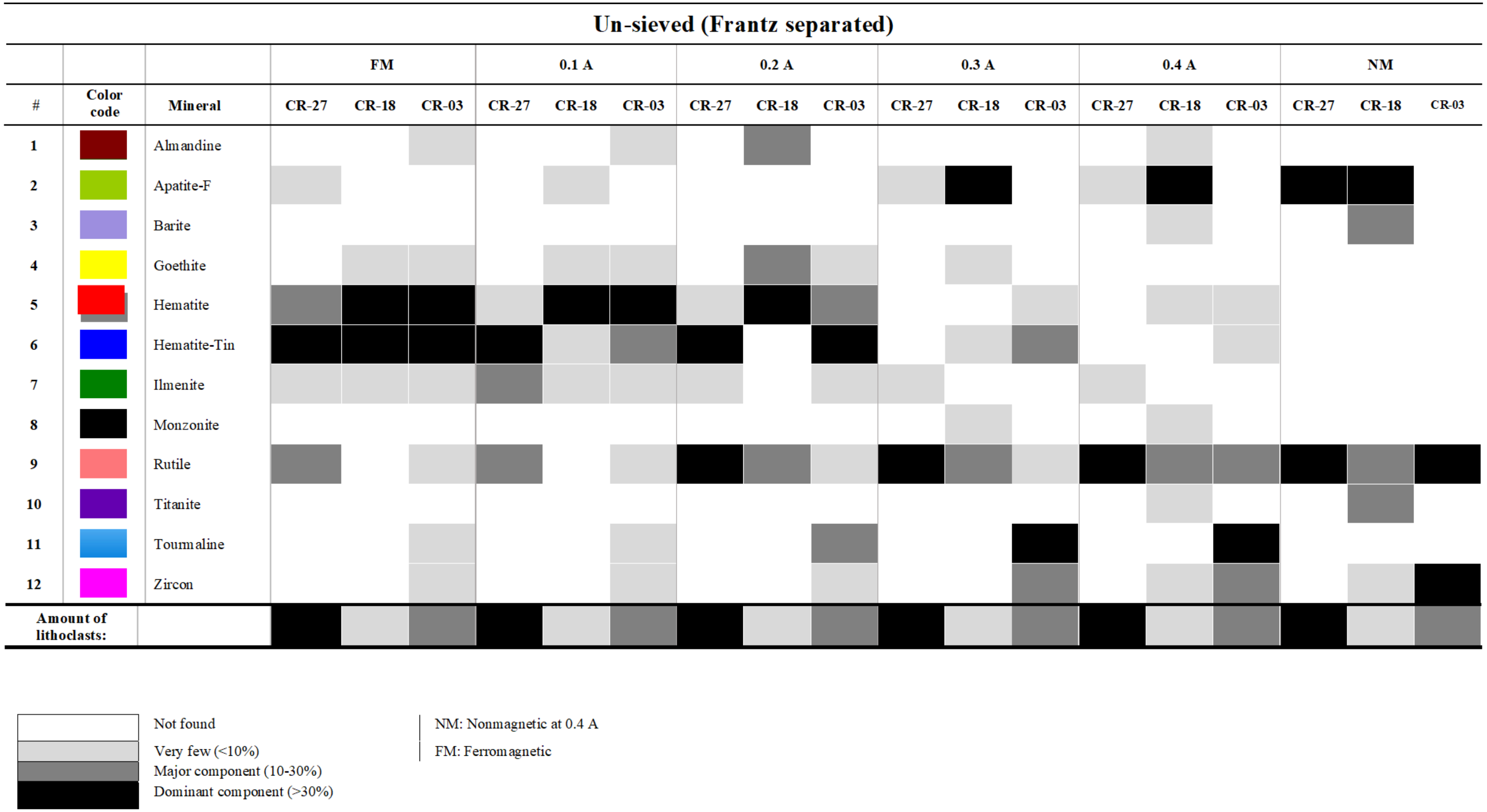

Un-sieved (Frantz separated)

			FM			0.1 A			0.2 A			0.3 A			0.4 A			NM		
#	Color code	Mineral	CR-27	CR-18	CR-03	CR-27	CR-18	CR-03	CR-27	CR-18	CR-03	CR-27	CR-18	CR-03	CR-27	CR-18	CR-03	CR-27	CR-18	CR-03
1	🟫	Almandine			░			░		▒						░				
2	🟩	Apatite-F	░				░					░	■		░	■		■	■	
3	🟪	Barite														░			▒	
4	🟨	Goethite		░	░		░	░		▒	░		░							
5	🟥	Hematite	▒	■	■	░	■	■	░	■	▒			░		░	░			
6	🟦	Hematite-Tin	■	■	■	■	░	▒	■		■		░	▒			░			
7	🟩	Ilmenite	░	░	░	▒	░	░	░		░	░			░					
8	⬛	Monzonite											░			░				
9	🟥	Rutile	▒		░	▒		░	■	▒	░	■	▒	░	■	▒	▒	■	▒	■
10	🟪	Titanite														░			▒	
11	🟦	Tourmaline			░			░			▒			■			■			
12	🟪	Zircon			░			░			░			▒		░	▒		░	■
Amount of lithoclasts:			■	░	▒	■	░	▒	■	░	▒	■	░	▒	■	░	▒	■	░	▒

□ Not found
░ Very few (<10%)
▒ Major component (10-30%)
■ Dominant component (>30%)

NM: Nonmagnetic at 0.4 A
FM: Ferromagnetic

Figure 4.11: The % of each mineral in all three samples at different magnetic field strength for un-sieved sample fraction. The values are % of total heavy minerals identified using EDS.

Rutile is found in all three rock units. In Amphibolite (CR-27), the abundance is recognized in magnetic retain at 0.2A, 0.3 A, 0.4 A and also in NM retain for un-sieved grains whereas grain size fraction <250 µm gives abundance of rutile in FM, 0.1 A, 0.2 A, 0.3 A and 0.4 A. For grain size fraction <150 µm amphibolite contains rutile in abundance at all magnetic retains except at 0.2 A (Figure 4.11, Figure 4.12, and Figure 4.13).

Rutile in phyllite (CR-03), is abundant only in NM fraction for un-sieved grains and for grain size fraction <150 µm. However, in for grain size fraction <250 µm it dominates (>30%) in FM fraction. In lava (CR-18), the abundance of rutile is restricted only to NM fraction for all three grain sizes (Figure 4.11, Figure 4.12, and Figure 4.13).

Rutile is the high temperature minerals, which tend to occur in high temperature pressure conditions. It is found in igneous rocks mainly in plutonic rocks but can occur in volcanic rocks as a minute grain. In metamorphic rock, it exists as an accessory mineral particularly in some amphibolite and eclogites (Deer et al., 2013). In general, among all three rock units, highest amount of rutile is present in amphibolite (CR-27) where it is retained in many magnetics fractions (Figure 4.11, Figure 4.12, and Figure 4.13). This represents the high temperature and pressure conditions facilitating the formation of amphibolite (Rosh Pinah Formation).

Tin bearing hematite is abundant mineral in all three rock units (phyllite, amphibolite and lava) at different magnetic field strengths (Figure 4.11, Figure 4.12, and Figure 4.13). For amphibolite FM,0.1 A and 0.2 A are tin bearing hematite rich magnetic fractions for un-sieved grains size whereas in grain size fraction <250 µm it is dominant in FM,0.1 A, 0.2 A and 0.3 A. The grain size fraction <150 µm contains abundant tin bearing hematite in FM and 0.1 A.

In phyllite (CR-03), tin bearing hematite is abundant in FM and magnetic retain at 0.2 A for un-sieved grain fraction (Figure 4.11, Figure 4.12, and Figure 4.13), whereas in grain size fraction <150 µm it is abundant in magnetic retain at 0.3 A and 0.4 A. In contrast, for grain size fraction <150 µm, the tin bearing hematite is only abundant in magnetic retain at 0.2 A.

Lavas (CR-18) has abundance of tin bearing hematite only in one grain size i.e. un-sieved fraction in FM retain. In other grain sizes, it is either absent or in low concentration (<30).

In comparison with phyllite (CR-03) and lava (CR-18), the tin bearing hematite is more dominant in amphibolite (CR-27) (Figure 4.11, Figure 4.12, and Figure 4.13). The sample CR-27 also contains rutile in dominant concertation as discussed above. It is possible chemical weathering and fluid reactions may result in addition of tin in hematite.

The ilmenite is present in all three rock units however it does not dominant in any grain size except for phyllite (CR-03) which contains abundant (>30%) ilmenite in magnetic retain at 0.1 A for grain size fraction <150 µm (Figure 4.9, Figure 4.10, and Figure 4.11).

It is quite common accessory mineral found in igneous and metamorphic rocks. In metamorphic rocks it forms as result of regional metamorphism (Deer et al., 2013). Sample CR-03, is a low-grade metamorphic rock formed as result of regional metamorphism.

Phyllite (CR-03) and Lavas (CR-18) contains goethite, however the abundant amount of goethite is solitary found for phyllite (CR-03) in FM retain for grain size fraction <150 µm (Figure 4.11, Figure 4.12, and Figure 4.13).

The weathering of iron bearing minerals such as siderite, magnetite, and pyrite forms goethite (Deer et al., 2013). Overall, the phyllite contains more goethite than lavas, and in amphibolite it is absent (Figure 4.10, Figure 4.11, and Figure 4.12). The presence of large amount of goethite in phyllite (CR-03) suggest that, it has gone through more chemical weathering then lavas (CR-18).

Apatite-F is dominant (>30%) in CR-27 (Amphibolite) and CR-18 (Lavas) in only two grain size fractions i.e. un-sieved fraction and grain size fraction <150 µm. In amphibolite (CR-27), it is dominant in NM fraction for both un-sieved fraction and grain size fraction <150 µm (Figure 4.11, Figure 4.12, and Figure 4.13).

For lavas, in un-sieved grain fraction it is dominant in magnetic retain at 0.3 A, 0.4 A and in NM retain. For grain size fraction <150 µm it is abundant at in magnetic retain at 0.4 A only (Figure 4.11, Figure 4.12, and Figure 4.13).

Apatite in sample CR-27 and CR-18 is not as abundant as other heavy minerals such as hematite and rutile because, the separation carried out by Geotrack international, Australia removed the apatite fractions. However, in comparison between rock samples, the lavas (CR-18) contains more apatite than amphibolite which indicates separation for lavas in Australia was less effective compare to amphibolite (Figure 4.11, Figure 4.12, and Figure 4.13).

Apatite most abundant phosphorus minerals and found in all types igneous rock from basic to acidic. Among different varieties of apatite, fluorapatite is most common in igneous rocks. In regionally metamorphosed rocks fluorapatite is commonly associated with phlogopite (Deer et al., 2013). Since apatite, is found in almost all igneous rock, therefore it does not indicate specific pressure and temperature condition.

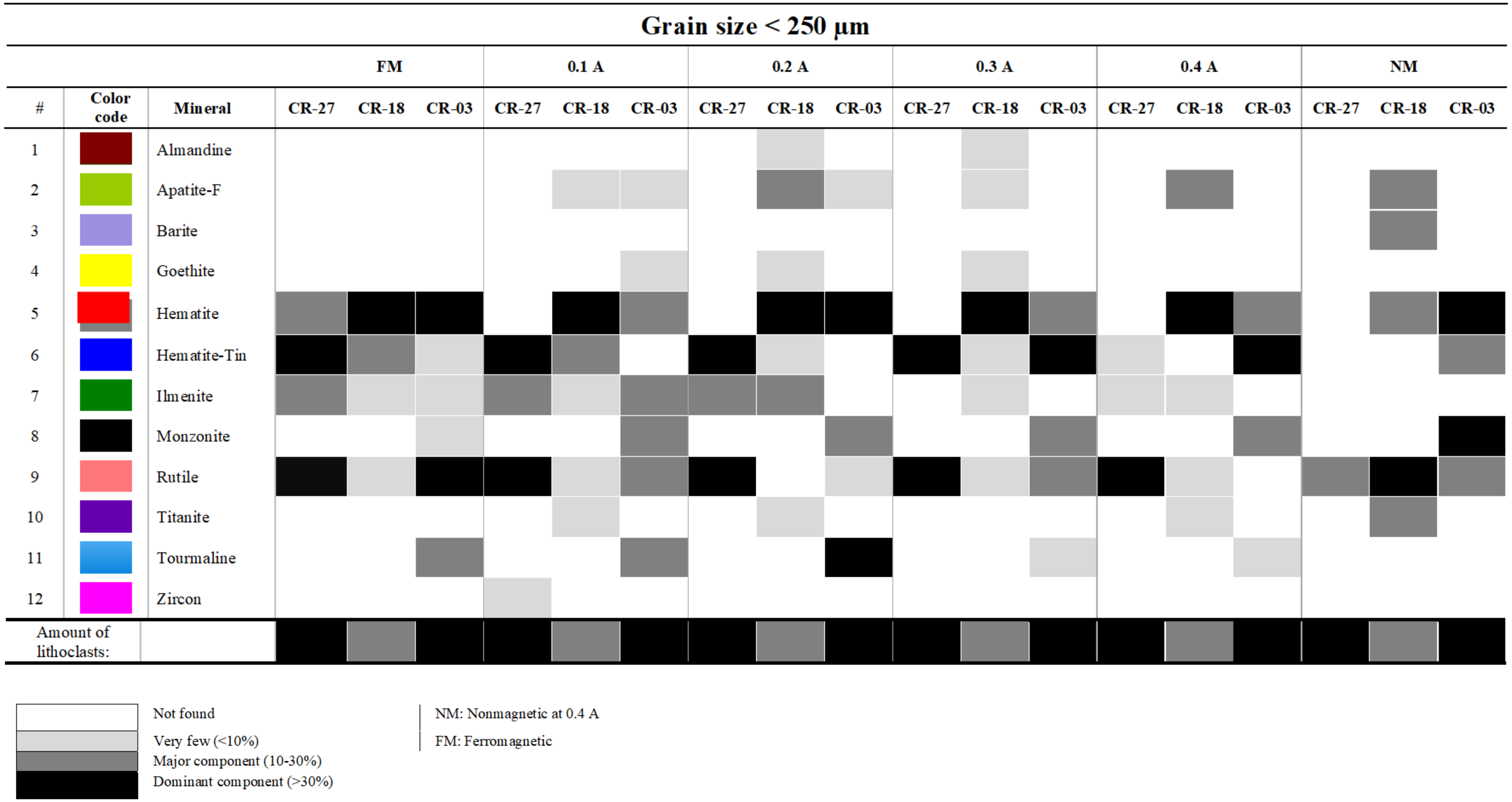

Grain size < 250 µm																				
			FM			**0.1 A**			**0.2 A**			**0.3 A**			**0.4 A**			**NM**		
#	**Color code**	**Mineral**	**CR-27**	**CR-18**	**CR-03**	**CR-27**	**CR-18**	**CR-03**	**CR-27**	**CR-18**	**CR-03**	**CR-27**	**CR-18**	**CR-03**	**CR-27**	**CR-18**	**CR-03**	**CR-27**	**CR-18**	**CR-03**
1	🟫	Almandine								░			░							
2	🟩	Apatite-F					░	░		▓	░		░			▓			▓	
3	🟪	Barite																	▓	
4	🟨	Goethite						░		░			░							
5	🟥	Hematite	▓	█	█		█	▓		█	█		█	▓		█	▓		▓	█
6	🟦	Hematite-Tin	█	▓	░	█	▓		█	░		█	░	█	░		█			▓
7	🟩	Ilmenite	▓	░	░	▓	░	▓	▓	▓			░		░	░				
8	⬛	Monzonite			░			▓			▓			▓			▓			█
9	🟥	Rutile	█	░	█	█	░	▓	█		░	█	░	▓	█	░		▓	█	▓
10	🟪	Titanite					░			░						░			▓	
11	🟦	Tourmaline			▓			▓			█			░			░			
12	🟪	Zircon				░														
Amount of lithoclasts:			█	▓	█	█	▓	█	█	▓	█	█	▓	█	█	▓	█	█	▓	█

☐ Not found
░ Very few (<10%)
▓ Major component (10-30%)
█ Dominant component (>30%)

NM: Nonmagnetic at 0.4 A
FM: Ferromagnetic

Figure 4.12: The % of each mineral in all three samples at different magnetic field strength for grain size fraction <250 µm. The values are % of total heavy minerals identified using EDS.

Zircon in dominance is only found in phyllite (CR-03) in NM retain for un-sieved grain and grain size fraction <150 µm. In other two lithological units it is not dominant (Figure 4.11, Figure 4.12, and Figure 4.13). Like apatite, the existence of zircon is unexpected, however zircon grains locked with other minerals can hang at low magnetic field strength.

Tourmaline is found only in one sample i.e. CR-03, in all three grain sizes (un-sieved, grain size fraction <250 µm, grain size fraction <150 µm). It is dominant in magnetic retain at 0.3A and 0.4 A for un-sieved fraction and grain size fraction <150 µm whereas in grain size fraction <250 µm, highest amount is recorded in magnetics retain at 0.2 A (Figure 4.11, Figure 4.12, and Figure 4.13).

The tourmaline is commonly found in felsic rocks such as granites and pegmatites. It is also found in metamorphic rock as result of boron metasomatism or due to recrystallization of detrital grains from parent sediments (Deer et al., 2013). The high concentration of tourmaline and also goethite in CR-03 indicates the chemical weathering by reaction of fluids.

Like tourmaline, monzonite is also restricted to phyllite (CR-03). the highest amount of Monzonite is recorded in NM retain for grain size fraction <250 µm (Figure 4.11, Figure 4.12, and Figure 4.13). Monzonite is absent in grain size fraction <150 µm whereas in un-sieved grain it has very few grains (<5%).

It is an accessory mineral commonly found in felsic igneous rocks, such as granites. Among metamorphic rocks. Monzonite is generally found in most grades of metapelite rocks.

The titanite is only found in Lava (CR-18), however It is not found as dominant component in any magnetics fraction. The NM fraction for grain size fraction <150 µm contains titanite which is less than 30% (Figure 4.11, Figure 4.12, and Figure 4.13).

Titanate also known as sphene is common accessory mineral in igneous rock particularly it is dominant titanium-bearing mineral in rocks of intermediates to acidic composition. It can also find in low-temperature Alpine-type veins where it occurs in association with albite and epidote (Deer et al., 2013).

The barite is also restricted to lavas (CR-18), it is found NM fraction of all three grain sizes (un-sieved, grain size fraction <250 µm and grain size fraction <150 µm) but the overall concentration is less than 30% (Figure 4.11, Figure 4.12, and Figure 4.13). The presence of barite at low magnetic field strength is due to high amount of clasts because it is non magnetics mineral and is usually extracted at >1.7 A (Rosenblum & Brownfield, 2000).

Barite is generally a product of hydrothermal activity which can precipitate from intermediate temperature fluid (150–250 C°), seafloor plumes, fractures zones and in volcanic arcs (Hein, Zierenberg, Maynard, & Hannington, 2007). It can also formed in mica an feldspar found in igneous rocks due to mixing of sulphur rich fluids (Deer et al., 2013).

Some of the minerals such as almandine, hematite, tin bearing hematite, tourmalines, ilmenite and goethite are extracted in expected range presented in Table 4.1 with few exceptions where these minerals are dominated in other fractions where they are not supposed to be. One example to illustrate is goethite, which is generally expected to separate at 0.2 A to 0.4 A according to (Rosenblum & Brownfield, 2000) but it is found in FM retain of sample CR-03 for grain size fraction <150 µm where usually highly paramagnetic mineral is expected. This could be due to either presence of impurities or due to presence of these minerals in the form of lithoclast.

Another, example is Rutile, which occurs dominant in all three grain sizes but it is expected normally to extract at >1.7 A which is its best extraction range (Rosenblum & Brownfield, 2000) however it could exist in fractions of low magnetic field strength due to presence of impurities or if it is locked with other grain of high paramagnetic susceptibility such as hematite (Figure 4.14). The abundance of rutile does not seem to be controlled by grains size, or lithology (Figure 4.11, Figure 4.12, and Figure 4.13).

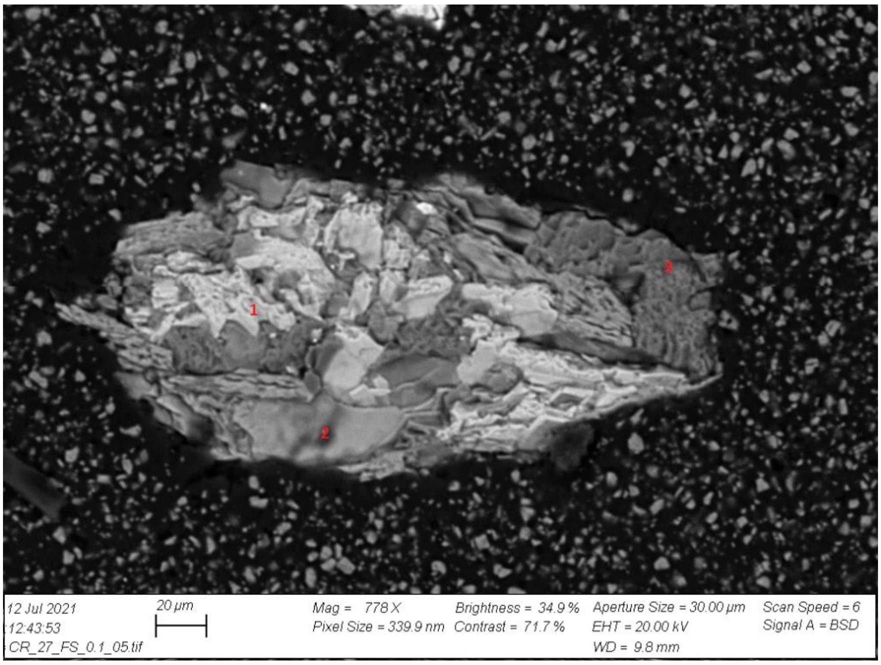

Figure 4.13: A lithoclast composed of rutile (1), phlogopite (2), and albite (3) in magnetic fraction at 0.1 A (CR-27 < 150 µm)

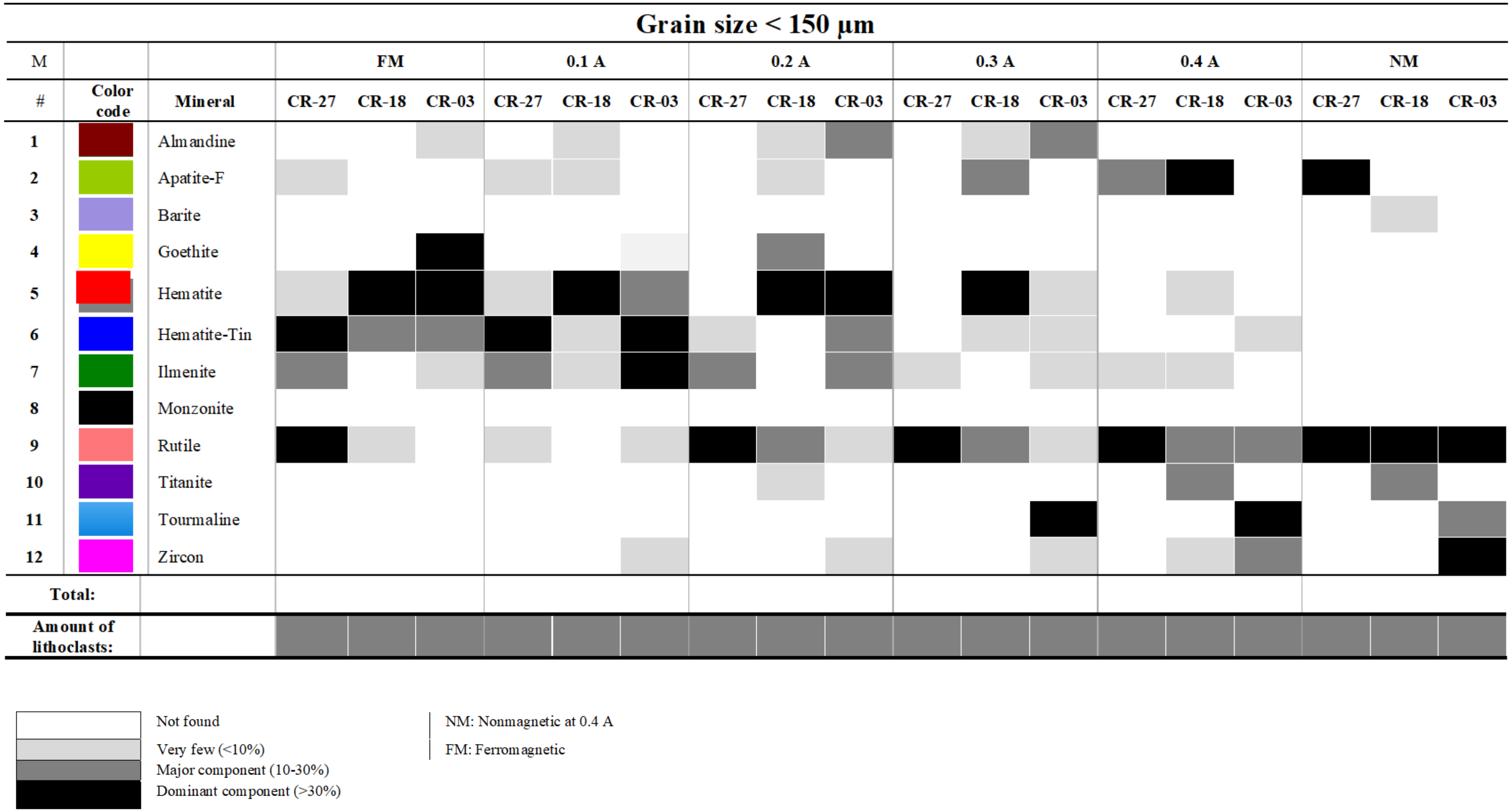

Grain size < 150 µm

M			FM			0.1 A			0.2 A			0.3 A			0.4 A			NM		
#	Color code	Mineral	CR-27	CR-18	CR-03	CR-27	CR-18	CR-03	CR-27	CR-18	CR-03	CR-27	CR-18	CR-03	CR-27	CR-18	CR-03	CR-27	CR-18	CR-03
1	🟥	Almandine			░		░			░	▓		░	▓						
2	🟩	Apatite-F	░			░	░			░			▓		▓	█		█		
3	🟪	Barite																	░	
4	🟨	Goethite			█			░		▓										
5	🟥	Hematite	░	█	█	░	█	▓		█	█		█	░		░				
6	🟦	Hematite-Tin	█	▓	▓	█	░	█	░		▓		░	░			░			
7	🟩	Ilmenite	▓		░	▓	░	█	▓		▓	░		░	░	░				
8	⬛	Monzonite																		
9	🟥	Rutile	█	░		░		░	█	▓	░	█	▓	░	█	▓	▓	█	█	█
10	🟪	Titanite								░						▓			▓	
11	🟦	Tourmaline												█			█			▓
12	🟪	Zircon						░			░			░		░	▓			█
Total:																				
Amount of lithoclasts:			▓	▓	▓	▓	▓	▓	▓	▓	▓	▓	▓	▓	▓	▓	▓	▓	▓	▓

□	Not found
░	Very few (<10%)
▓	Major component (10-30%)
█	Dominant component (>30%)

NM: Nonmagnetic at 0.4 A

FM: Ferromagnetic

Figure 4.14: The % of each mineral in all three samples at different magnetic field strength for grain size fraction <150 µm. The values are % of total heavy minerals identified using EDS.

Apart from these, another group mineral, such as Apatitie-F, Zircon, Monzanite, Barite and Titanite are expected to extract at higher magnetic field strength shown in Table 1.1. The mineral should not be in the magnetic fraction however their presence indicates the separation done by Geotrack international, did not captured these non-magnetic minerals. The reason could be their presence as locked grains; therefore they were not removed completely during separation of non-magnetic fractions in Australia.

The most effective separation by Frantz is done for tourmaline for grain sizes i.e. un-sieved and <150 µm. This mineral is only found in CR-03 (phyllite) and is restricted to 0.3 A and 0.4 A as an abundant component (>30%) in both un-sieved grain size and grain size fraction <150 µm. In grain size fraction <250 µm. The sample CR-03 has less concentration of clast in un-sieved fraction and grain size fraction <150 µm, therefore it show effective separation, whereas in grain size fraction <250 µm the quartz are in abundance (>30%) where it retained at 0.2 A instead of 0.3 A and 0.4 A (Figure 4.11, Figure 4.12, and Figure 4.13).

The minerals like tourmaline and monzonite have been found only restricted to phyllite (CR-03). Similarly, titanite and barite are constrained to only one sample i.e. CR-18. Minerals which are restricted to specific rock type can be determining heavy minerals for correlations.

From above discussion it can be said that it is possible to extract heavy minerals using Frantz which can characterize the rock for correlation.

4.4 General comparison between analytical methods used in the project.

The FEM-SEM, together with EDS, is a valuable tool for gain semi-quantitative heavy mineral data. However, this method gives only some idea of heavy mineral content in the whole rock. The values are not as accurate, such as it cannot distinguish between polymorphic minerals.

XRD is a useful technique to give idea of mineralogy present in a sample. It is the only method capable of making a distinction between polymorphic minerals. Furthermore, this method aids when wanting to confirm whether the interpretation done by FE-SEM and EDS is correct or not.

Therefore, a combination of FE-SEM-EDS with other analytical techniques such as XRD provides accurate results. Relying on one approach would not be beneficial, and data could be highly misleading in some cases.

4.5 Reliability of data

The analysis carried out in the thesis project using different analytical techniques has a certain source of error; therefore, it is crucial to consider data reliability. The error can be a human error, or the sample could get contamination, which is generally unlikely. During mounting, the grain picking needs to be random, but with humans' possibility of making choice, it is not entirely random.

During the separation of minerals, in Frantz, the increase in vibration intensity of a chute and aluminum plate could force minerals to go in wrong fraction. The use of EDS has a possibility of error in the resolution, interaction of x-rays with a sample, and detector calibration. During polishing of mounts, some grain loss for a certain fraction could damage the proper representation of fraction.

During the interpretation process, some of the minerals could be identified as a wrong mineral. Some of the tourmalines may be amphibole. Due to low amount of these mineral, they do not create large peak and FE-SEM-EDS analysis only gives elemental composition which could be unclear in indicating the exact mineral type. The BSE images were analyzed to keep interpretation correct as much as possible. If some of the grains are designated wrong mineral type, then most likely it does not apply to most of the grains, and the outcomes will be the same as interpreted.

5 Conclusions

An attempt was made to illustrate the effectiveness of Frantz isodynamic separator for separation of heavy minerals from rock sample of varied size. The value of this method is illustrated by selecting three rock sample (CR-27, CR-03 and CR-18) from Rosh Pinah Formation, Grootderm Formation and Vredefontein Formation. The samples chosen for the study are free from zircon fraction, zircon concentrate and apatite fraction. For the three different grain sizes (un-sieved sample fraction, grain size <250 µm, and grain size <150 µm) the separation of each sample in Frantz is carried out by applying magnetic field strength ranging from 0.1A to 0.4 A.

The analytical methods FE-SEM-EDS and XRD identifies both light and heavy mineral concertation in all three rock samples. Light minerals such as albite, quartz, phlogopite, chlorite and feldspars are found as relict of magnetic separation in different magnetic fractions for all three rock units in all grain sizes (un-sieved sample fraction, grain size <250 µm, and grain size <250 µm). The abundance of light minerals at low strength magnetic field is largely because of lithoclasts and presence of impurities.

Comparison of different lithological units (i.e. phyllite, amphibolite and lava) suggest that, some heavy minerals, like almandine, hematite, tin bearing hematite, ilmenite are found mostly in their expected range of extraction with some exemptions e.g. goethite which has best range of extraction at 0.2 and 0.3 A but is dominating in FM fraction of sample CR-03 for grain size fraction <150 µm. However, these minerals are not restricted to a specific fraction instead they have range.

Mineral rutile shows wide range of distribution and is usually expected to extract at magnetic field strength > 1.7 A, but its abundance in fractions of low magnetic field strength could be due to its occurrence in the form locked grain or due to impurities.

Non-magnetic minerals such as apatite-F, zircon, monzonite, barite are also found in rock samples at low magnetic field strength for different grain size fractions (un-sieved sample fraction, grain size <250 µm, and grain size <150 µm). The presence of non-magnetic minerals in magnetic fraction could be result of their occurrence as locked grain with mineral of higher paramagnetic susceptibility. This also proves infective separation of non-magnetic minerals from the magnetic fractions.

Among all the heavy minerals, only tourmaline is effectively separated for the rock sample CR-03, in Frantz and show its dominance in specific magnetic fractions at 0.2 A and 0.3 A for un-sieved grain fraction and grain size >150 µm. In grain size >250 µm, the separation of tourmaline is slightly affected by presence of lithoclasts therefore its dominance is found at 0.2 A.

Out of many, few heavy minerals such as tourmaline, monzonite, barite and titanite are found constrained to certain lithology. These heavy minerals can be used as determining parameter for correlation of these rocks.

6 Further work

Generally, testing of Frantz isodynamic separator for same rock samples but with further small grain size can be recommended. It would be interesting to check effectivity of Frantz for grain size 70 µm to 100 µm. The smaller grain size is expected to have low amount of lithoclasts, which may increase the effectivity of Frantz. Moreover the analysis of separated fractions with The EMPA (Electron Microprobe Analysis) can prove more efficient to distinguish between different minerals and phases which in SEM shows similar characteristics.

7 References

Alchin, D., Frimmel, H., & Jacobs, L. (2005). Stratigraphic setting of the metalliferous Rosh Pinah Formation and the Spitzkop and Koivib suites in the Pan-African Gariep Belt, southwestern Namibia. *South African Journal of Geology, 108*(1), 19-34.

Basei, M. A. S., Frimmel, H., Nutman, A. P., Preciozzi, F., & Jacob, J. (2005). A connection between the Neoproterozoic Dom Feliciano (Brazil/Uruguay) and Gariep (Namibia/South Africa) orogenic belts–evidence from a reconnaissance provenance study. *Precambrian Research, 139*(3-4), 195-221.

Deer, W. A., Howie, R. A., & Zussman, J. (2013). *An Introduction to the Rock-forming Minerals*: Mineralogical Society.

Egerton, R. F. (2016). Physical principles of electron microscopy : an introduction to TEM, SEM, and AEM.

Fölling, P., & Frimmel, H. E. (2002). Chemostratigraphic correlation of carbonate successions in the Gariep and Saldania Belts, Namibia and South Africa. *Basin Research, 14*(1), 69-88.

Frimmel, H., Basei, M., & Gaucher, C. (2011). Neoproterozoic geodynamic evolution of SW-Gondwana: a southern African perspective. *International Journal of Earth Sciences, 100*(2), 323-354.

Frimmel, H., & Jiang, S.-Y. (2001). Marine evaporites from an oceanic island in the Neoproterozoic Adamastor ocean. *Precambrian Research, 105*(1), 57-71.

Frimmel, H. E. (2018). The Gariep Belt. In *Geology of Southwest Gondwana* (pp. 353-386): Springer.

Frimmel, H. E., Hartnady, C. J., & Koller, F. (1996). Geochemistry and tectonic setting of magmatic units in the Pan-African Gariep Belt, Namibia. *Chemical Geology, 130*(1-2), 101-121.

Frimmel, H. E., Hartnady, C. J. H., & Koller, F. (1996). Geochemistry and tectonic setting of magmatic units in the Pan-African Gariep Belt, Namibia. *Chemical Geology, 130*(1-2), 101-121. doi:10.1016/0009-2541(95)00188-3

Germs, G. J. (1995). The Neoproterozoic of southwestern Africa, with emphasis on platform stratigraphy and paleontology. *Precambrian Research, 73*(1-4), 137-151.

Goldstein, J., Newbury, D. E., Michael, J. R., Ritchie, N. W. M., Scott, J. H. J., & Joy, D. C. (2018). *Scanning electron microscopy and x-ray microanalysis*. New York, NY: Springer.

Gopi, S. P., & Subramanian, V. K. (2012). Polymorphism in CaCO3—Effect of temperature under the influence of EDTA (di sodium salt). *Desalination, 297*, 38-47.

Hein, J. R., Zierenberg, R. A., Maynard, J. B., & Hannington, M. D. (2007). Barite-forming environments along a rifted continental margin, Southern California Borderland. *Deep Sea Research Part II: Topical Studies in Oceanography, 54*(11-13), 1327-1349. doi:10.1016/j.dsr2.2007.04.011

Hessenbruch, A. (2002). A brief history of x-rays. *Endeavour, 26*(4), 137-141.

Leng, Y. (2013). *Materials Characterization: Introduction to Microscopic and Spectroscopic Methods* (2nd ed.): Wiley-VCH, Weinheim, Germany,.

Macdonald, F. A., Strauss, J. V., Rose, C. V., Dudás, F. Ő., & Schrag, D. P. (2010). Stratigraphy of the Port Nolloth Group of Namibia and South Africa and implications for the age of Neoproterozoic iron formations. *American Journal of Science, 310*(9), 862-888.

Martin, H. (1965). The Precambrian geology of South West Africa and Namaqualand: Precambrian Res. *Unit, Univ. Cape Town, 159.*

Middlemost, E. (1966). The genesis of the Stinkfontein Formation. *South African Journal of Geology, 69*(01), 87-98.

Middlemost, E. A. K. (1963). *Geology of the south-eastern Richtersveld.* University of Cape Town,

Morton, A. C. (1985). Heavy Minerals in Provenance Studies. In G. G. Zuffa (Ed.), *Provenance of Arenites* (pp. 249-277). Dordrecht: Springer Netherlands.

Nesse, W. D. (2000). *Introduction to mineralogy*. New York: Oxford University Press.

Oberteuffer, J. (1974). Magnetic separation: A review of principles, devices, and applications. *IEEE Transactions on Magnetics, 10*(2), 223-238.

Oder, R. (1976). High gradient magnetic separation theory and applications. *IEEE Transactions on Magnetics, 12*(5), 428-435.

Reed, S. J. B. (2005). *Electron microprobe analysis and scanning electron microscopy in geology*: Cambridge university press.

Rosenblum, S., & Brownfield, I. K. (2000). *Magnetic susceptibilities of minerals*: Citeseer.

Schorn, S., & Diener, J. (2017). Details of the gabbro-to-eclogite transition determined from microtextures and calculated chemical potential relationships. *Journal of Metamorphic Geology, 35*(1), 55-75.

Siegesmund, S., Basei, M. A., Oyhantçabal, P., & Oriolo, S. (2018). *Geology of Southwest Gondwana*: Springer.

Strong, T. R., & Driscoll, R. L. (2016). *A process for reducing rocks and concentrating heavy minerals* (2331-1258). Retrieved from

Thomas, R. J., Macey, P. H., Spencer, C., Dhansay, T., Diener, J. F., Lambert, C. W., . . . Nguno, A. (2016). The Sperrgebiet Domain, Aurus Mountains, SW Namibia: A∼ 2020–850 Ma window within the Pan-African Gariep Orogen. *Precambrian Research, 286*, 35-58.

Ul-Hamid, A. (2018). *A beginner's guide to scanning electron microscopy*. Cham: Springer.

Van der Voo, R., & French, R. (1974). Apparent polar wandering for the Atlantic-bordering continents: Late Carboniferous to Eocene. *Earth-Science Reviews, 10*(2), 99-119.

Von Veh, M. W. (1988). The stratigraphy and structural evolution of the Late Proterozoic Gariep Belt in the Sendelingsdrif-Annisfontein area, northwestern Cape Province.

Appendix A: Spectrums from FE-SEM-EDS analyses.

#	Color code	Mineral
1	■	Albite
2	■	Andalusite
3	■	Anorthite
4	■	Anorthite Fe
5	■	Anorthoclase
6	■	Chlorite
7	■	Glauconite
8	■	Microcline
9	■	Muscovite
10	■	Orthoclase
11	■	Phlogopite
12	■	Quartz
13	■	Almandine
14	■	Apatite-F
15	■	Barite
16	■	Goethite
17	■	Hematite
18	■	Hematite-Tin
19	■	Ilmenite
20	■	Monzonite
21	■	Rutile
22	■	Titanite
23	■	Tourmaline
24	■	Zircon

The minerals identified on the basis of spectrums obtained from FE-SEM-EDS analyses are listed as mineral 1-24. The EDS measurements taken from grains matching the spectrum 1-24 are named as the corresponding mineral type.

Albite

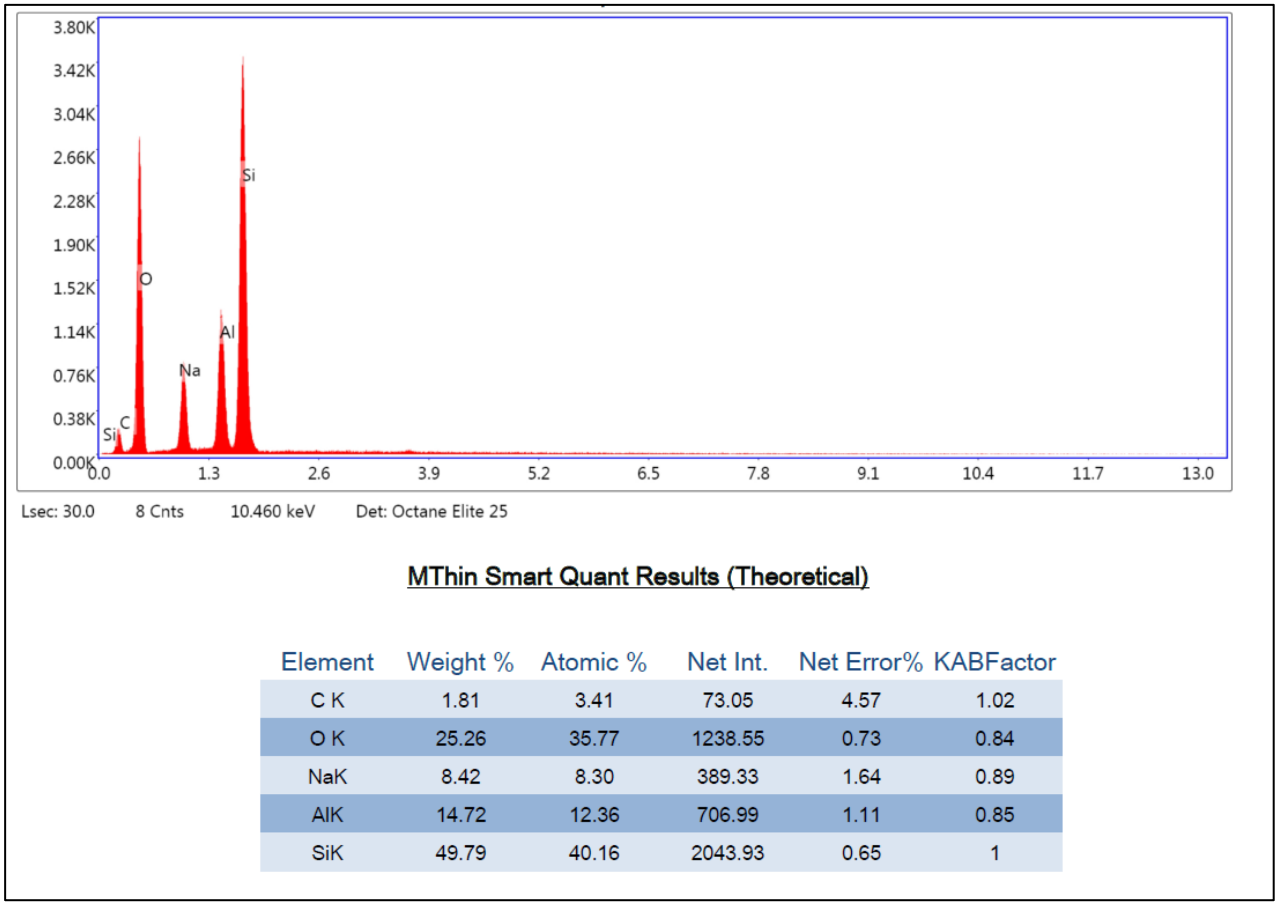

Lsec: 30.0 8 Cnts 10.460 keV Det: Octane Elite 25

MThin Smart Quant Results (Theoretical)

Element	Weight %	Atomic %	Net Int.	Net Error%	KABFactor
C K	1.81	3.41	73.05	4.57	1.02
O K	25.26	35.77	1238.55	0.73	0.84
NaK	8.42	8.30	389.33	1.64	0.89
AlK	14.72	12.36	706.99	1.11	0.85
SiK	49.79	40.16	2043.93	0.65	1

1. Andalusite

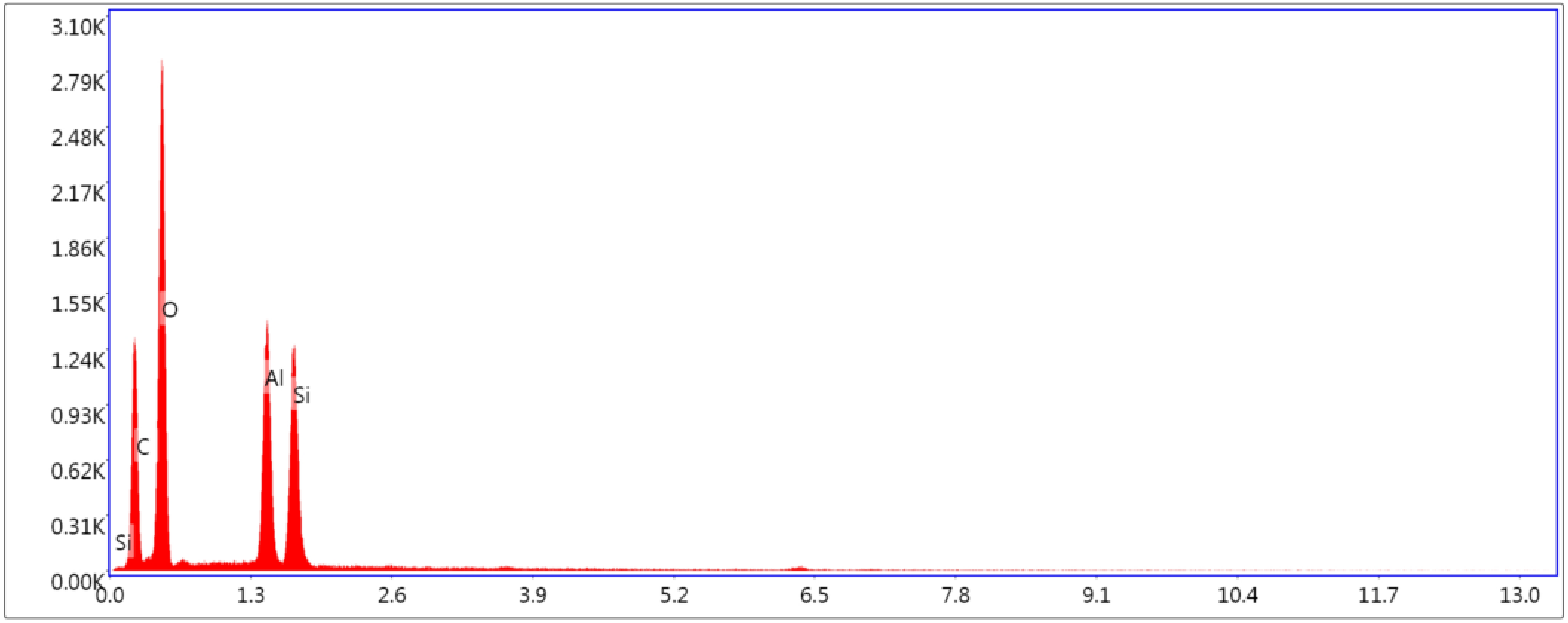

Lsec: 30.0 1.060K Cnts 1.735 keV Det: Octane Elite 25

MThin Smart Quant Results (Theoretical)

Element	Weight %	Atomic %	Net Int.	Net Error%	KABFactor
C K	18.52	28.36	572.21	1.21	1.02
O K	35.72	41.07	1340.11	0.82	0.84
AlK	22.22	15.15	816.75	1.12	0.85
SiK	23.54	15.42	739.57	1.39	1

2. Anorthite

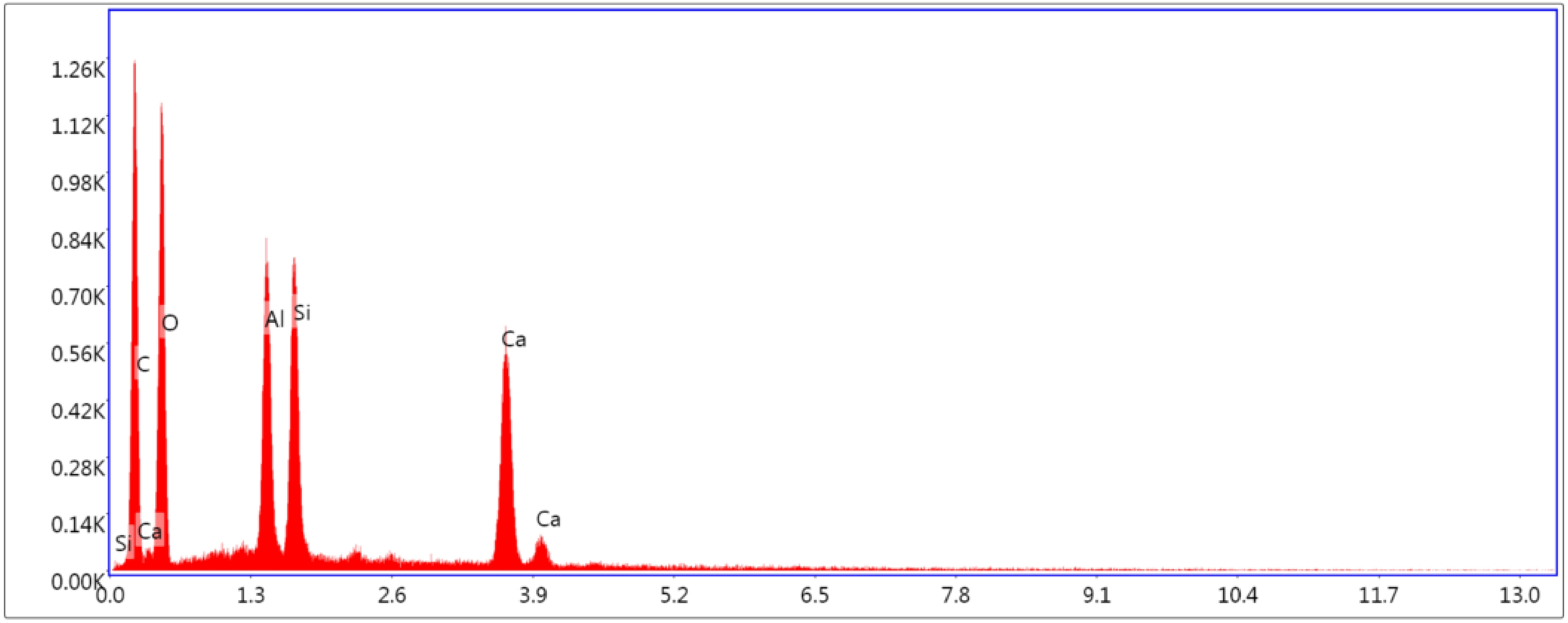

Lsec: 30.0 700 Cnts 1.735 keV Det: Octane Elite 25

MThin Smart Quant Results (Theoretical)

Element	Weight %	Atomic %	Net Int.	Net Error%	KABFactor
C K	22.01	37.92	522.41	1.34	1.02
O K	17.93	23.18	516.49	1.50	0.84
AlK	15.40	11.81	434.63	1.68	0.85
SiK	18.27	13.46	440.82	2.02	1
CaK	26.38	13.62	428.73	2.08	1.48

3. Anorthite-Fe

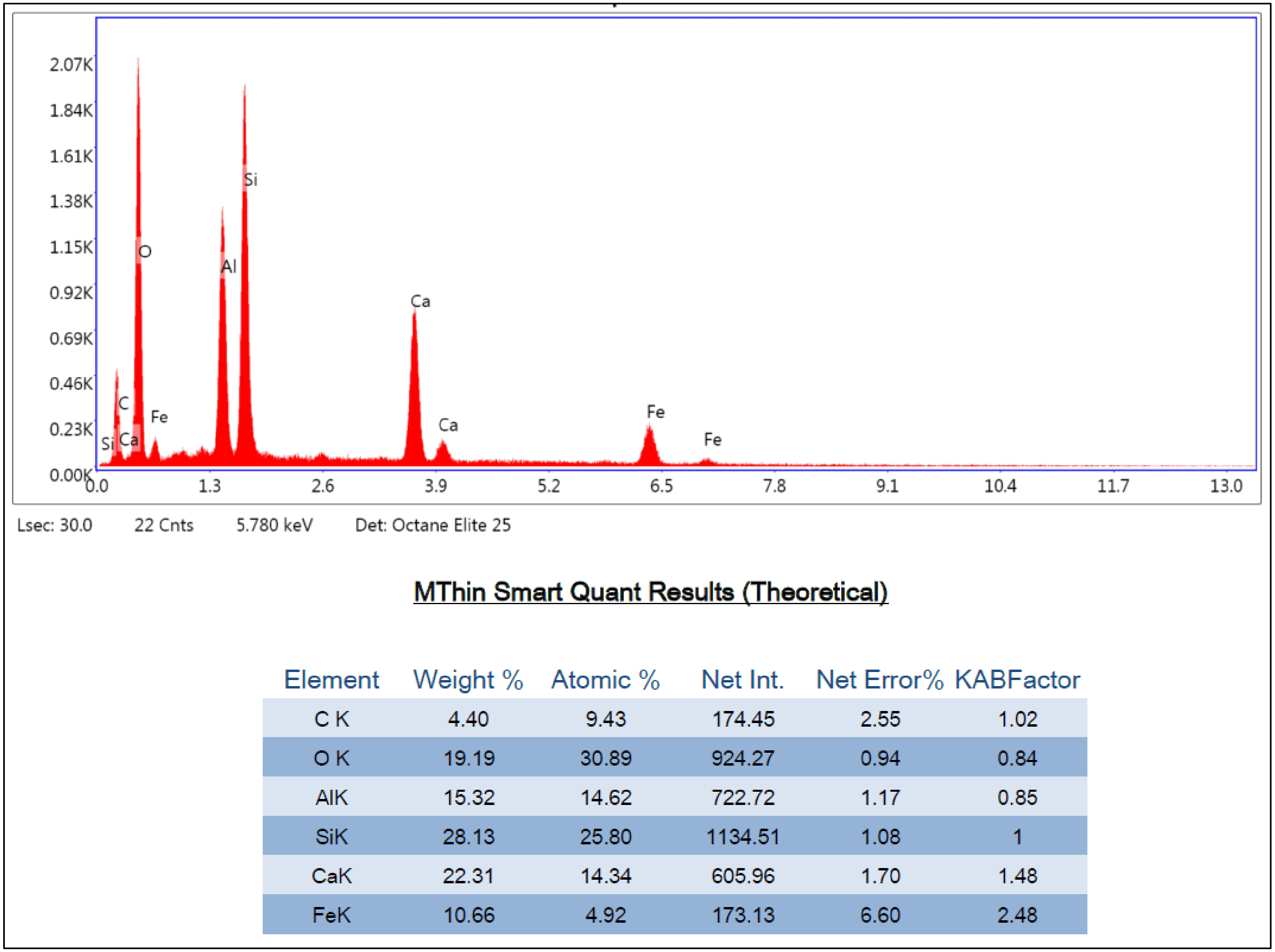

Lsec: 30.0 22 Cnts 5.780 keV Det: Octane Elite 25

MThin Smart Quant Results (Theoretical)

Element	Weight %	Atomic %	Net Int.	Net Error%	KABFactor
C K	4.40	9.43	174.45	2.55	1.02
O K	19.19	30.89	924.27	0.94	0.84
AlK	15.32	14.62	722.72	1.17	0.85
SiK	28.13	25.80	1134.51	1.08	1
CaK	22.31	14.34	605.96	1.70	1.48
FeK	10.66	4.92	173.13	6.60	2.48

4. Anorthoclase

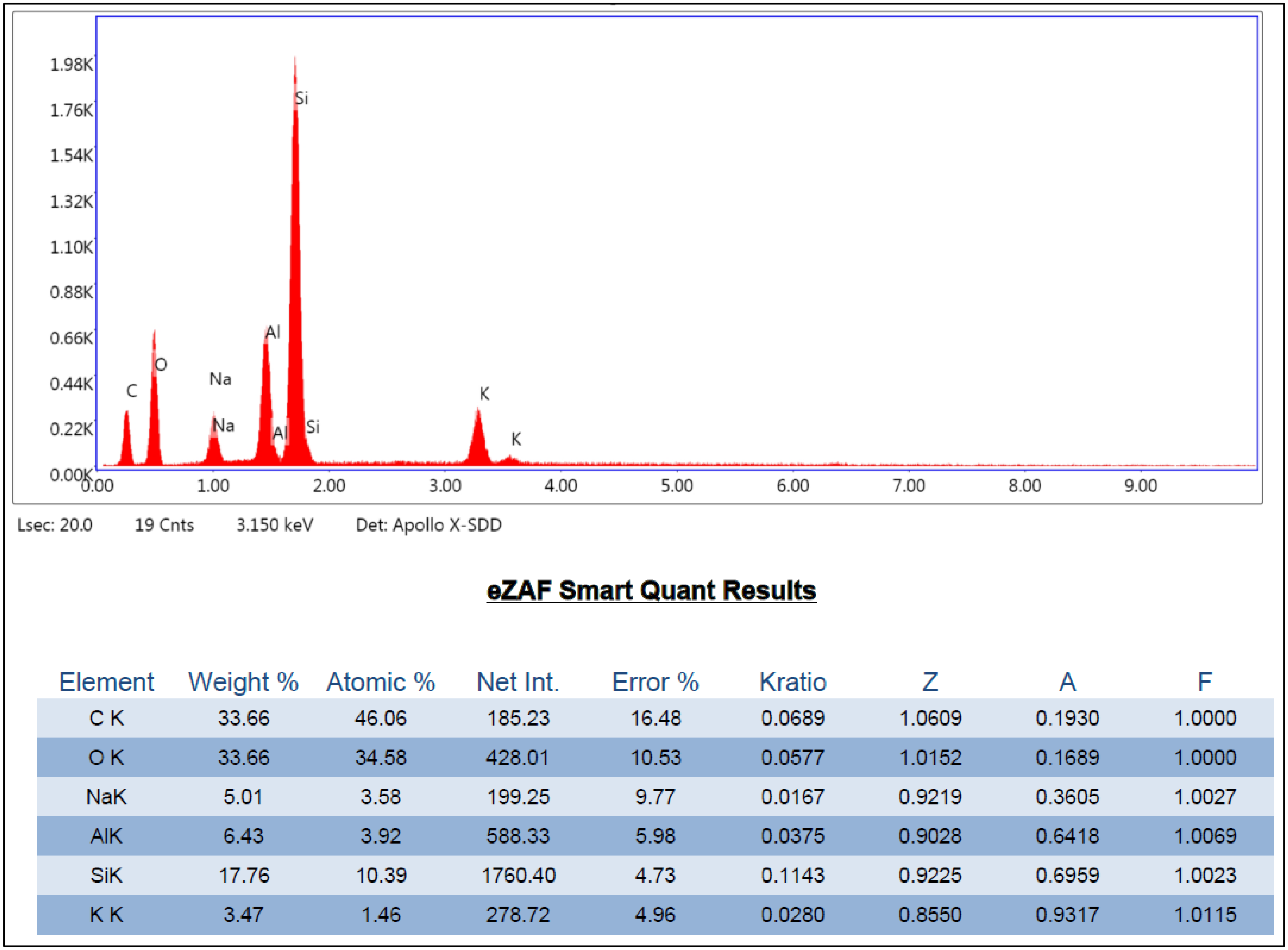

Lsec: 20.0 19 Cnts 3.150 keV Det: Apollo X-SDD

eZAF Smart Quant Results

Element	Weight %	Atomic %	Net Int.	Error %	Kratio	Z	A	F
C K	33.66	46.06	185.23	16.48	0.0689	1.0609	0.1930	1.0000
O K	33.66	34.58	428.01	10.53	0.0577	1.0152	0.1689	1.0000
NaK	5.01	3.58	199.25	9.77	0.0167	0.9219	0.3605	1.0027
AlK	6.43	3.92	588.33	5.98	0.0375	0.9028	0.6418	1.0069
SiK	17.76	10.39	1760.40	4.73	0.1143	0.9225	0.6959	1.0023
K K	3.47	1.46	278.72	4.96	0.0280	0.8550	0.9317	1.0115

5. Chlorite

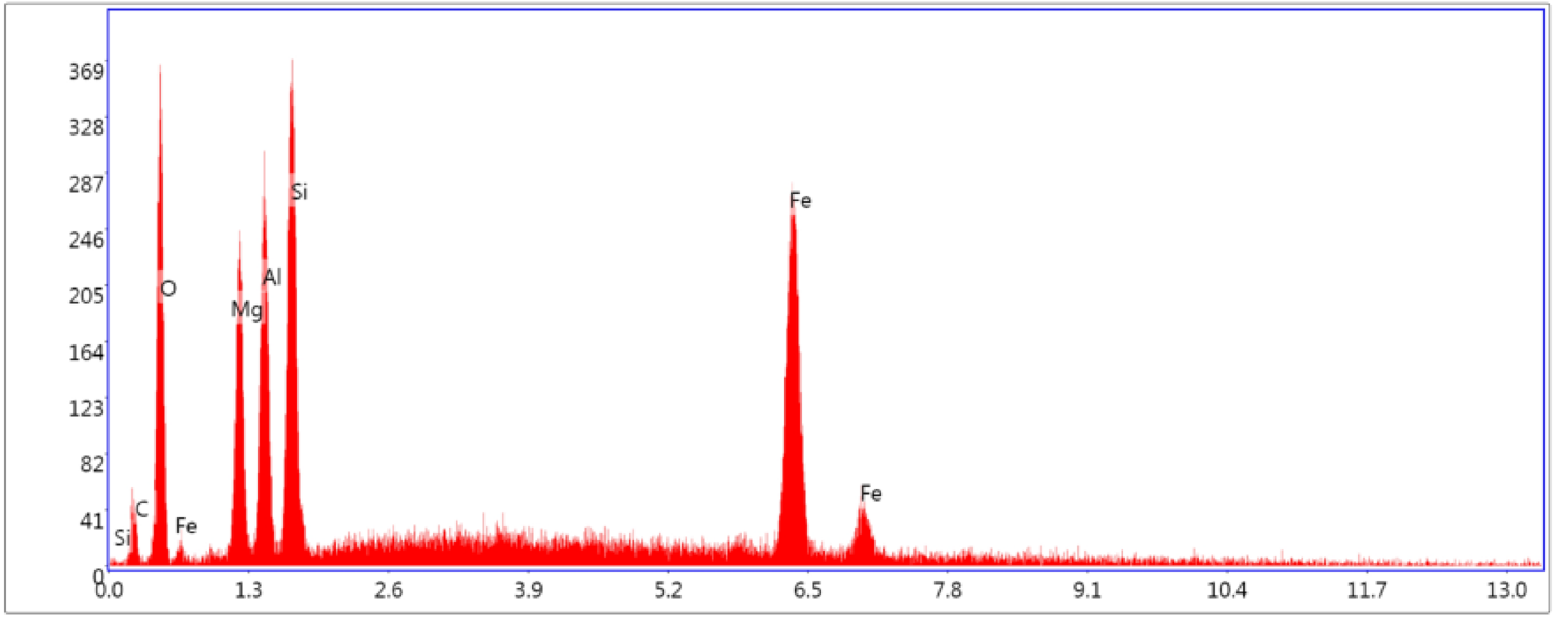

Lsec: 30.0 320 Cnts 1.735 keV Det: Octane Elite 25

MThin Smart Quant Results (Theoretical)

Element	Weight %	Atomic %	Net Int.	Net Error%	KABFactor
C K	0.94	2.59	10.96	20.08	1.02
O K	10.45	21.59	147.79	2.42	0.84
MgK	8.99	12.22	113.56	3.13	0.94
AlK	10.09	12.36	139.82	2.82	0.85
SiK	17.27	20.32	204.52	2.31	1
FeK	52.25	30.92	249.10	2.68	2.48

6. Glauconite

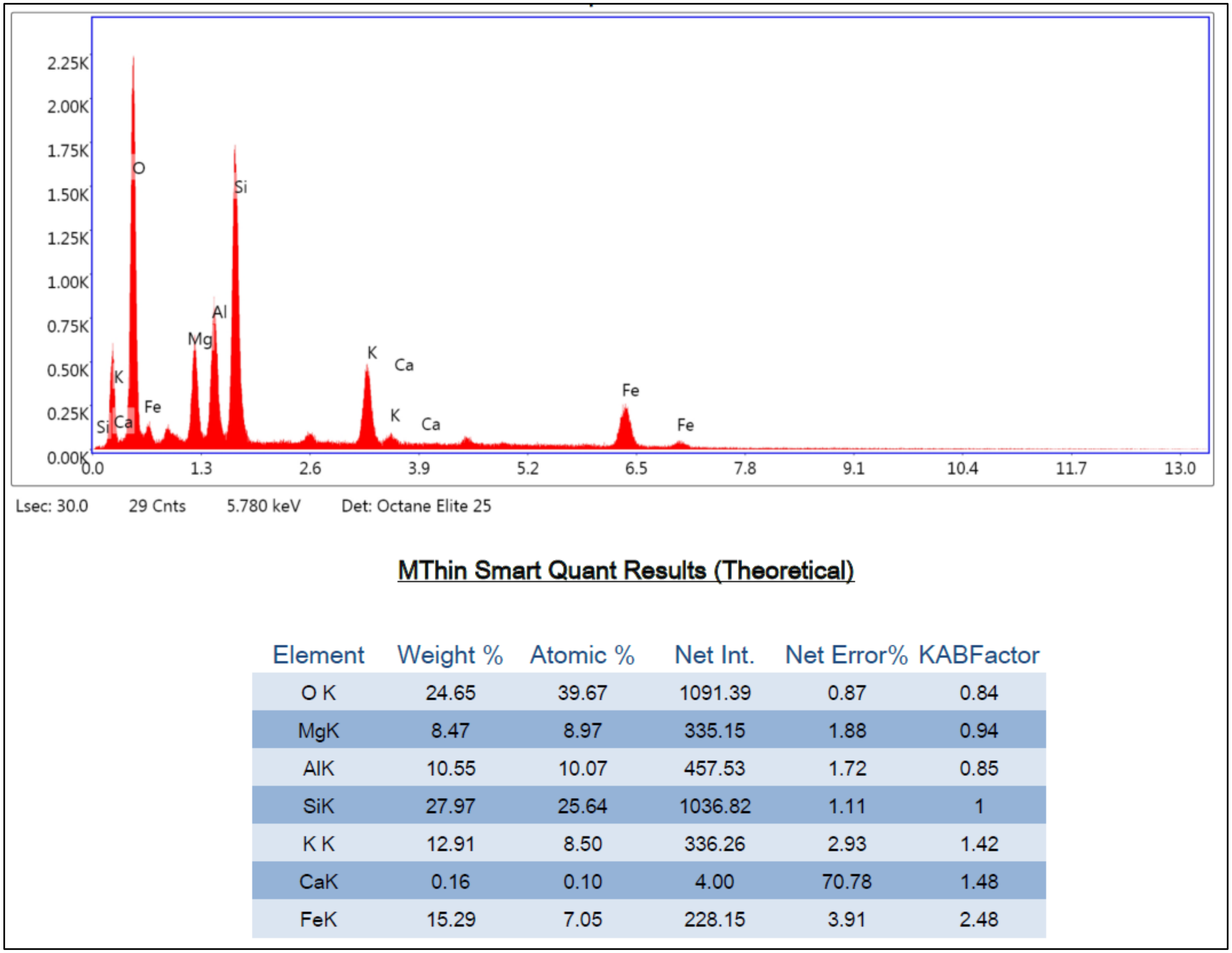

Lsec: 30.0 29 Cnts 5.780 keV Det: Octane Elite 25

MThin Smart Quant Results (Theoretical)

Element	Weight %	Atomic %	Net Int.	Net Error%	KABFactor
O K	24.65	39.67	1091.39	0.87	0.84
MgK	8.47	8.97	335.15	1.88	0.94
AlK	10.55	10.07	457.53	1.72	0.85
SiK	27.97	25.64	1036.82	1.11	1
K K	12.91	8.50	336.26	2.93	1.42
CaK	0.16	0.10	4.00	70.78	1.48
FeK	15.29	7.05	228.15	3.91	2.48

7. Microcline

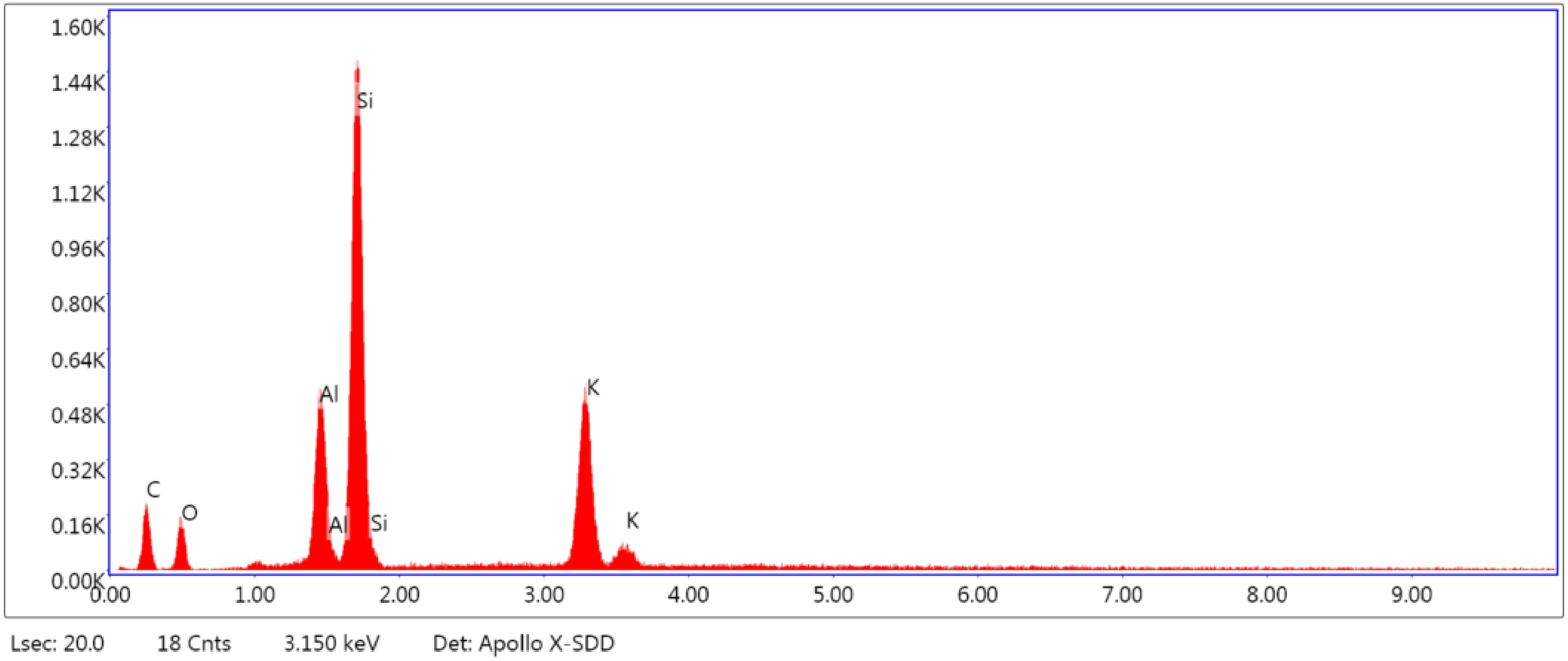

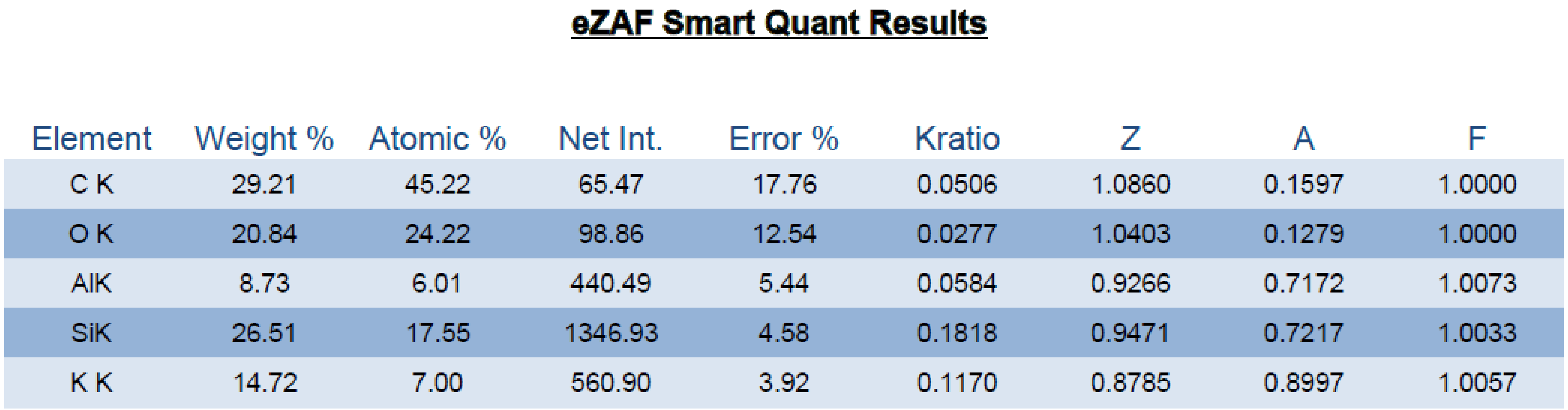

eZAF Smart Quant Results

Element	Weight %	Atomic %	Net Int.	Error %	Kratio	Z	A	F
C K	29.21	45.22	65.47	17.76	0.0506	1.0860	0.1597	1.0000
O K	20.84	24.22	98.86	12.54	0.0277	1.0403	0.1279	1.0000
AlK	8.73	6.01	440.49	5.44	0.0584	0.9266	0.7172	1.0073
SiK	26.51	17.55	1346.93	4.58	0.1818	0.9471	0.7217	1.0033
K K	14.72	7.00	560.90	3.92	0.1170	0.8785	0.8997	1.0057

8. Muscovite

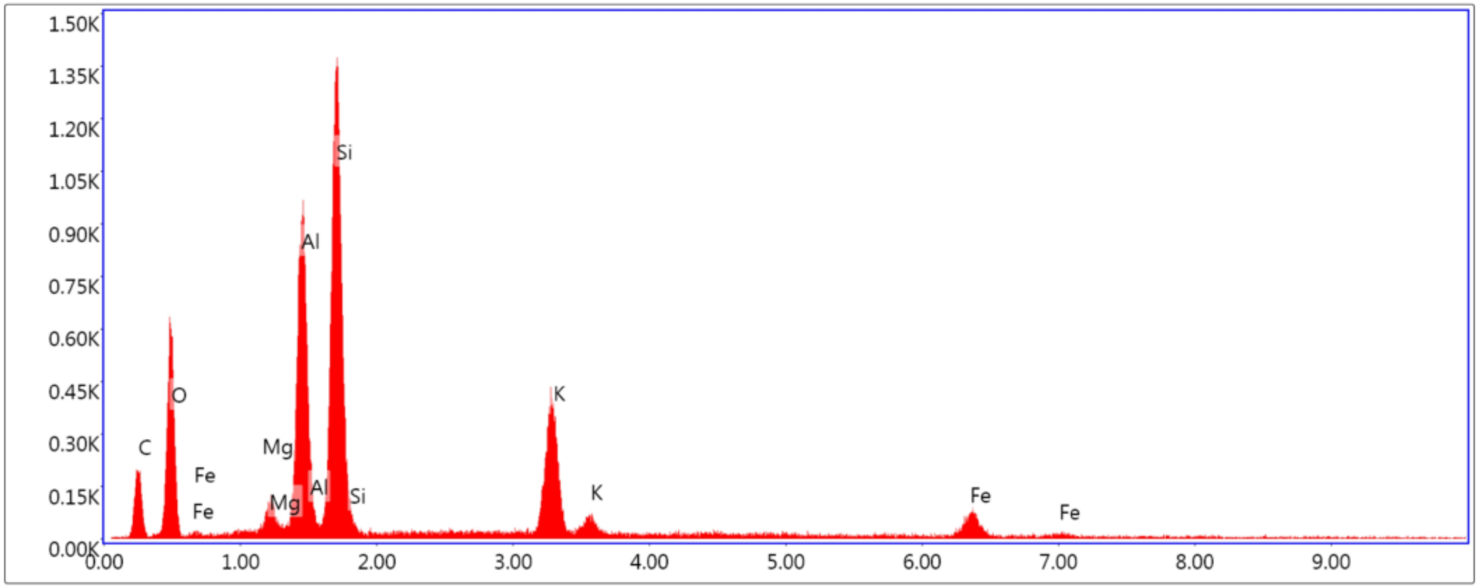

Lsec: 20.0 13 Cnts 3.150 keV Det: Apollo X-SDD

eZAF Smart Quant Results

Element	Weight %	Atomic %	Net Int.	Error %	Kratio	Z	A	F
C K	27.54	39.98	127.17	44.90	0.0557	1.0738	0.1885	1.0000
O K	35.64	38.85	400.27	10.53	0.0636	1.0281	0.1735	1.0000
MgK	1.39	1.00	83.75	11.11	0.0064	0.9502	0.4850	1.0042
AlK	10.56	6.83	814.29	5.80	0.0612	0.9151	0.6297	1.0047
SiK	15.34	9.53	1207.46	5.51	0.0923	0.9352	0.6414	1.0027
K K	6.24	2.79	428.96	4.09	0.0507	0.8672	0.9242	1.0123
FeK	3.29	1.03	102.47	8.39	0.0277	0.7873	1.0093	1.0612

9. Orthoclase

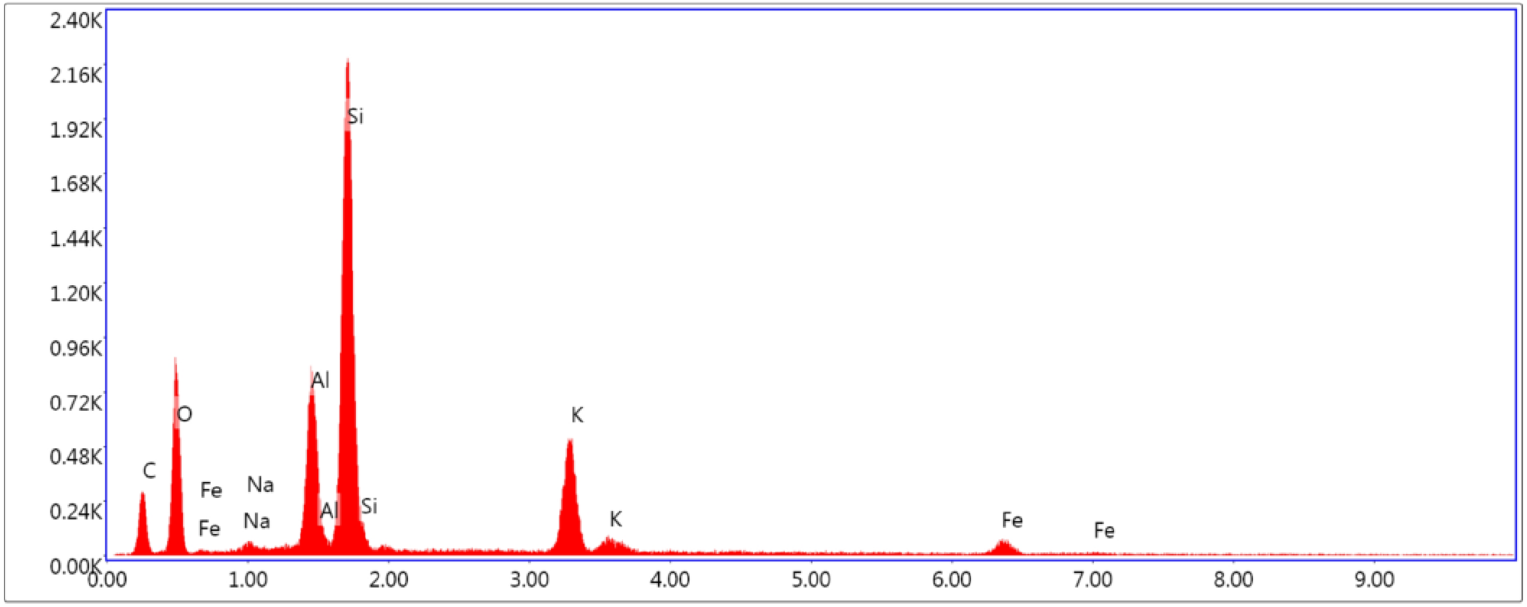

Lsec: 20.0 22 Cnts 3.150 keV Det: Apollo X-SDD

eZAF Smart Quant Results

Element	Weight %	Atomic %	Net Int.	Error %	Kratio	Z	A	F
C K	22.71	33.70	118.09	18.23	0.0433	1.0762	0.1771	1.0000
O K	39.11	43.58	555.61	10.27	0.0738	1.0304	0.1831	1.0000
NaK	1.35	1.05	49.25	15.48	0.0041	0.9363	0.3201	1.0024
AlK	7.62	5.04	709.41	6.01	0.0446	0.9172	0.6336	1.0060
SiK	20.24	12.84	2011.86	4.92	0.1286	0.9374	0.6764	1.0026
K K	6.84	3.12	557.03	3.84	0.0550	0.8692	0.9152	1.0108
FeK	2.12	0.68	79.46	12.41	0.0180	0.7890	1.0069	1.0663

10. Phlogopite

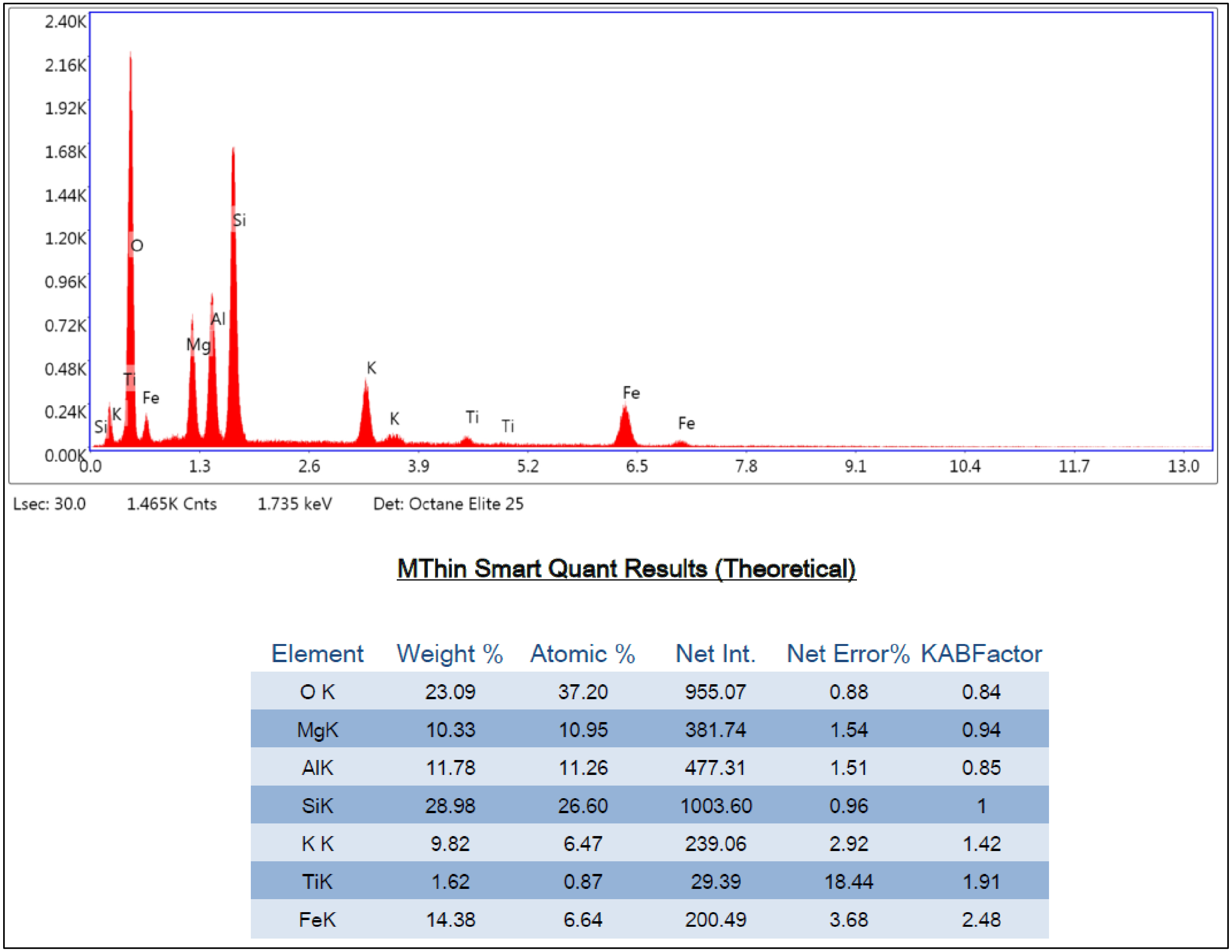

Lsec: 30.0 1.465K Cnts 1.735 keV Det: Octane Elite 25

MThin Smart Quant Results (Theoretical)

Element	Weight %	Atomic %	Net Int.	Net Error%	KABFactor
O K	23.09	37.20	955.07	0.88	0.84
MgK	10.33	10.95	381.74	1.54	0.94
AlK	11.78	11.26	477.31	1.51	0.85
SiK	28.98	26.60	1003.60	0.96	1
K K	9.82	6.47	239.06	2.92	1.42
TiK	1.62	0.87	29.39	18.44	1.91
FeK	14.38	6.64	200.49	3.68	2.48

11. Quartz

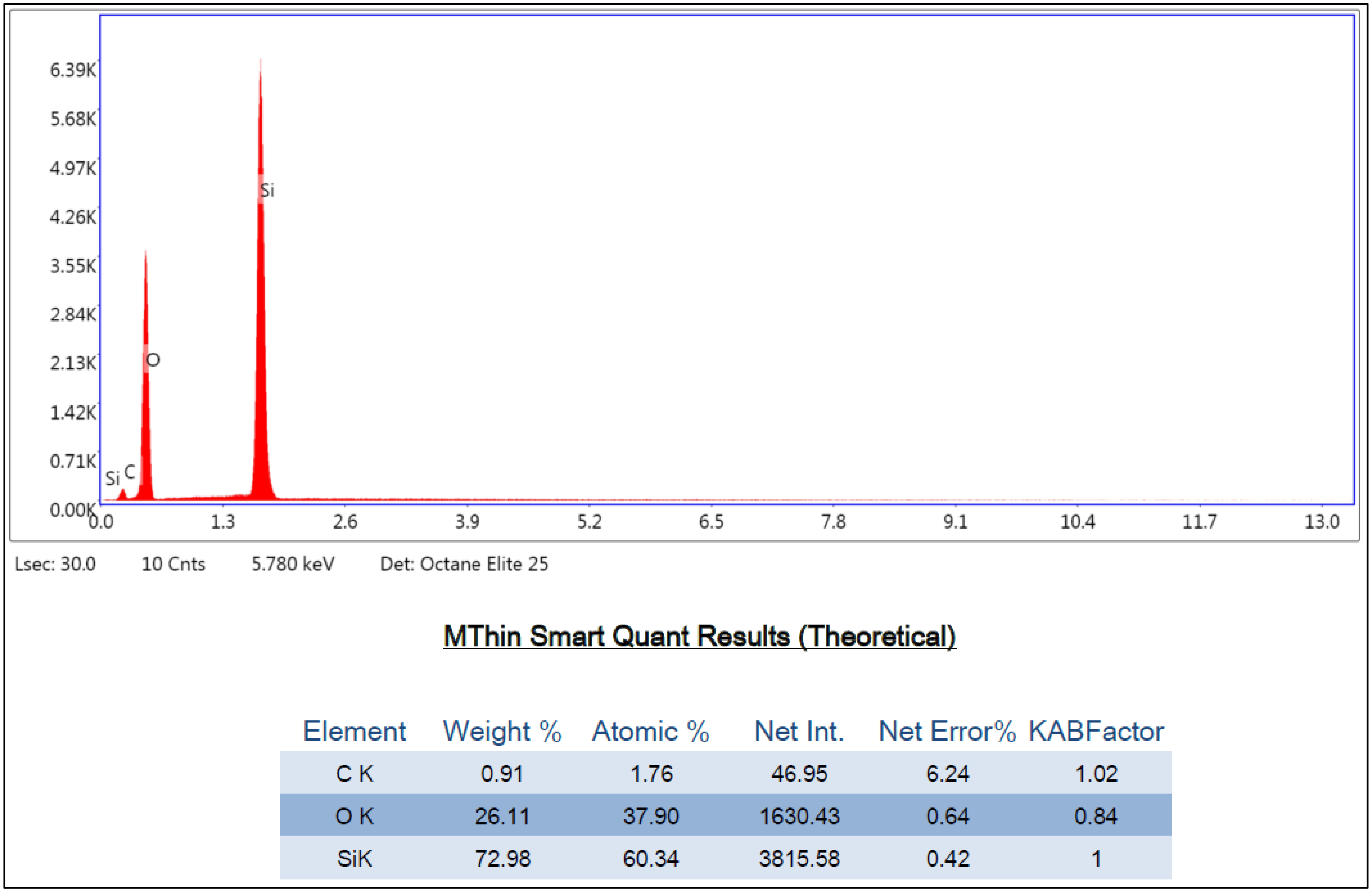

Lsec: 30.0 10 Cnts 5.780 keV Det: Octane Elite 25

MThin Smart Quant Results (Theoretical)

Element	Weight %	Atomic %	Net Int.	Net Error%	KABFactor
C K	0.91	1.76	46.95	6.24	1.02
O K	26.11	37.90	1630.43	0.64	0.84
SiK	72.98	60.34	3815.58	0.42	1

12. Almandine

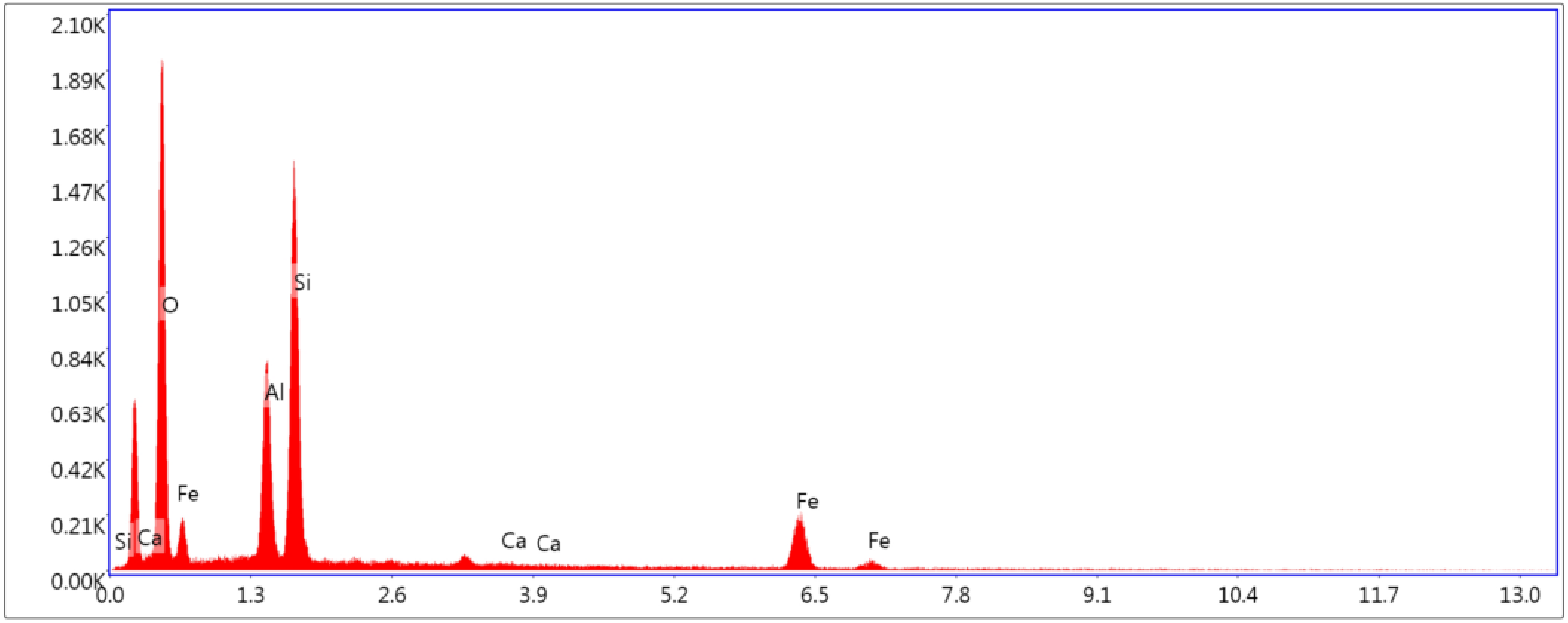

Lsec: 30.0 8 Cnts 5.780 keV Det: Octane Elite 25

MThin Smart Quant Results (Theoretical)

Element	Weight %	Atomic %	Net Int.	Net Error%	KABFactor
O K	30.30	46.55	891.59	0.94	0.84
AlK	15.58	14.19	448.96	1.53	0.85
SiK	35.31	30.90	870.01	1.12	1
CaK	0.44	0.27	7.23	59.03	1.48
FeK	18.38	8.09	182.37	3.40	2.48

13. Apatite-F

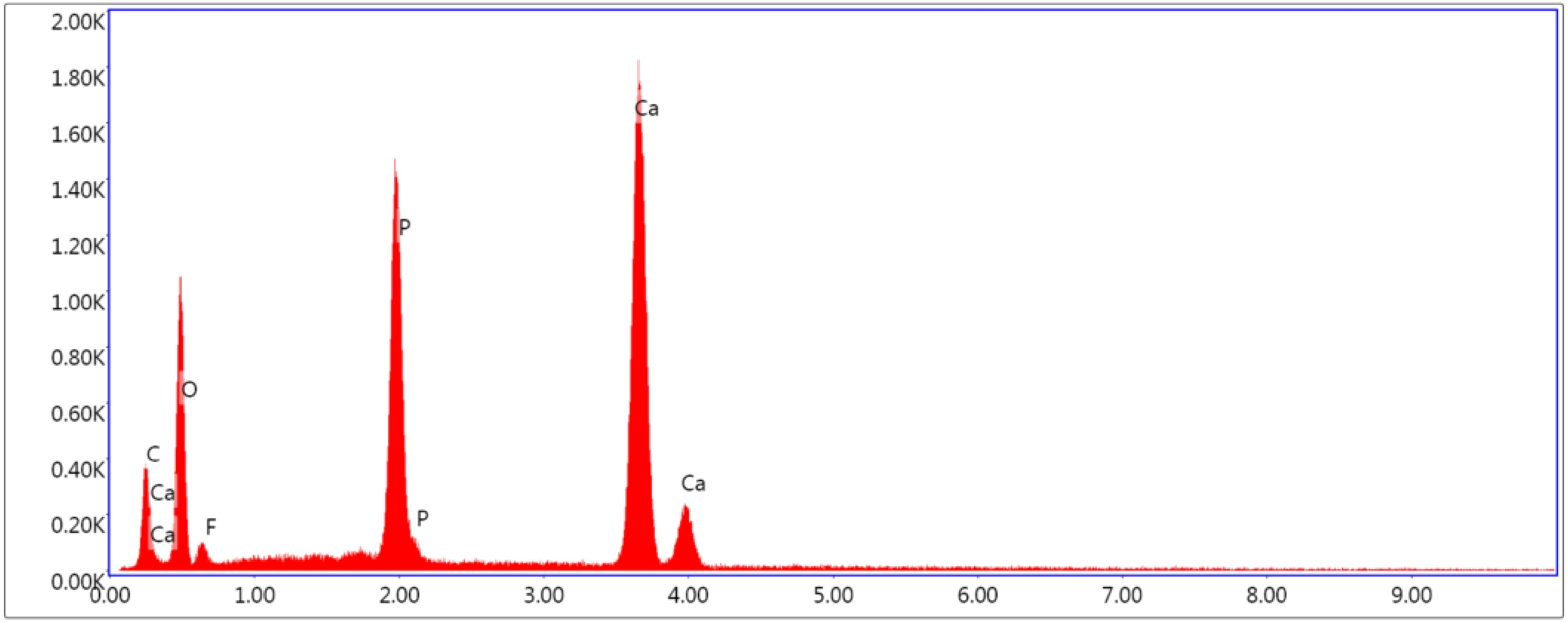

Lsec: 20.0 33 Cnts 3.150 keV Det: Apollo X-SDD

eZAF Smart Quant Results

Element	Weight %	Atomic %	Net Int.	Error %	Kratio	Z	A	F
C K	19.76	29.76	204.05	10.63	0.0556	1.0792	0.2607	1.0000
O K	43.85	49.57	650.26	10.51	0.0642	1.0336	0.1417	1.0000
F K	5.75	5.48	84.46	13.95	0.0056	0.9610	0.1019	1.0000
P K	10.27	6.00	1358.81	3.74	0.0766	0.9037	0.8186	1.0081
CaK	20.37	9.19	2042.65	1.96	0.1797	0.8885	0.9857	1.0068

14. Barite

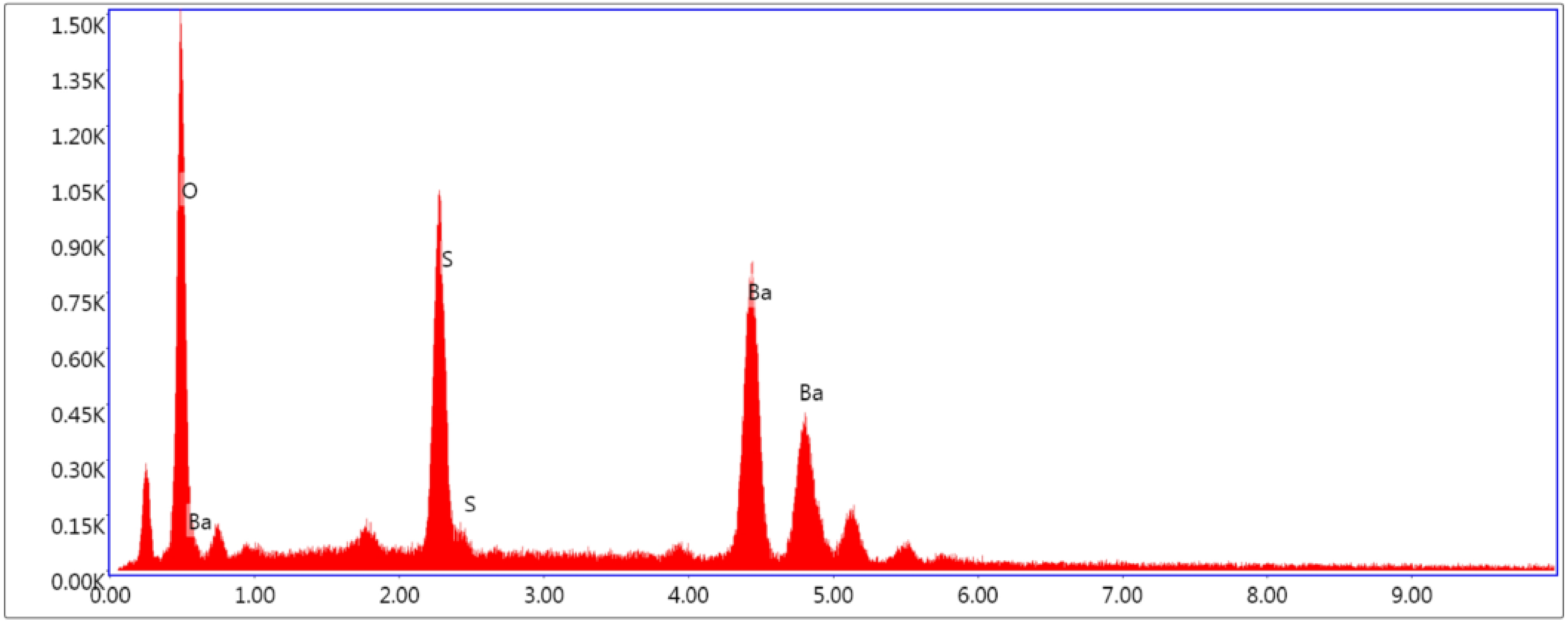

Lsec: 20.0 13 Cnts 6.840 keV Det: Apollo X-SDD

eZAF Smart Quant Results

Element	Weight %	Atomic %	Net Int.	Error %	Kratio	Z	A	F
O K	37.69	75.24	1152.94	8.06	0.1750	1.2227	0.3799	1.0000
S K	13.44	13.39	1088.80	6.52	0.0955	1.1061	0.6328	1.0151
BaL	48.87	11.37	1070.48	4.11	0.4048	0.7762	1.0677	0.9995

15. Goethite

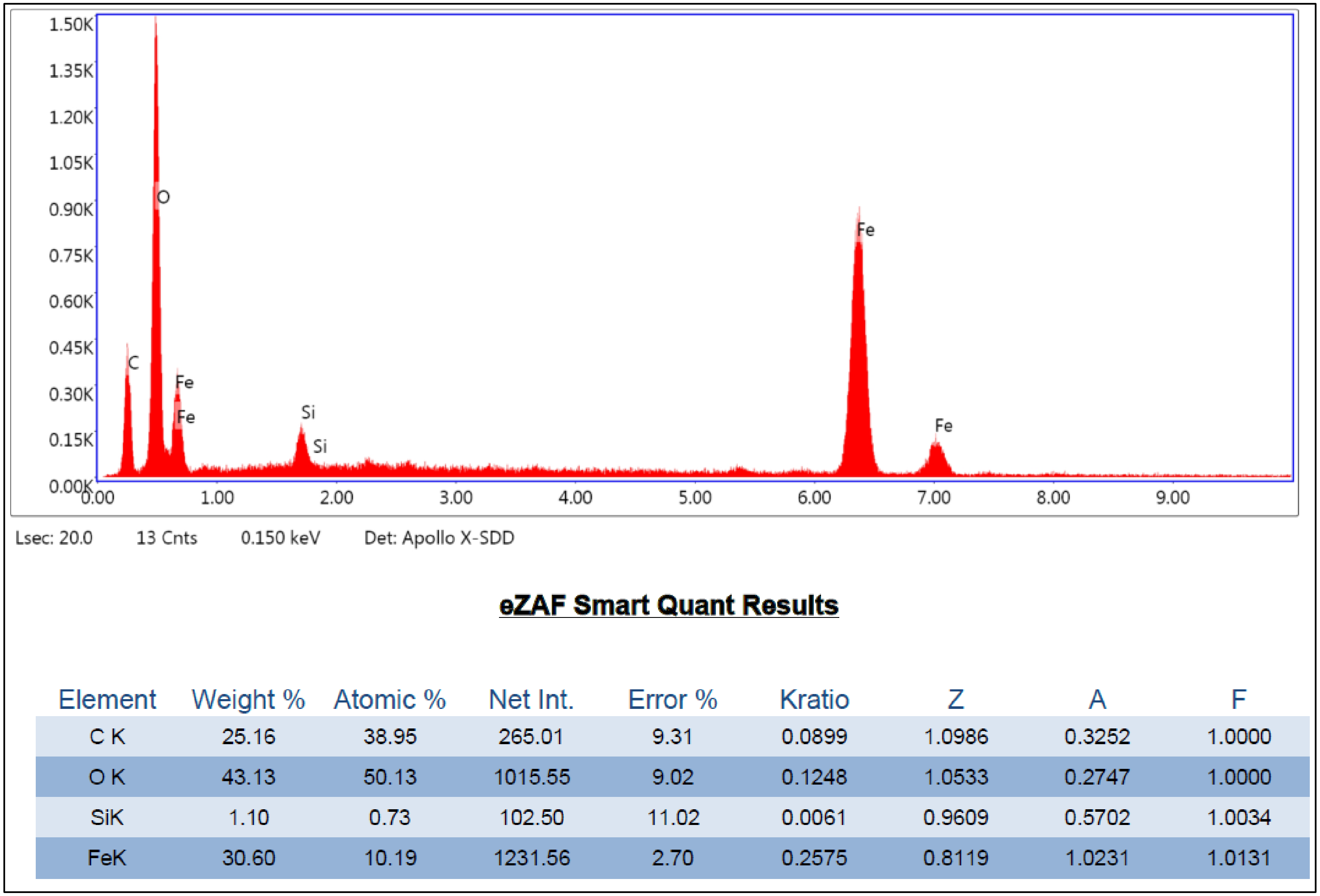

Lsec: 20.0 13 Cnts 0.150 keV Det: Apollo X-SDD

eZAF Smart Quant Results

Element	Weight %	Atomic %	Net Int.	Error %	Kratio	Z	A	F
C K	25.16	38.95	265.01	9.31	0.0899	1.0986	0.3252	1.0000
O K	43.13	50.13	1015.55	9.02	0.1248	1.0533	0.2747	1.0000
SiK	1.10	0.73	102.50	11.02	0.0061	0.9609	0.5702	1.0034
FeK	30.60	10.19	1231.56	2.70	0.2575	0.8119	1.0231	1.0131

16. Hematite

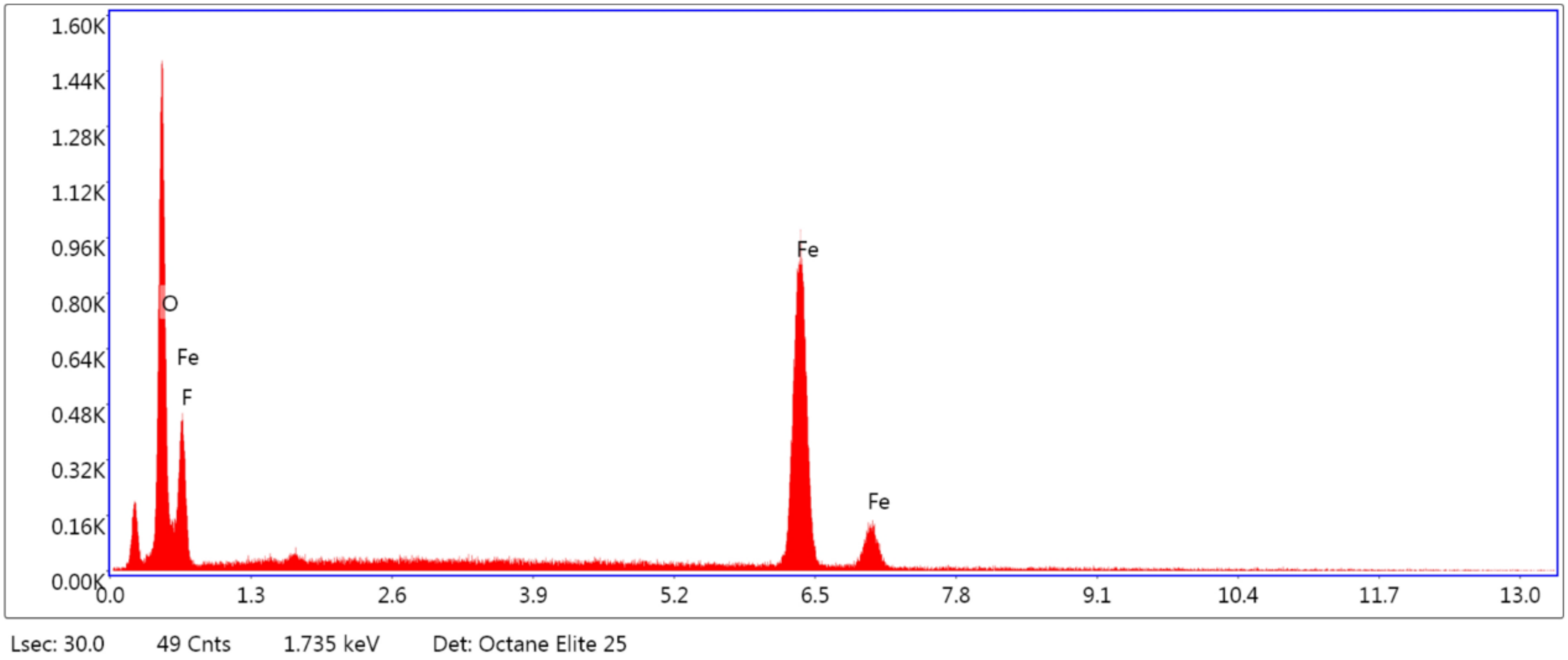

MThin Smart Quant Results (Theoretical)

Element	Weight %	Atomic %	Net Int.	Net Error%	KABFactor
O K	19.59	42.07	703.60	0.96	0.34
F K	7.09	12.82	167.56	2.84	0.51
FeK	73.33	45.12	887.89	1.08	1

17. Hematite-tin

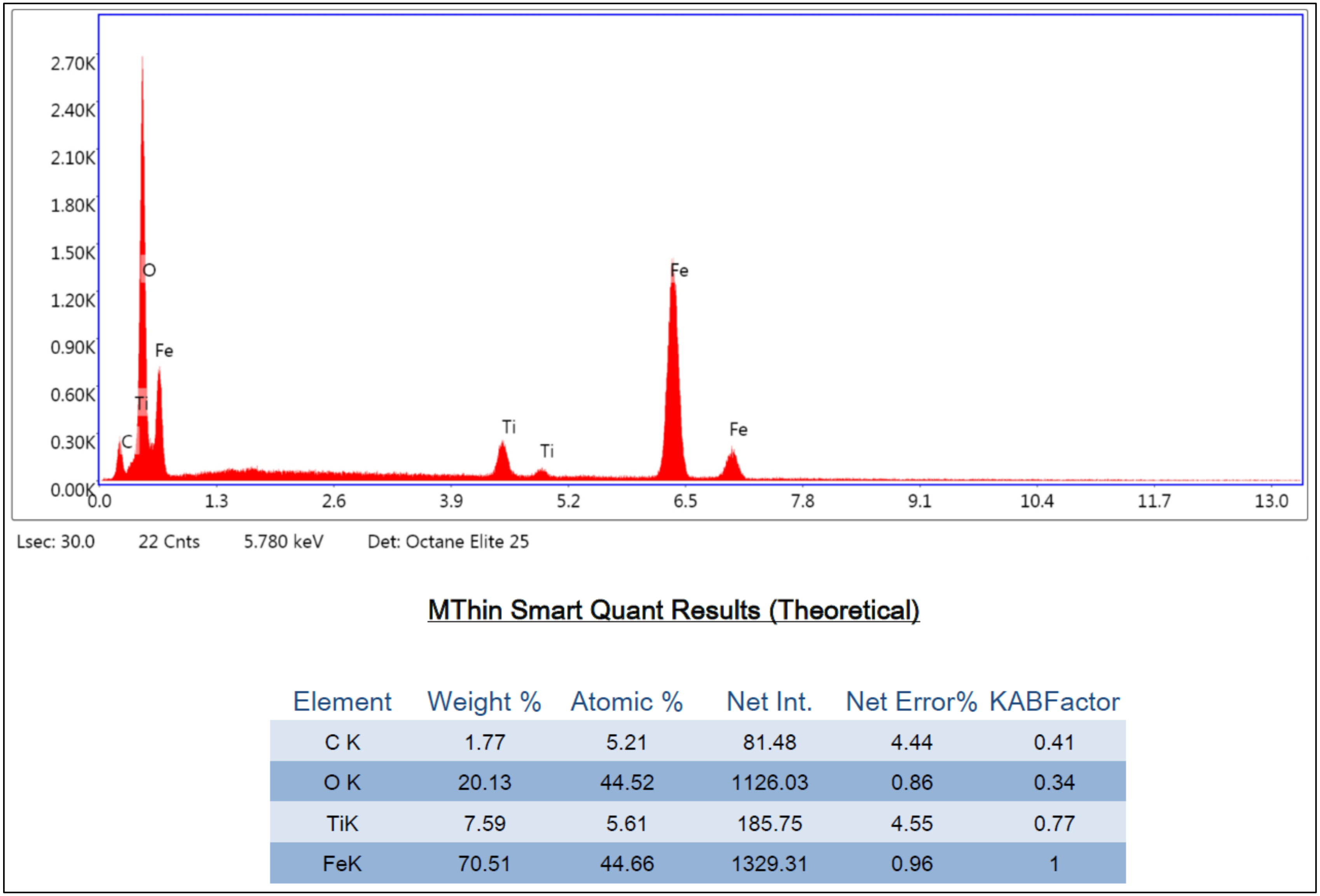

Lsec: 30.0 22 Cnts 5.780 keV Det: Octane Elite 25

MThin Smart Quant Results (Theoretical)

Element	Weight %	Atomic %	Net Int.	Net Error%	KABFactor
C K	1.77	5.21	81.48	4.44	0.41
O K	20.13	44.52	1126.03	0.86	0.34
TiK	7.59	5.61	185.75	4.55	0.77
FeK	70.51	44.66	1329.31	0.96	1

18. Ilmenite

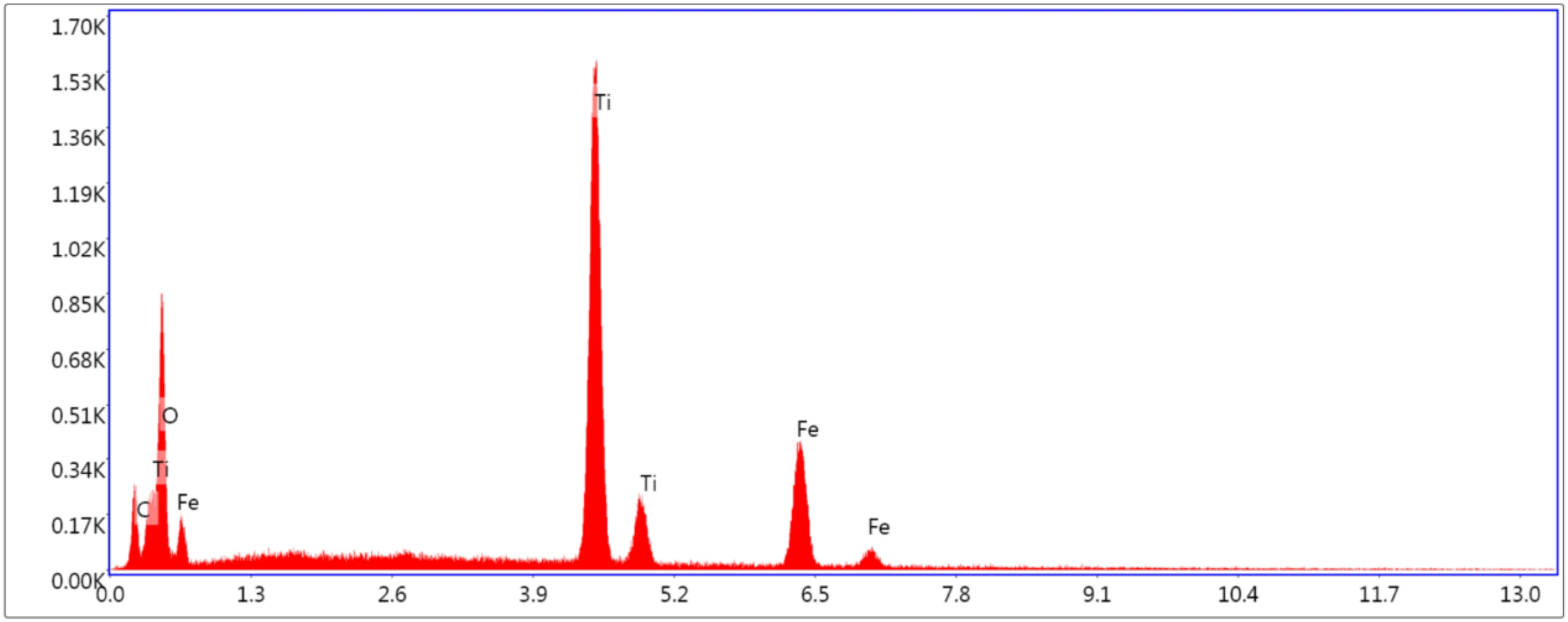

Lsec: 30.0 50 Cnts 1.735 keV Det: Octane Elite 25

MThin Smart Quant Results (Theoretical)

Element	Weight %	Atomic %	Net Int.	Net Error%	KABFactor
C K	2.62	8.92	96.11	3.45	0.53
O K	6.40	16.35	285.00	1.64	0.44
TiK	66.57	56.84	1297.49	0.85	1
FeK	24.42	17.89	366.81	2.08	1.3

19. Monzonite

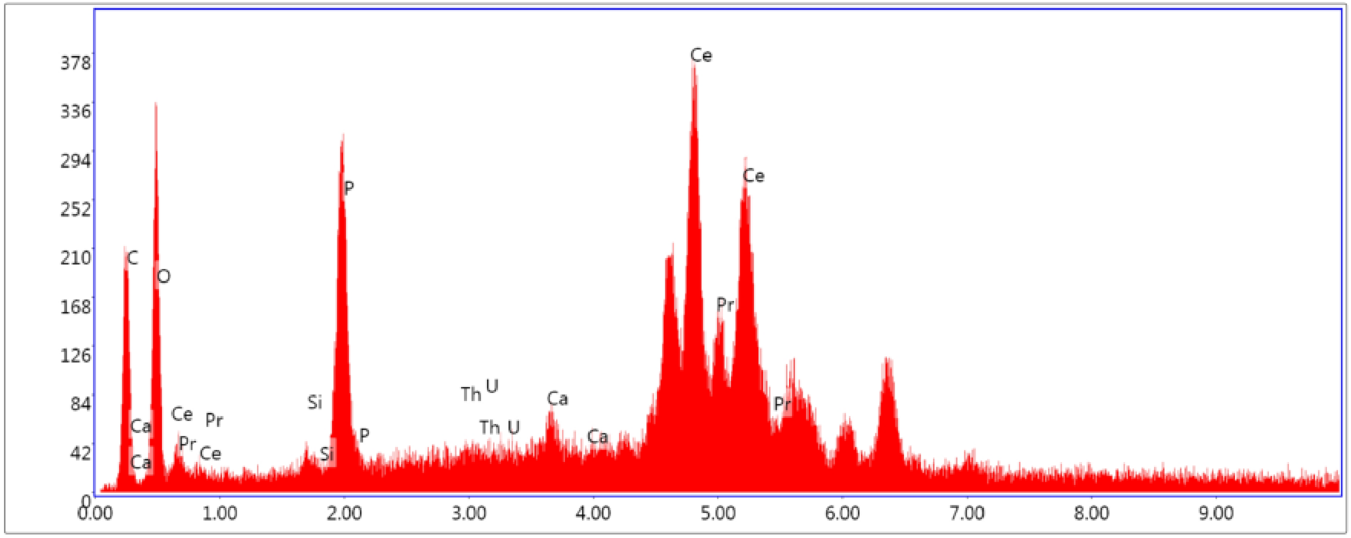

Lsec: 20.0 2 Cnts 0.150 keV Det: Apollo X-SDD

eZAF Smart Quant Results

Element	Weight %	Atomic %	Net Int.	Error %	Kratio	Z	A	F
C K	21.41	50.49	137.08	10.29	0.0854	1.2610	0.3164	1.0000
O K	17.49	30.97	208.42	10.93	0.0471	1.2139	0.2218	1.0000
SiK	0.37	0.37	14.50	41.63	0.0016	1.1182	0.3802	1.0051
P K	7.53	6.88	309.28	8.89	0.0399	1.0760	0.4886	1.0076
ThM	0.60	0.07	12.15	58.44	0.0049	0.7056	1.1294	1.0201
U M	0.40	0.05	8.62	40.10	0.0033	0.7027	1.1539	1.0238
CaK	1.25	0.88	58.72	15.69	0.0118	1.0667	0.8481	1.0461
CeL	37.04	7.49	545.63	4.02	0.3090	0.7785	1.0700	1.0014
PrL	13.91	2.80	196.97	8.42	0.1161	0.7848	1.0639	0.9999

20. Rutile

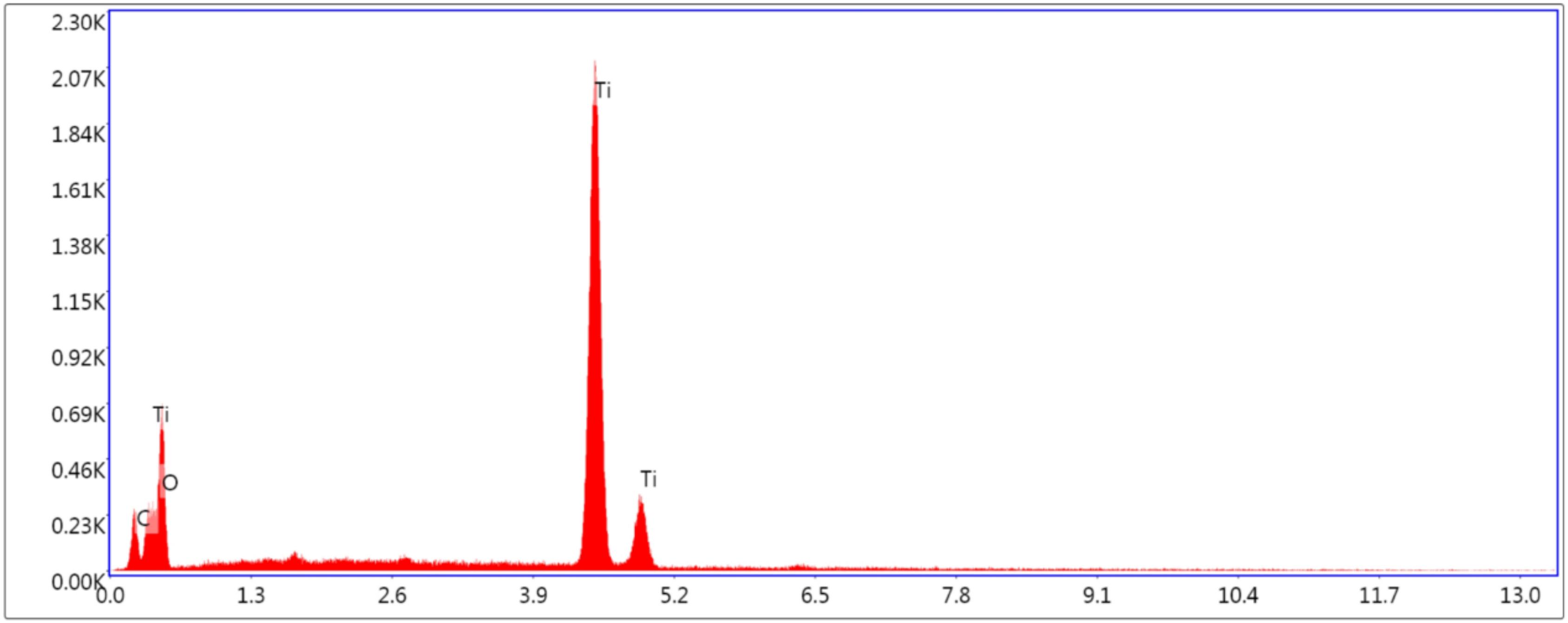

Lsec: 30.0 76 Cnts 1.735 keV Det: Octane Elite 25

MThin Smart Quant Results (Theoretical)

Element	Weight %	Atomic %	Net Int.	Net Error%	KABFactor
C K	2.96	10.00	102.18	3.12	0.53
O K	4.65	11.79	194.89	1.99	0.44
TiK	92.39	78.21	1692.83	0.69	1

21. Titanite

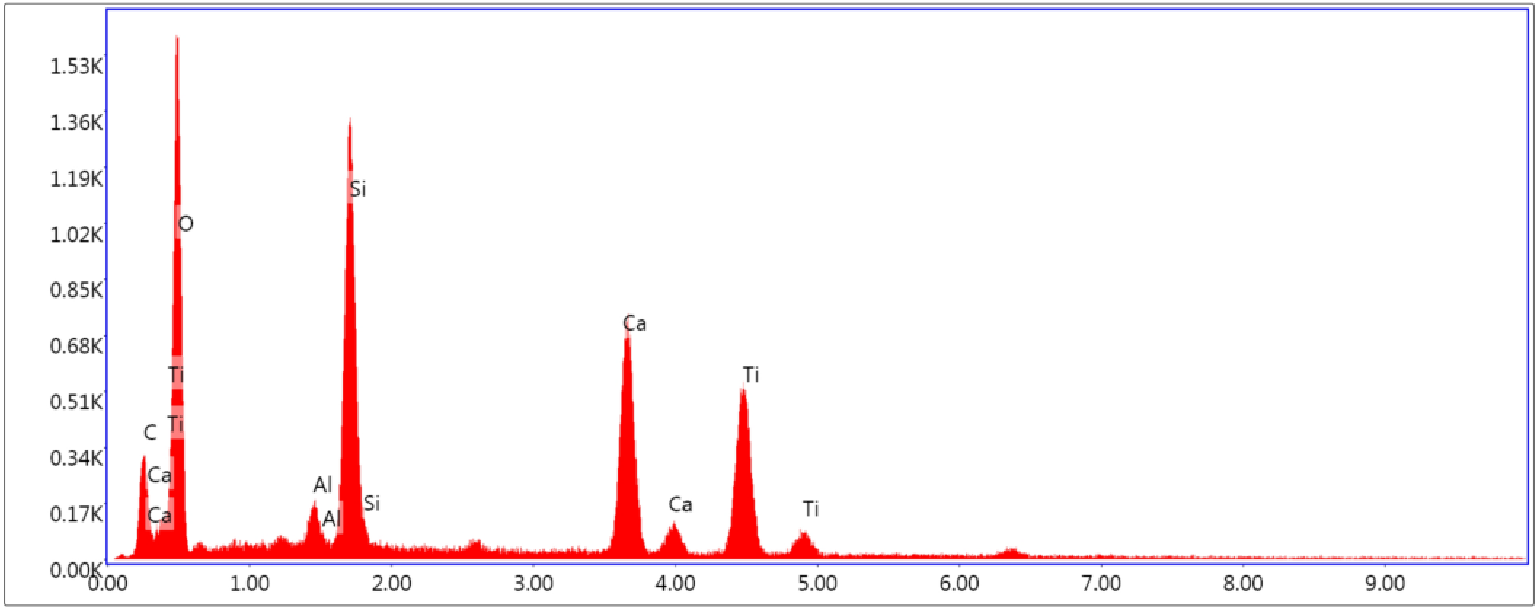

Lsec: 20.0 7 Cnts 0.150 keV Det: Apollo X-SDD

eZAF Smart Quant Results

Element	Weight %	Atomic %	Net Int.	Error %	Kratio	Z	A	F
C K	19.85	28.62	233.30	9.68	0.0618	1.0707	0.2908	1.0000
O K	54.52	59.04	974.07	10.29	0.0935	1.0251	0.1673	1.0000
AlK	1.02	0.66	115.68	10.94	0.0053	0.9125	0.5597	1.0048
SiK	8.64	5.33	1213.74	5.20	0.0561	0.9326	0.6928	1.0045
CaK	8.12	3.51	856.66	2.81	0.0732	0.8805	0.9946	1.0293
TiK	7.85	2.84	670.59	3.13	0.0626	0.7981	0.9821	1.0170

22. Tourmaline

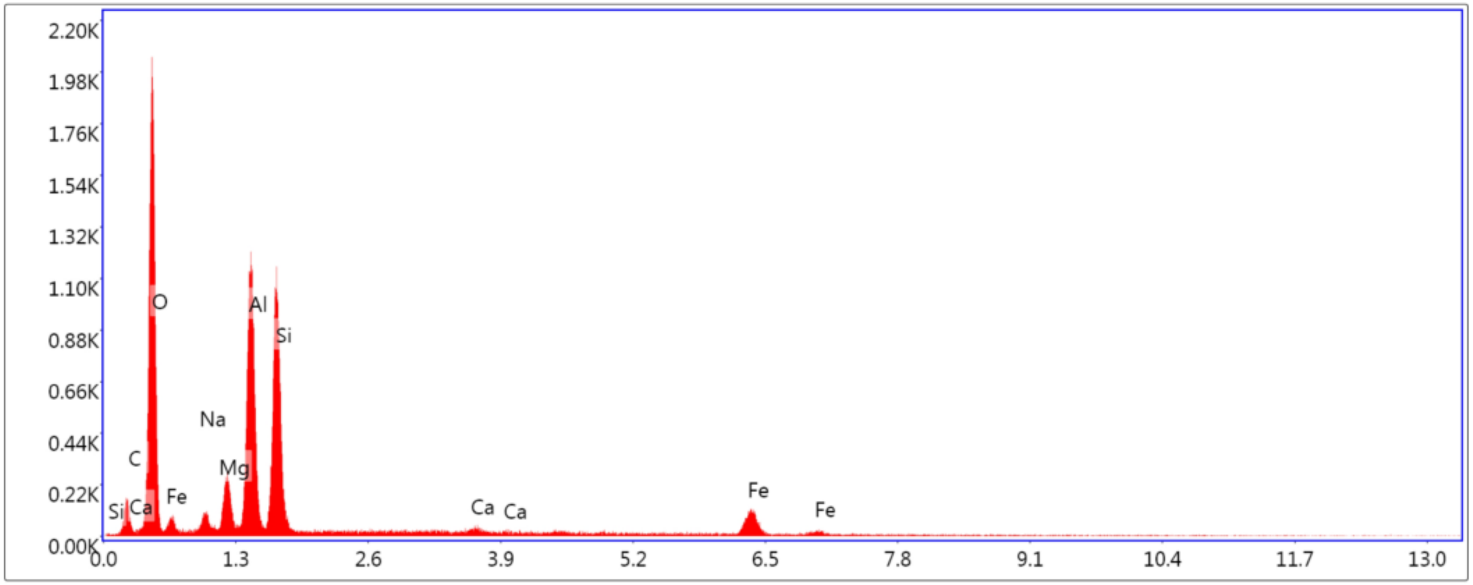

Lsec: 30.0 920 Cnts 1.735 keV Det: Octane Elite 25

MThin Smart Quant Results (Theoretical)

Element	Weight %	Atomic %	Net Int.	Net Error%	KABFactor
C K	2.16	4.10	52.21	5.52	1.02
O K	30.94	44.09	907.21	0.89	0.84
NaK	1.43	1.42	39.54	9.46	0.89
MgK	5.26	4.93	137.83	2.97	0.94
AlK	23.66	19.99	679.49	1.09	0.85
SiK	25.73	20.89	631.79	1.29	1
CaK	0.91	0.52	15.06	30.03	1.48
FeK	9.91	4.05	97.97	5.84	2.48

23. Zircon

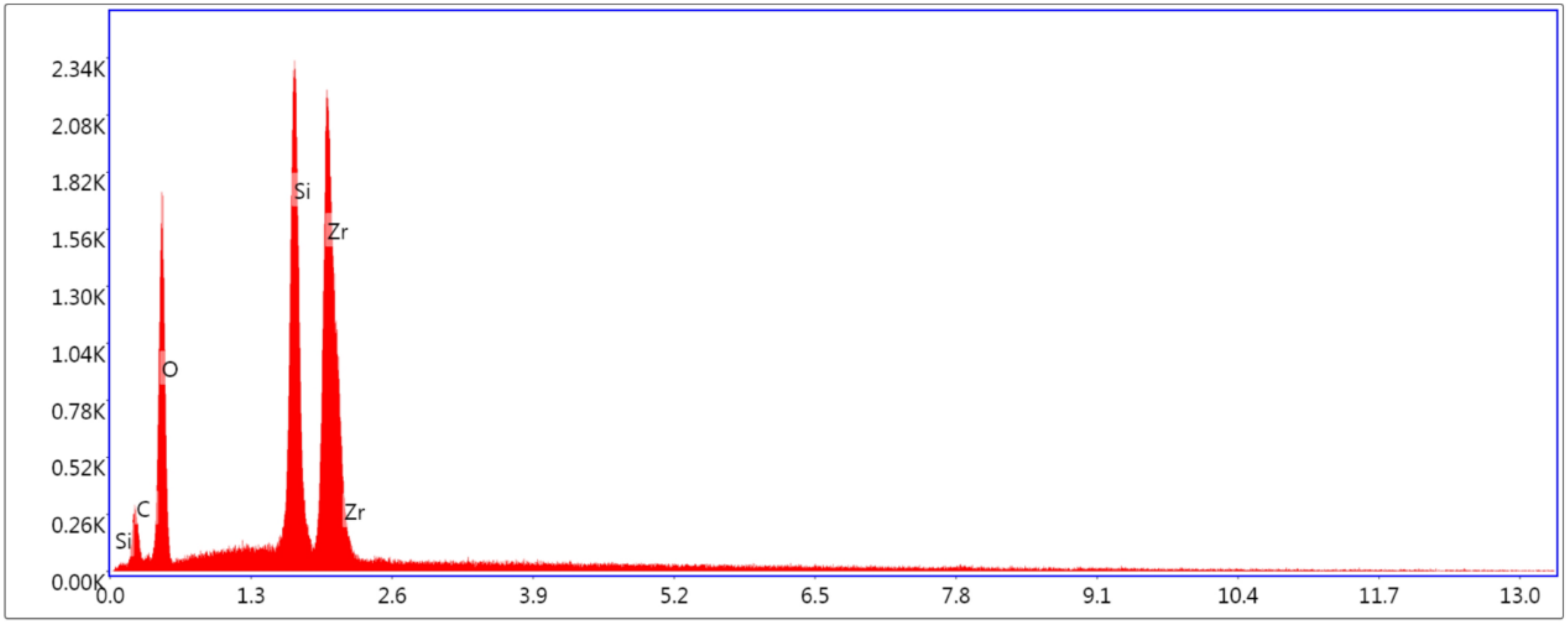

Lsec: 30.0 18 Cnts 5.780 keV Det: Octane Elite 25

MThin Smart Quant Results (Theoretical)

Element	Weight %	Atomic %	Net Int.	Net Error%	KABFactor
C K	1.84	5.93	94.27	4.72	1.02
O K	12.72	30.73	790.63	0.94	0.84
SiK	28.49	39.21	1482.83	0.80	1
ZrL	56.95	24.13	1497.79	1.00	1.98

Appendix B: BSE images for some samples

Sample CR-27 REFERNCE

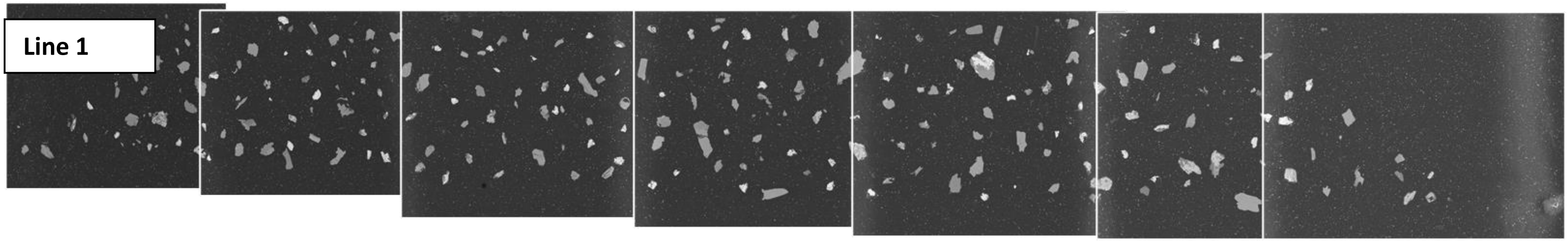

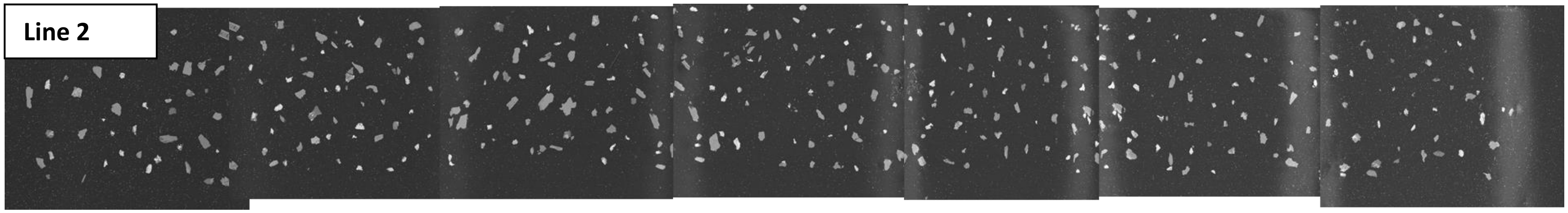

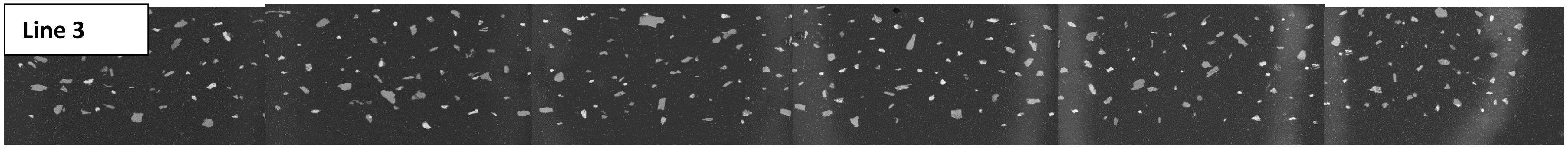

1000 um

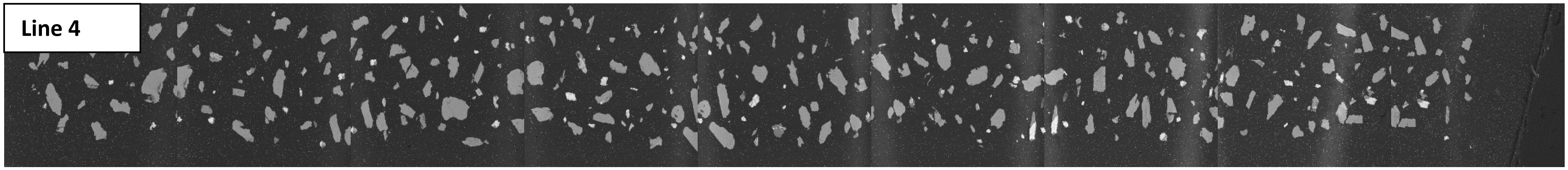
Line 4

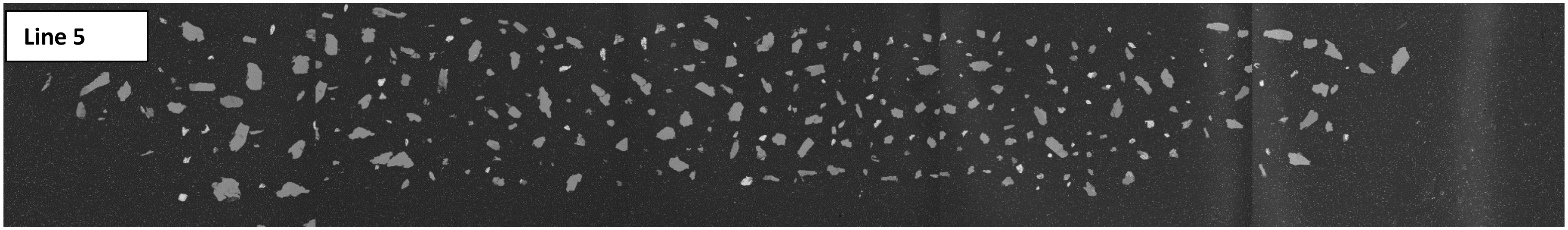
Line 5

1000 um

Sample CR-27-Un-sieved-Frantz separated

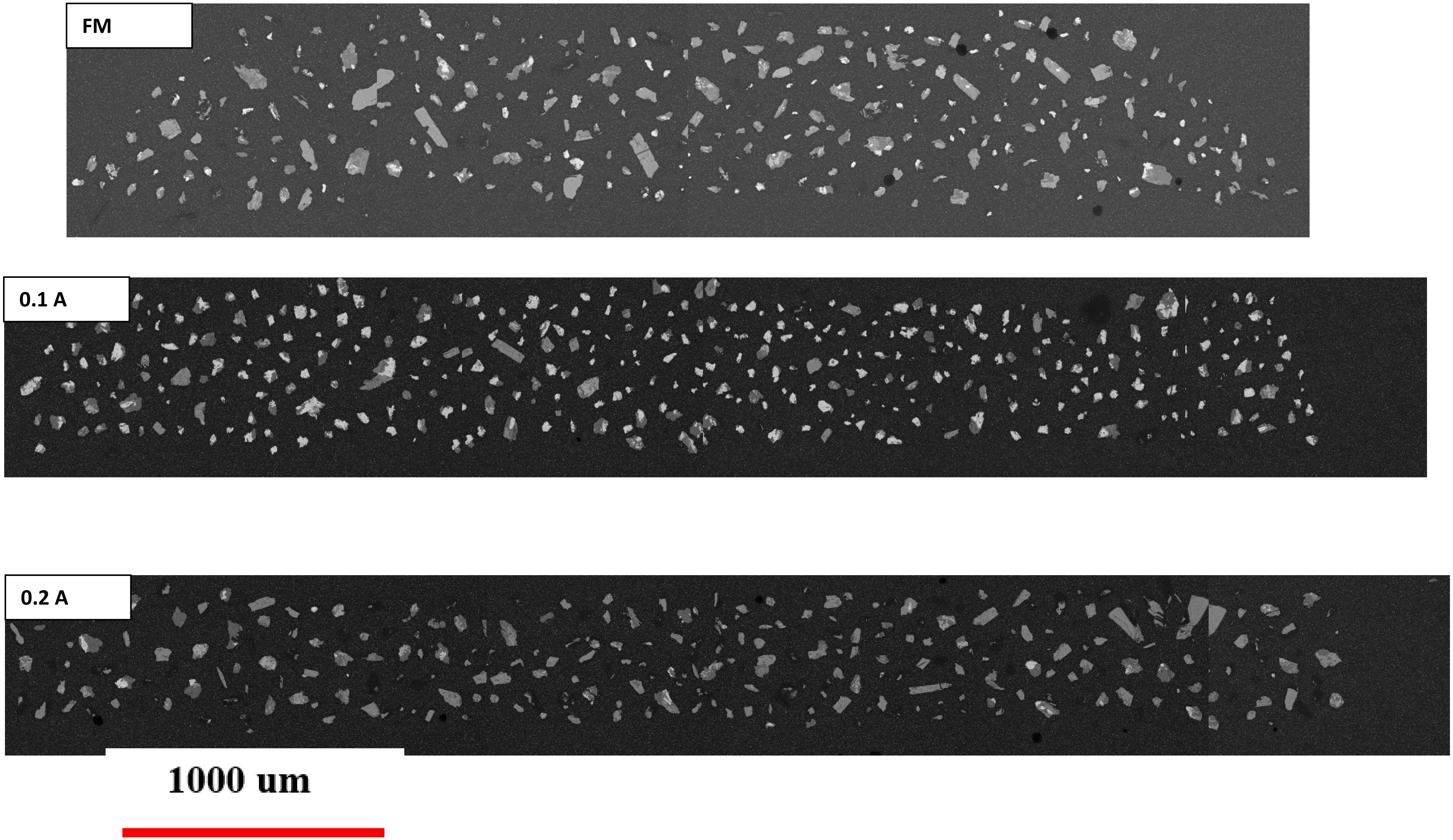

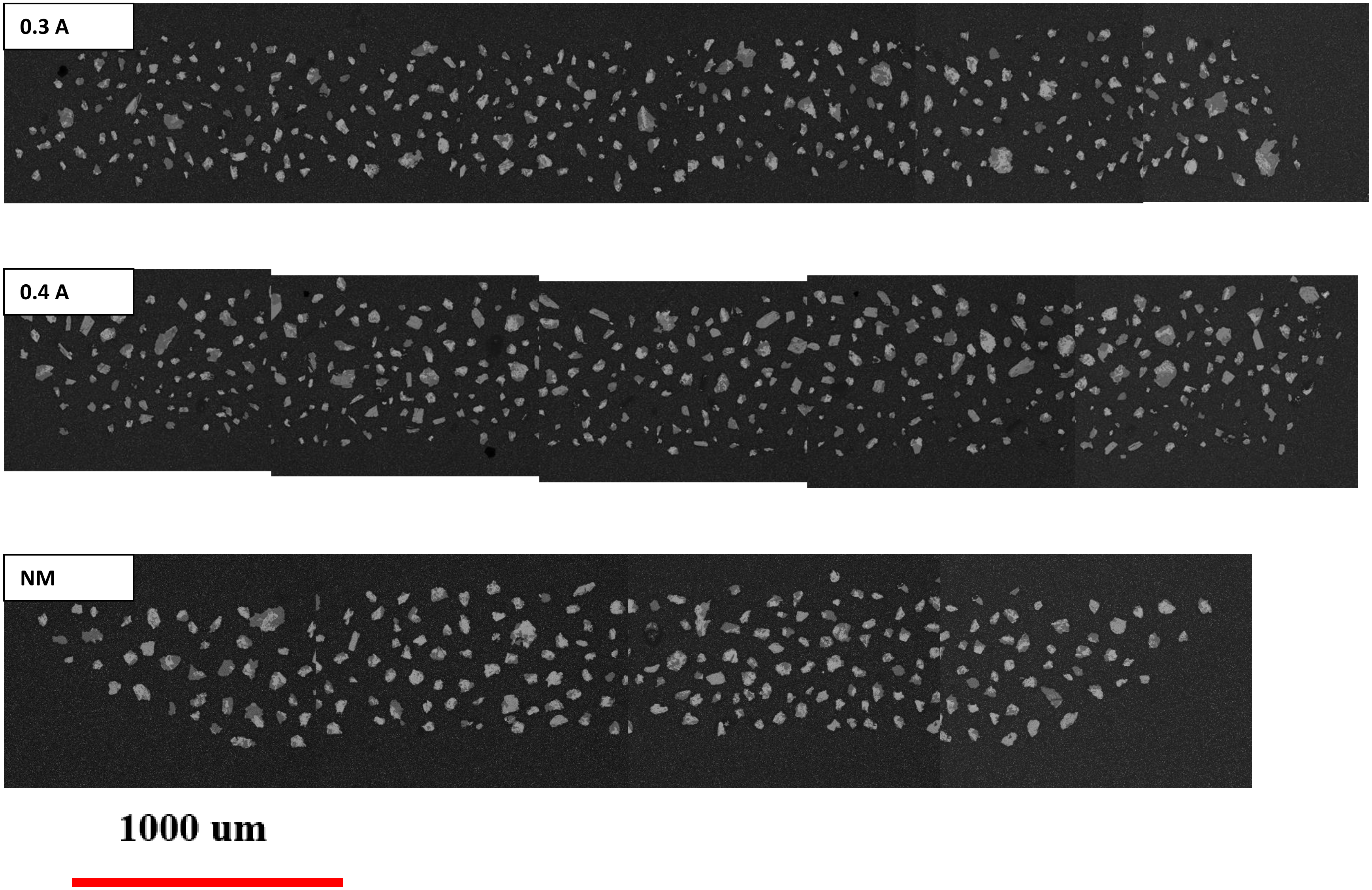
0.3 A
0.4 A
NM
1000 um

Sample CR-27-< 250 um - Frantz separated

FM

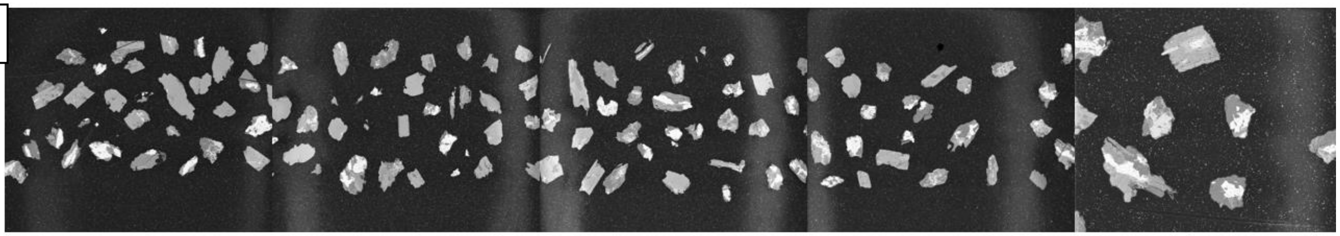

0.1 A

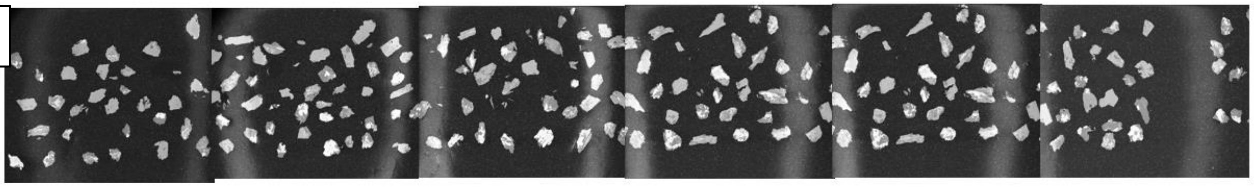

0.2 A

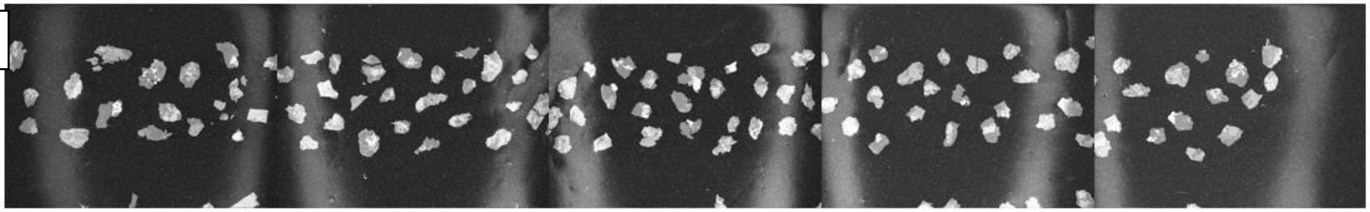

0.3 A

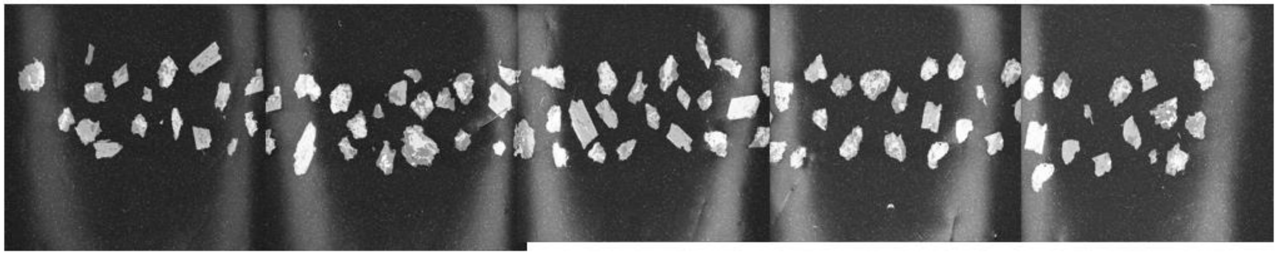

1000 um

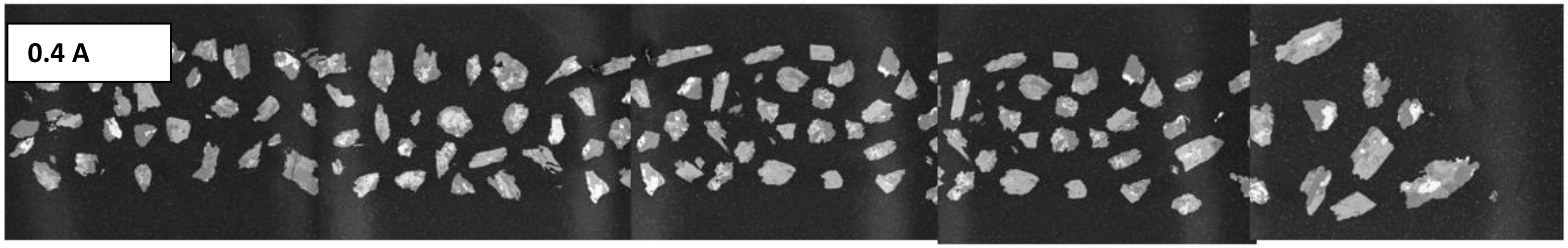

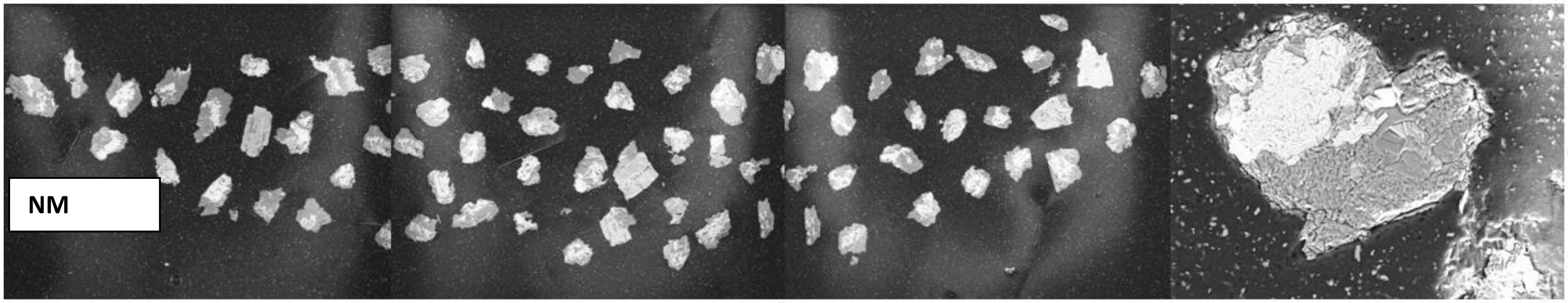

1000 um

Sample CR-27-< 150 um - Frantz separated

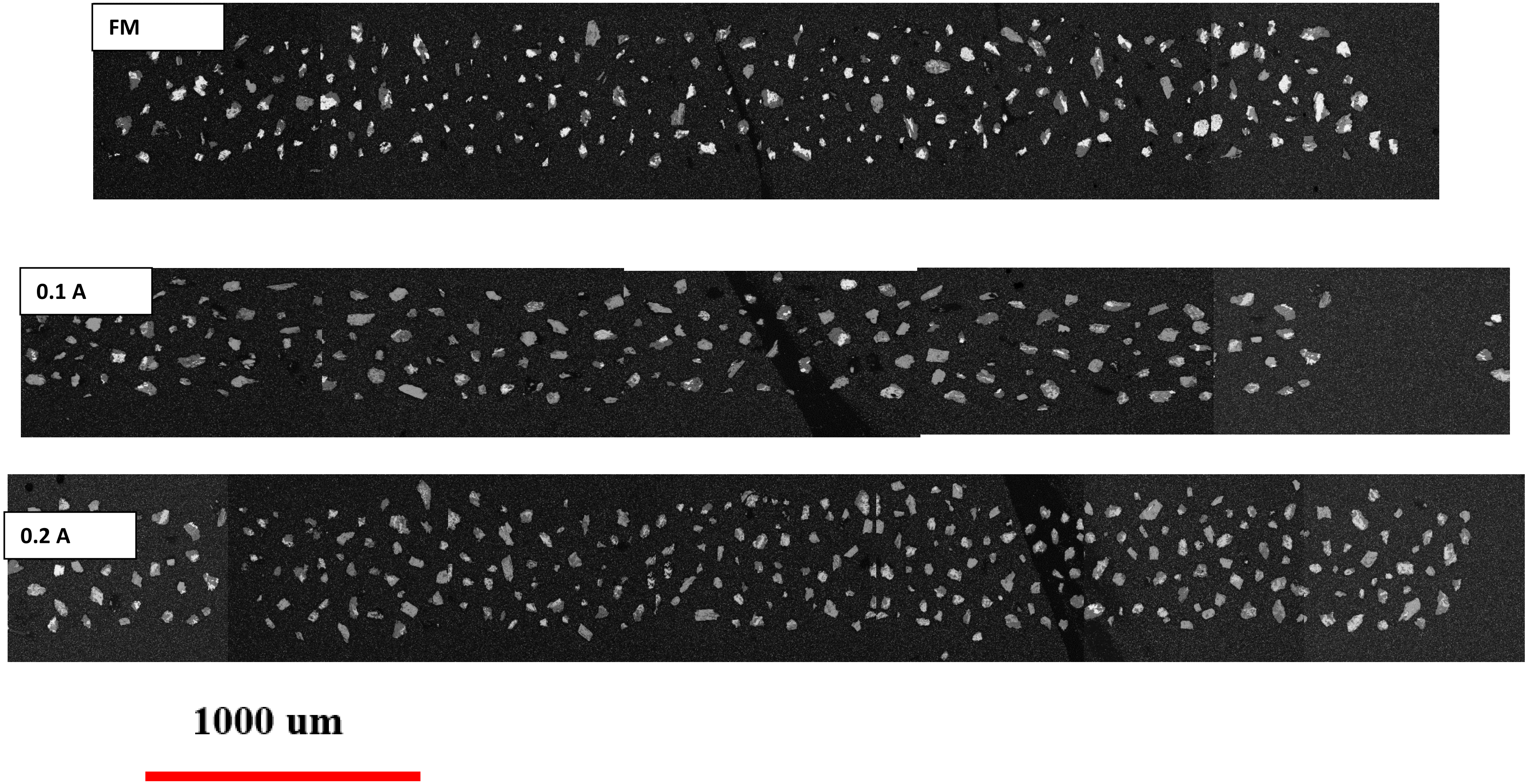

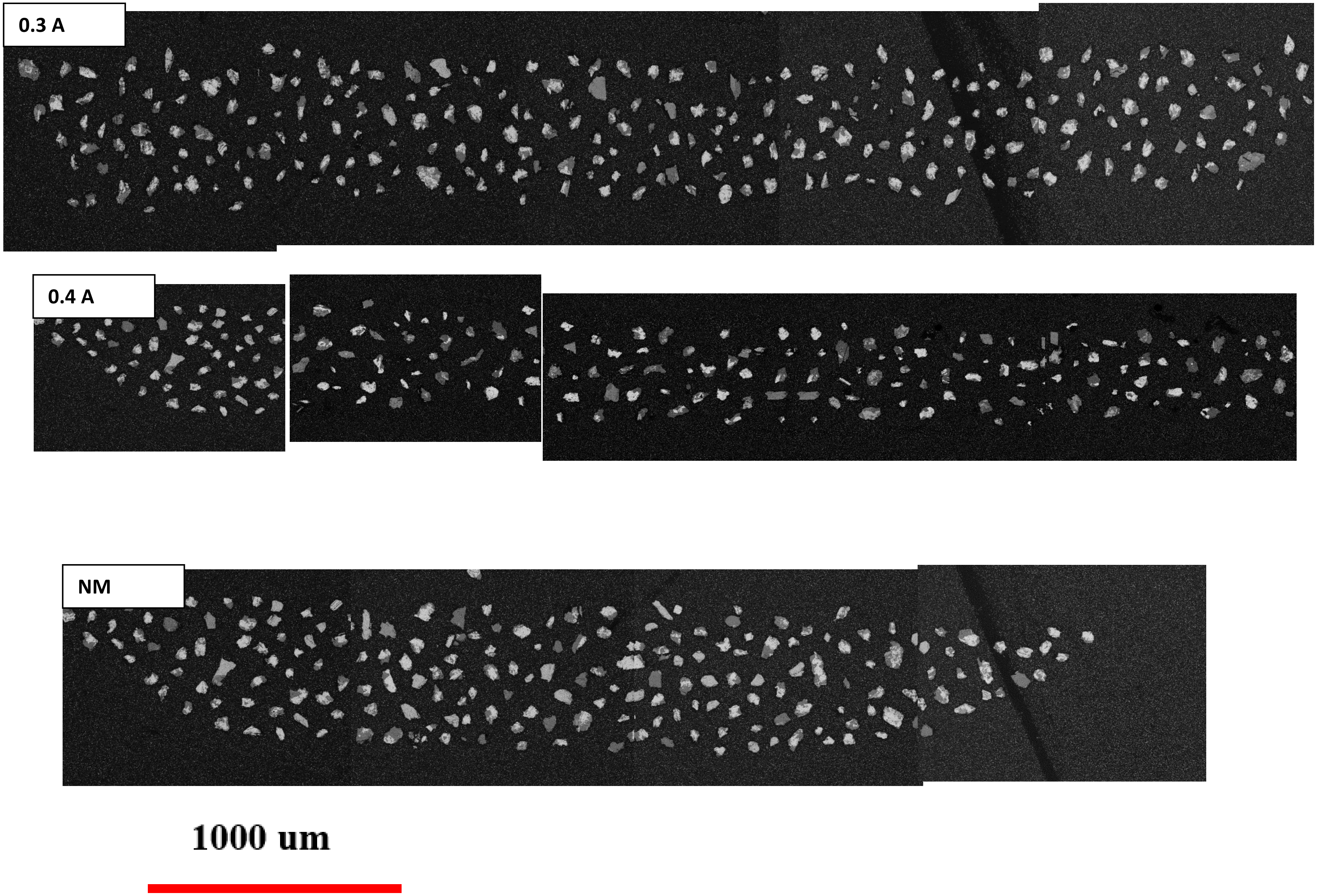
0.3 A
0.4 A
NM
1000 um

Sample CR-18 REFERNCE

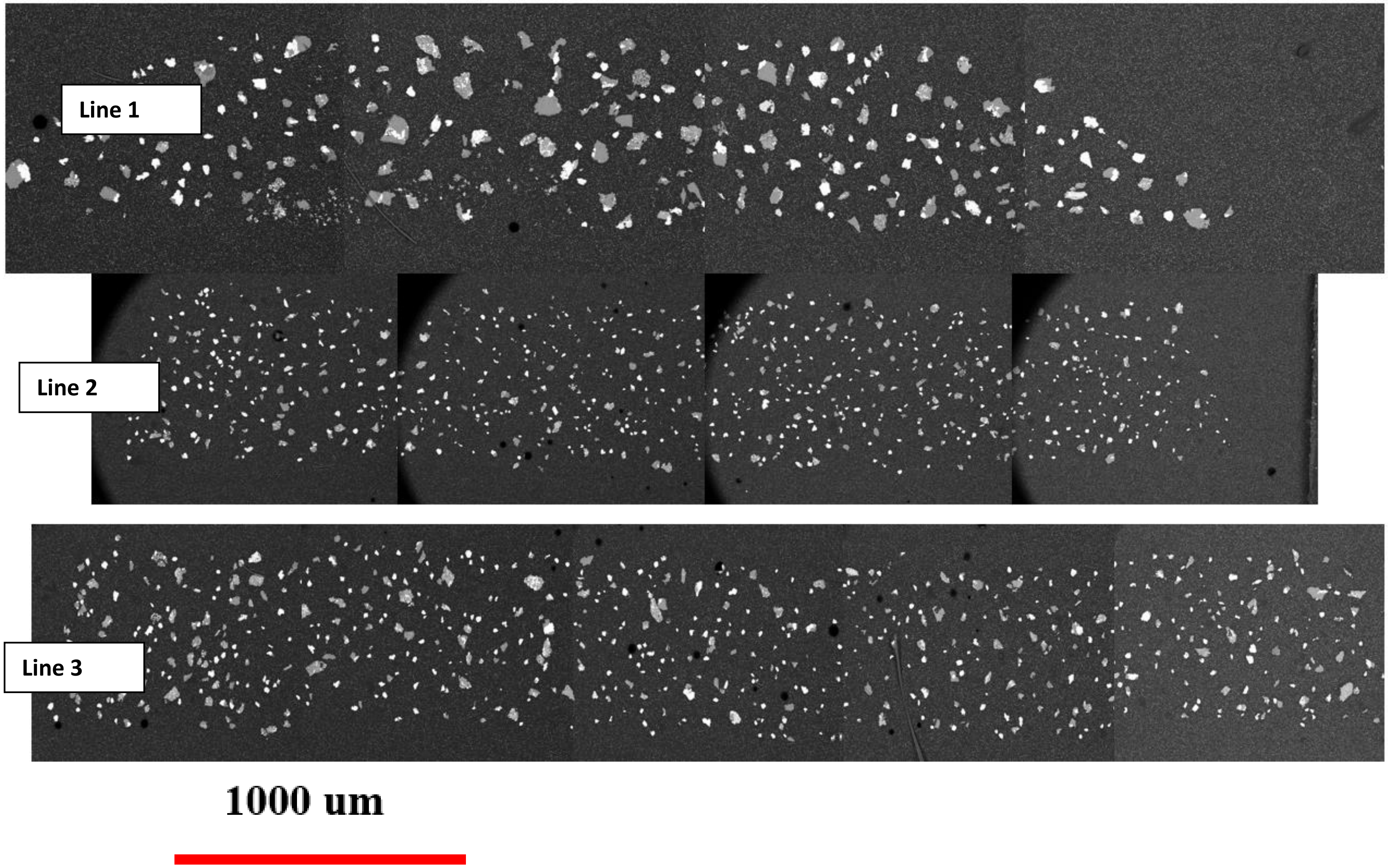

Line 4

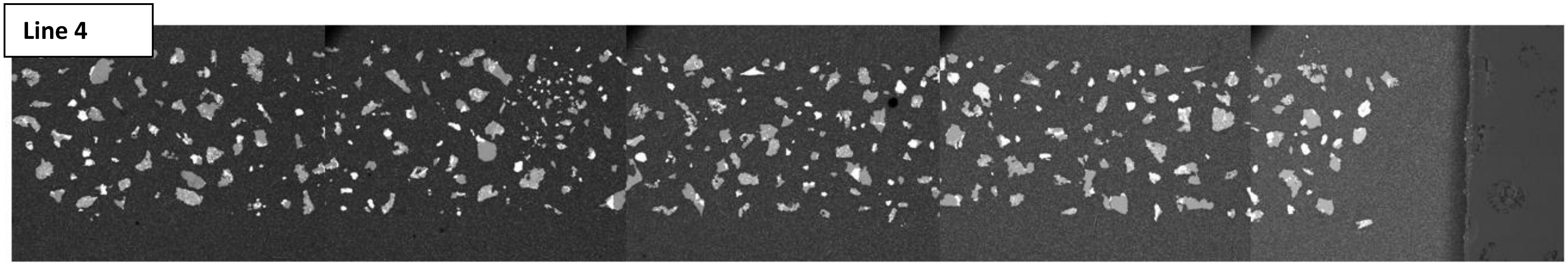

Line 5

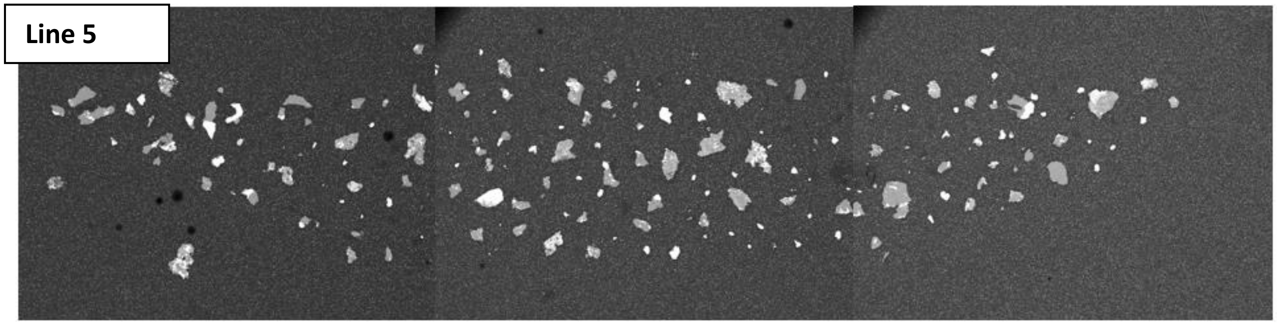

1000 um

Sample CR-03 REFERNCE

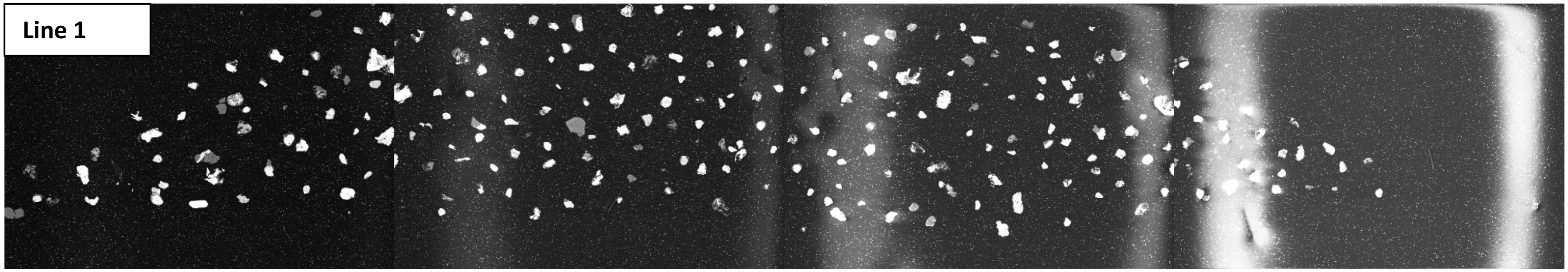
Line 1

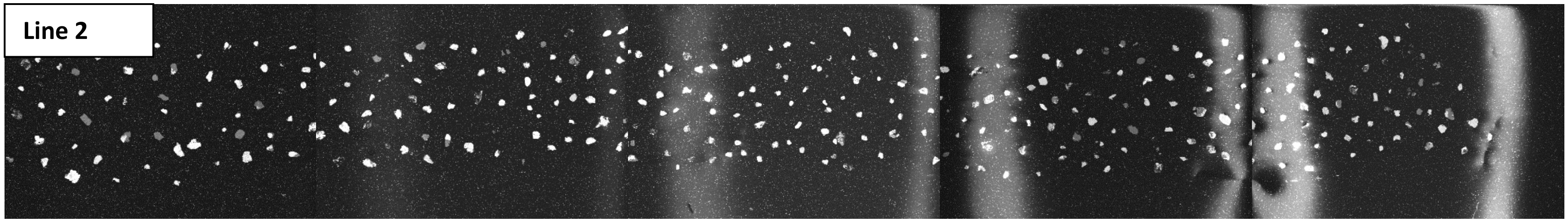
Line 2

1000 um

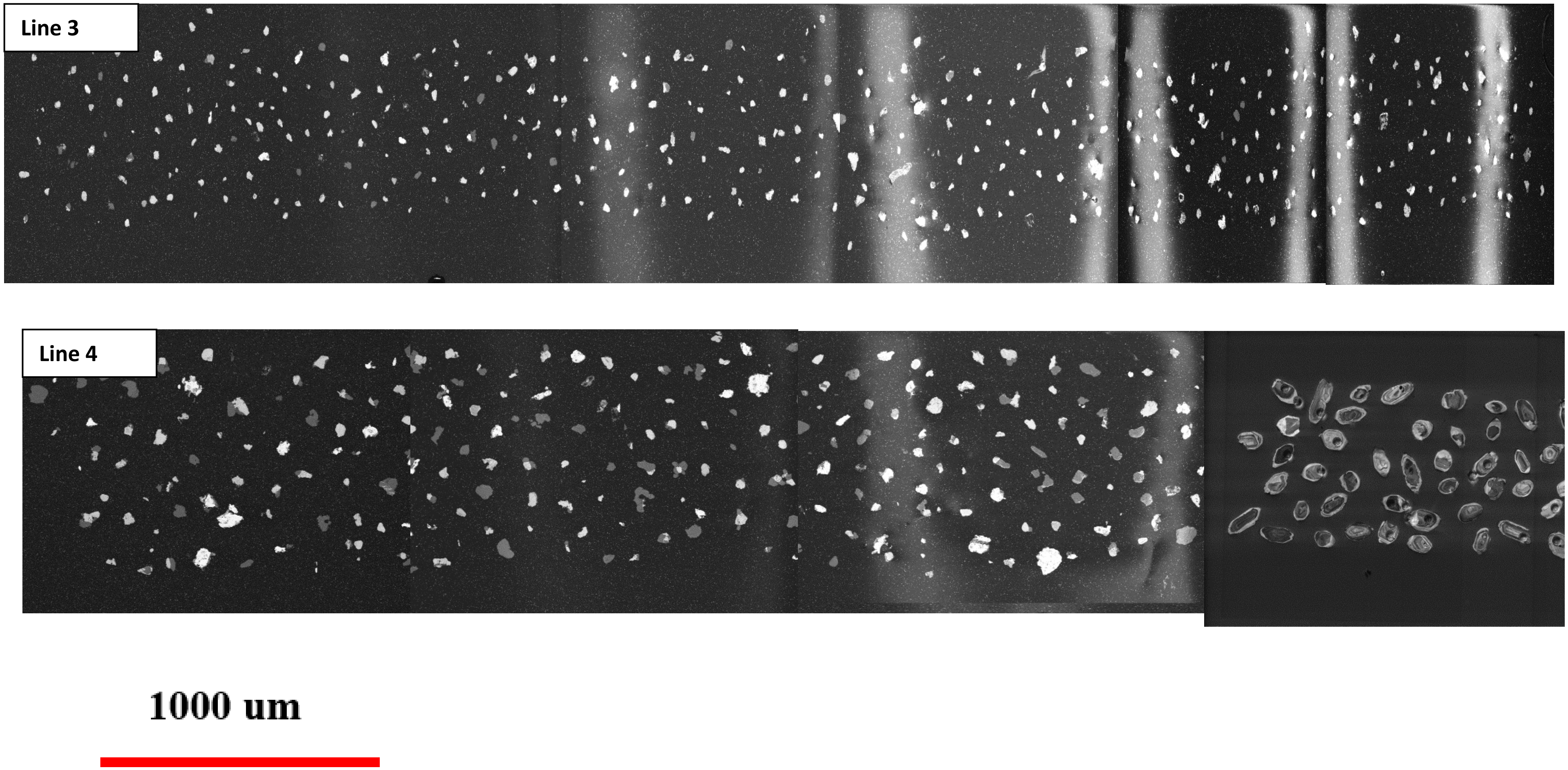
Line 3
Line 4
1000 um

Appendix C: Tables for heavy minerals identified using SEM

FE-SEM-EDS results for heavy minerals present in rock samples for un-sieved grain size fraction. Table include % of each heavy mineral in rock sample from total % heavy mineral composition. Light minerals are not included.

Un-sieved (Frantz separated)

M				**FM**			**0.1 A**			**0.2 A**			**0.3 A**			**0.4 A**			**NM**	
#	**Color code**	**Mineral**	**CR-27**	**CR-18**	**CR-03**	**CR-27**	**CR-18**	**CR-03**	**CR-27**	**CR-18**	**CR-03**	**CR-27**	**CR-18**	**CR-03**	**CR-27**	**CR-18**	**CR-03**	**CR-27**	**CR-18**	**CR-03**
1	🟫	Almandine			1.96			2.04		22.22						2.43				
2	🟩	Apatite-F	2.85				2.43					4.25	54.54		9.75	48.78		31.70	30.95	
3	🟪	Barite														7.31			26.19	
4	🟨	Goethite		4.87	5.88		7.31	2.04		22.22	1.78		9.09							
5	🟥	Hematite	25.71	60.97	31.337	7.22	78.04	55.10	4.76	44.44	19.64			8.19		2.43	2.5			
6	🟦	Hematite-Tin	48.57	31.70	39.21	68.67	9.75	24.48	38.09		33.92		9.09	11.47			2.5			
7	🟩	Ilmenite	5.71	2.43	9.80	12.04	2.43	6.12	9.52		8.92	4.25			2.43					
8	⬛	Monzonite											9.09			7.31				
9	🟥	Rutile	17.14		5.88	12.04		2.04	47.61	11.11	5.35	91.48	18.18	4.91	87.80	19.51	10.00	68.29	19.04	30.00
10	🟪	Titanite														2.43			16.66	
11	🟦	Tourmaline			1.96			2.04			21.42			60.65			62.50			
12	🟪	Zircon			3.92			6.12			8.92			14.75		9.75	22.50		7.14	70.00
Total:																				
Amount of lithoclasts:			~24.25	~1.71	~10.69	~24.25	~1.71	~10.69	~24.25	~1.71	~10.69	~24.25	~1.71	~10.69	~24.25	~1.71	~10.69	~24.25	~1.71	~10.69

FE-SEM-EDS results for heavy minerals present in rock samples for grain size fraction <250 µm . Table include % of each heavy mineral in rock sample from total % heavy mineral composition. Light minerals are not included.

Grain size < 250 µm

M			FM			0.1 A			0.2 A			0.3 A			0.4 A			NM		
#	**Color code**	**Mineral**	**CR-27**	**CR-18**	**CR-03**	**CR-27**	**CR-18**	**CR-03**	**CR-27**	**CR-18**	**CR-03**	**CR-27**	**CR-18**	**CR-03**	**CR-27**	**CR-18**	**CR-03**	**CR-27**	**CR-18**	**CR-03**
1	🟫	Almandine								8.33			6.66							
2	🟩	Apatite-F					2.04	4.16		12.5	3.22		6.66			18.75			10.52	
3	🟪	Barite																	15.75	
4	🟨	Goethite						4.16		4.16			6.66							
5	🟥	Hematite	20.00	73.17	33.33		69.38	29.16		45.83	35.48		60.00	11.76		62.5	23.52		10.52	37.50
6	🟦	Hematite-Tin	30.00	21.95	4.76	37.5	14.28		45.00	8.33		32.14	6.66	47.05	7.14		41.17			12.50
7	🟩	Ilmenite	20.00	2.43	4.76	18.75	6.12	25.00	20.00	16.66			6.66		3.57	6.25				
8	⬛	Monzonite			4.76			25.00			19.35			17.64			29.41			37.50
9	🟥	Rutile	30.00	2.43	33.33	37.50	6.12	16.66	35.00		9.67	67.85	6.66	17.64	89.28	6.25		24.00	36.84	12.50
10	🟪	Titanite					2.04	4.16		4.16						6.25			5.26	
11	🟦	Tourmaline			23.80			16.66			32.25			5.88			5.88		21.05	
12	🟪	Zircon				6.25														
Total:			100.00	100.00	100.00	100.00	100.00	100S. 00	100.00	100.00	100.00	100.00	100.00	100.00	100.00	100.00	100.00	100.00	100.00	100.0
Amount of lithoclasts:			~51.92	~15.15	~43.84	~51.92	~15.15	~43.84	~51.92	~15.15	~43.84	~51.92	~15.15	~43.84	~51.92	~15.15	~43.84	~51.92	~15.15	~43.84

F FE-SEM-EDS results for heavy minerals present in rock samples for grain size fraction <150 µm . Table include % of each heavy mineral in rock sample from total % heavy mineral composition. Light minerals are not included

Grain size < 150 µm

			FM			0.1 A			0.2 A			0.3 A			0.4 A			NM		
#	Color code	Mineral	CR-27	CR-18	CR-03	CR-27	CR-18	CR-03	CR-27	CR-18	CR-03	CR-27	CR-18	CR-03	CR-27	CR-18	CR-03	CR-27	CR-18	CR-03
1	🟥	Almandine			8.33		2.94			6.25	27.90		8.33	26.41						
2	🟩	Apatite-F	3.63			3.92	2.94			6.25			25.00		18.18	48.27		35.00		
3	🟪	Barite																	4.54	
4	🟨	Goethite			41.66			2.56		12.50										
5	🟥	Hematite	3.63	72.09	36.11	1.96	85.29	25.64		56.25	30.23		41.66	4.71		6.89				
6	🟦	Hematite-Tin	40.00	25.58	11.11	70.58	5.88	33.33	8.33		11.62		8.33	0.94			1.69			
7	🟩	Ilmenite	21.81		2.77	13.72	2.94	33.33	25.00		18.60	4.16		2.83	2.27	3.44				
8	⬛	Monzonite																		
9	🟥	Rutile	30.90	2.32		9.80		2.56	66.66	12.50	6.97	95.83	16.66	3.77	79.54	24.13	20.33	65.00	68.18	40.74
10	🟪	Titanite								6.25						10.34			27.27	
11	🟦	Tourmaline												56.60			67.79			18.51
12	🟪	Zircon						2.56			4.65			4.71		6.89	10.16			40.74
Total:																				
Amount of lithoclasts:			~13.91	~11.43	~7.00	~13.91	~11.43	~7.00	~13.91	~11.43	~7.00	~13.91	~11.43	~7.00	~13.91	~11.43	~7.00	~13.91	~11.43	~7.00

Appendix D: Results from XRD analysis

1. **Sample CR-27 REFERNCE**

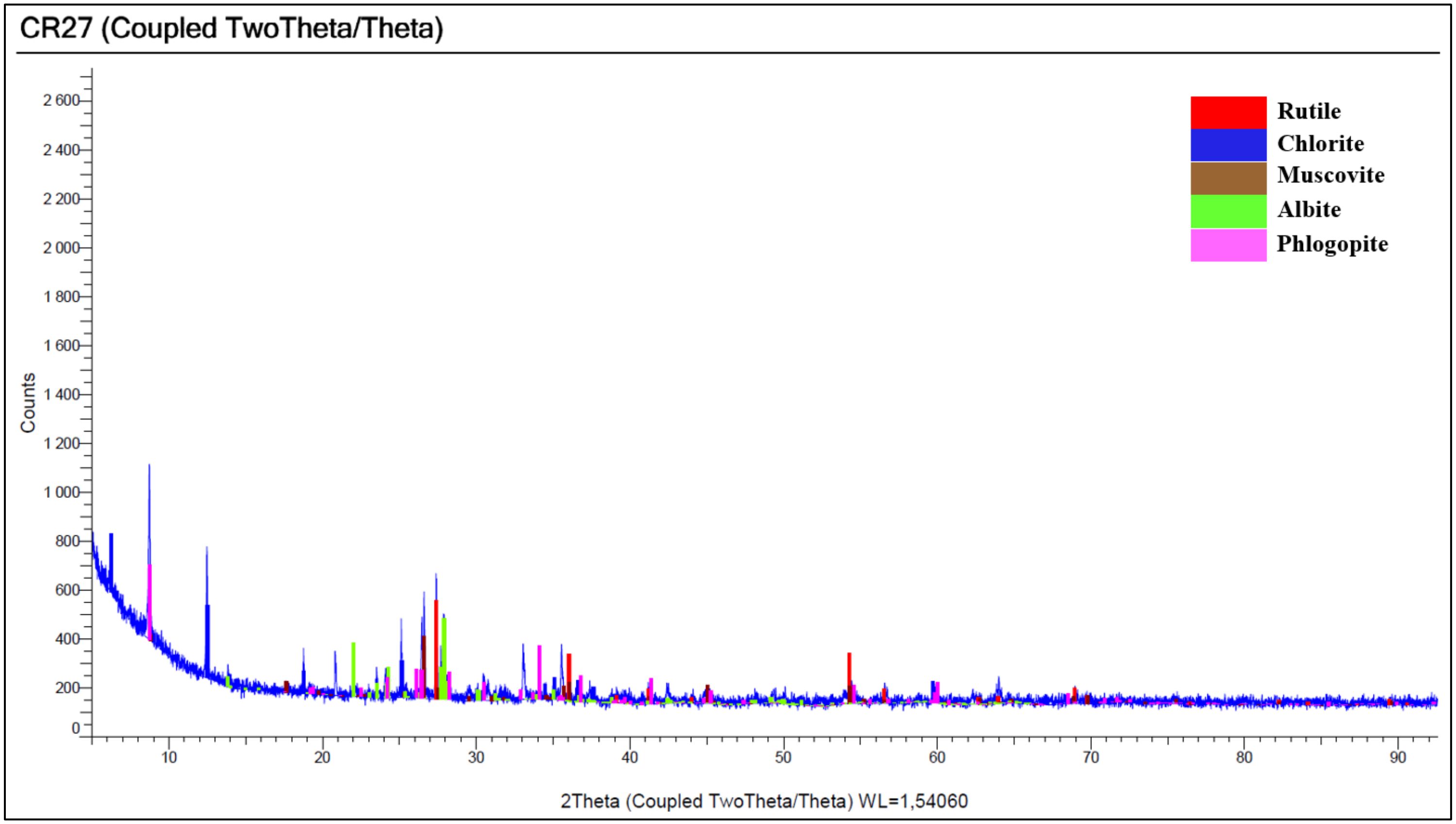

2. Sample CR-18 Reference

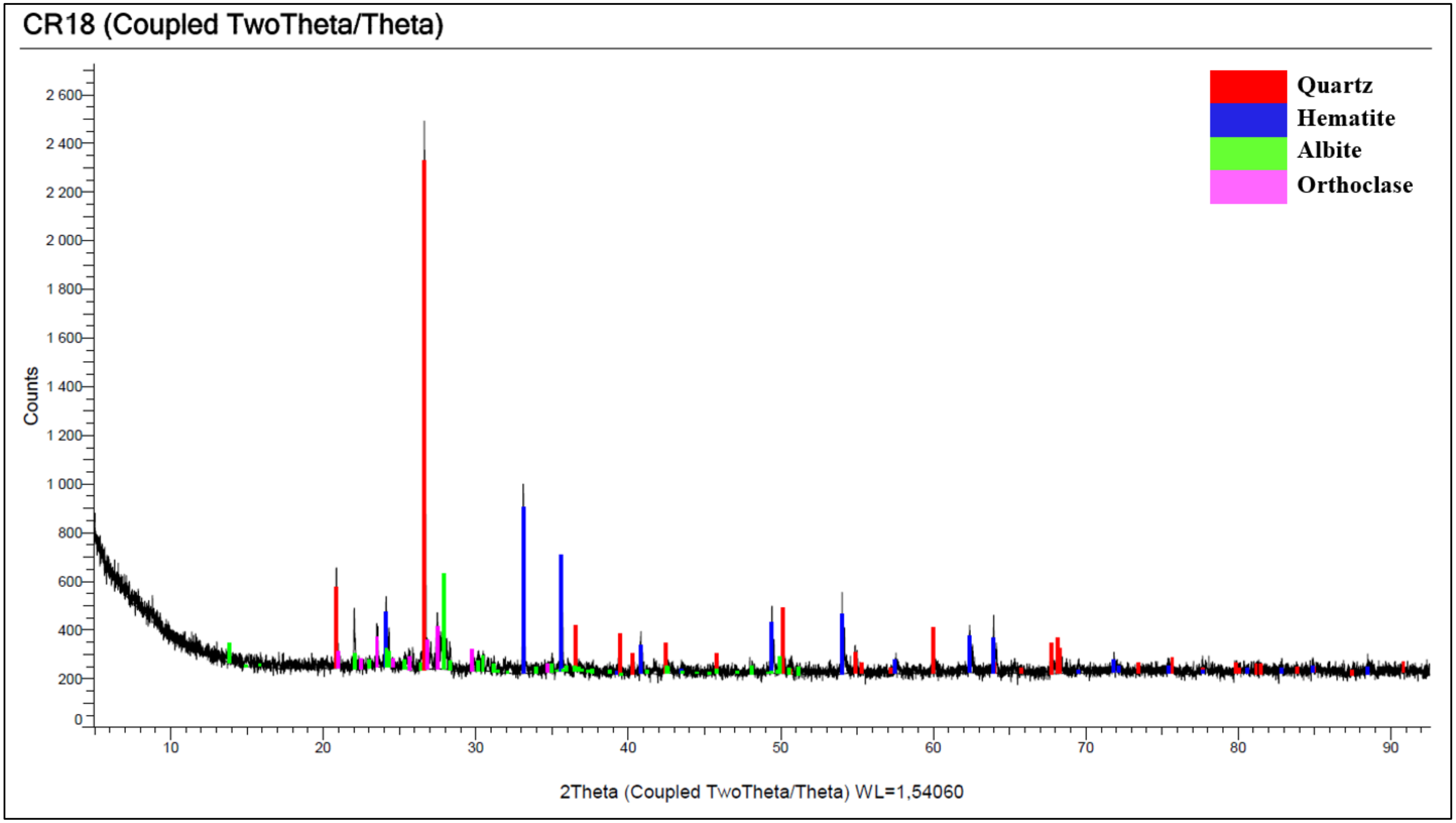
CR18 (Coupled TwoTheta/Theta)
Counts
2Theta (Coupled TwoTheta/Theta) WL=1,54060
Quartz
Hematite
Albite
Orthoclase